VYSOKÉ UČENÍ TECHNICKÉ V BRNĚ

BRNO UNIVERSITY OF TECHNOLOGY

FAKULTA STROJNÍHO INŽENÝRSTVÍ
ÚSTAV FYZIKÁLNÍHO INŽENÝRSTVÍ

FACULTY OF MECHANICAL ENGINEERING
INSTITUTE OF PHYSICAL ENGINEERING

APPLICATION OF SCANNING PROBE MICROSCOPY FOR THE STUDY OF ULTRATHIN FILMS AND NANOSTRUCTURES

APLIKACE RASTROVACÍ SONDOVÉ MIKROSKOPIE PRO VÝZKUM ULTRATENKÝCH VRSTEV A NANOSTRUKTUR

DIZERTAČNÍ PRÁCE
DOCTORAL THESIS

AUTOR PRÁCE   Ing. JAN NEUMAN
AUTHOR

VEDOUCÍ PRÁCE   prof. RNDr. TOMÁŠ ŠIKOLA, CSc.
SUPERVISOR

BRNO 2014

Abstrakt

Dizertační práce je obecně zaměřena na problematiku mikroskopie atomárních sil (AFM), a to jak vývoje částí těchto mikroskopů, tak i jejich obecnému využití v oblasti výzkumu povrchů, ultratenkých vrstev a nanostruktur. Na Ústavu fyzikálního inženýrství jsou vyvíjena zařízení umožňující aplikovat uvedenou mikroskopickou metodu. V těchto mikroskopech jsou využívány piezoelektrické motory pro zajištění pohybu vzorku a ladicích zrcátek v optickém detekčním systému. Práce se v části věnované vývoji AFM zabývá studiem parametrů řídicích pulzů za účelem optimalizace funkce těchto komponent. Měřením vlivu tvaru pulzů a opakovací frekvence byl jejich pohyb optimalizován z hlediska stability a rychlosti posuvu.

V části věnované výzkumu povrchů byly experimentálně zkoumány morfologické změny ultratenkých vrstev zlata na povrchu oxidu křemičitého za zvýšených teplot. Bylo zjištěno, že vhodná povrchová modifikace způsobuje vznik preferenčních trhlin ve vrstvě zlata. Řízeným rozdělením polykrystalické vrstvy na oddělené oblasti je možné významně ovlivnit proces tvorby ostrůvků zlata vznikajících při žíhání. S využitím metod elektronové litografie je možná příprava uspořádaných polí zlatých ostrůvků o velikostech 50 – 400 nm. Dále bylo ukázáno, že zvýšením teploty žíhání na 1000 °C dochází k postupnému zanořování ostrůvků zlata do povrchu. Tento jev je pravděpodobně způsoben přesunem oxidu křemičitého z oblasti pod zlatým ostrůvkem do těsného okolí vzniklého kráteru, kde tvoří tzv. límec. V těchto studiích vedle metody AFM byla s výhodou používána rovněž elektronová mikroskopie (SEM).

Abstract

The doctoral thesis is focused on the study of ultrathin layers and the utilization of atomic force microscopy (AFM) for their characterization. Morphological changes of ultrathin layer of gold on silica substrates at elevated temperatures were experimentally investigated. It was found that surface modification influences the formation of the voids in the gold layer. By the controlled dewetting of gold layer is possible to influence the formation of gold islands at elevated temperatures. Precise surface modification by electron beam lithography enabled preparation of ordered arrays of gold islands with the uniform size in range of 50 – 400 nm. It is also shown, that the increase of annealing temperature to 1000 °C induces embedding of the gold islands into the substrate. This phenomenon is probably caused by the silica transfer from the area bellow the islands to the rim. AFM methods are suitable for characterization of above mentioned nanostructures. The AFM working under the ultra-high vacuum conditions was developed at the Institute of Physical Engineering. Piezoelectric actuators are utilized for the sample approach and adjustment of the mirror used in optical detection system. The optimization was achieved by the systematic study of the driving pulse parameters. High stability and operating speed was achieved by the experimental measurements of the actuator response to the pulse shape and repetition frequency.

Klíčová slova

Mikroskopie atomárních sil, piezo-motory, tenké vrstvy, zlaté ostrůvky, nanostruktury

Keywords

Atomic force microscopy, piezo-actuators, thin films, gold islands, nanostructures

Prohlašuji, že jsem předloženou disertační práci vypracoval samostatně za odborného vedení prof. RNDr. Tomáše Šikoly, CSc., a RNDr. Antonína Fejfara, CSc. Dále prohlašuji, že veškeré podklady, ze kterých jsem čerpal, jsou uvedeny v seznamu použité literatury.

Ing. Jan Neuman

Obsah

Introduction

In the last decades atomic force microscopy (AFM) has become one of the basic techniques in nanotechnology. It enables surface analysis with a subnanometre resolution. Wide development of atomic force microscopy has been performed, driven by the research requirements focused on fabrication and characterization of the objects at nanoscale. Metallic nanostructures prepared on insulating substrates have been demonstrated to play an important role for instance in microelectronics, plasmonics (biosensing), semiconductor industry, magnetic memory media, and growth of nanowires. The fabrication of metallic nanostructures can be carried out by employing top-down or bottom-up approaches. Commonly used top-down methods, belonging to the group of lithographic techniques, cover photolithography, electron beam lithography, nanosphere lithography, colloidal lithography or surface milling by the focused ion beam. Bottom-up approaches utilize deposition procedures such chemical vapour deposition, molecular beam epitaxy or sol-gel synthesis. In the presented experimental work, the hybrid approaches have been utilized. Thermal evaporation is used for deposition of a gold thin layer on substrates patterned by electron beam lithography and the nanostructures have been fabricated by transformation of this layer at elevated temperatures into separated islands. Characterization of changes in surface morphology has been carried out by AFM accompanied by scanning electron microscopy (SEM).

The PhD thesis has been aimed at two main thematic areas. The first one has been devoted to the development of components of an ultra-high vacuum atomic force microscope, which mainly covers the optimization of piezo-actuator motions. The second one has been aimed at the study of morphological transformations of thin gold films during their annealing. Both development of the instrumentation and study of the surface transformation are based on the long-term research in the Institute of Physical Engineering (IPE) at the Brno University of Technology.

The theoretical description of the basic principles and commonly used measurement regimes are given in Part 1. An ultra-high vacuum AFM previously developed in IPE has undergone a software and electronics upgrade. The concept, design of mechanical and electronic parts of the developed AFM, is presented here as well. My personal contribution to AFM development issues can be mainly linked to the optimization of 3-axis rotary actuators used for laser beam alignment. The general procedure for characterization of properties and optimization of the piezoactuator motion is proposed in Part 2. Detailed analytical and numerical simulations are supported by experimental results and presented here.

Development of procedures for fabrication of nanostructures suitable for plasmonic applications is the main focus of this study in Parts 3 - 5. The work is aimed at the processes taking place at elevated temperatures where the morphological changes of thin films are observed. The brief description of the related processes is presented in Part 3. The main attention is paid to surface diffusion, solid-state dewetting and Ostwald ripening. The

experimental work reported in Part 4 deals with the fabrication of ordered arrays of gold islands formed on the pre-patterned silica substrates. The control of the dewetting process by proper surface modification is discussed and experimentally confirmed. The experimental work shows that the size and shape of islands, and regularity of their arrays are influenced by annealing temperature and surface modification. The last experimental study deals with the observed phenomena of embedding of gold islands into the silica substrate induced by annealing at high temperatures (1000 °C). Part 5 contains the characterization of embedded islands and formed craters. Unambiguous understanding of the embedding mechanism has not been previously reported and thus a detailed study of properties and dynamics of related phenomena is presented in this work. In this case an advanced data analysis of AFM and SEM images has been carried out to learn more details about the mechanism.

12

1. Scanning Probe Microscopy

Scanning probe microscopy belongs to the commonly used techniques in the field of surface science and nanotechnology. The first microscope of the SPM type (Scanning Probe Microscope) was STM (Scanning Tunneling Microscope) developed in 1981 by the group of Binnig and Rohrer in IBM laboratories [1, 2]. This work was awarded by the Nobel Prize in 1986. The SPM techniques utilize the interaction between the sample surface and the probe (sharp tip). Basic categorization can be done according to the type of tip-sample interaction as follows: AFM (Atomic Force Microscopy), STM (Scanning Tunneling Microscopy), MFM (Magnetic Force Microscopy), SNOM (Scanning Near-field Optical Microscopy), EFM (Electrostatic Force Microscopy) and others [3]. The interpretation of experimental results strongly depends on the applied techniques and generally are supported by ab-initio simulations, for example DFT (Density Function Theory) [4]. In the last three decades an extensive development of the SPM techniques has been achieved. The improvement of the measurements techniques, probes, design, electronics and software has been utilized based on the application requirement in the research or industry.

A wide range of SPM instruments operating at ambient conditions are currently available on the commercial market. The operation under ultra-high vacuum (UHV) conditions at low temperatures (LT, 20 K) requires an advanced technological approach and only a few producers such as Omicron, SPECS or RHK are able to deliver such systems. Due to a high cost of these systems, own SPM instrument was developed and continuously improved at IPE in the last decade. The design was optimized for experiments in a complex ultra-high vacuum apparatus [5]. The complex system enables to fabricate and characterize samples in situ (inside the UHV environment). Analysis of the samples directly after their preparation is favorable and prevents surface contamination and modification at ambient conditions. The developed UHV SPM system, being the part of the complex system, has been mainly designed for STM and AFM measurements.

1.1 Principles of Scanning Tunneling Microscopy

The first designed technique out of the SPM family was STM [2]. The principle of the method achieving the atomic resolution is based on the quantum effect of electron tunneling through the gap between the sharp tip and the sample under an applied voltage bias. The exponential dependence of the tunneling current I_t on the gap distance d determine the sensitivity of the methods for the topography imaging. The tip-sample distance d is typically in units of Å. The tunneling current can be expressed as $I_t = KU \exp(-kd)$, where U is the bias voltage and K, k are the constants. In Fig. 1.1 a basic experimental set up of STM is schematically shown. It is composed of a scanner, sharp tip and electronics. The imaging can be performed in two basic regimes, the constant height and the constant current. Using the constant current regime the distance between the tip and the sample is kept constant by the z approach of the scanner and corresponding feedback loop. The image is then represented by the voltage applied on the z piezoelement. The higher resolution can be achieved at the constant height regime when the z axis of the scanner is not moving and the

feedback is switched off. The image is then obtained from the value of the tunneling current during the scanning.
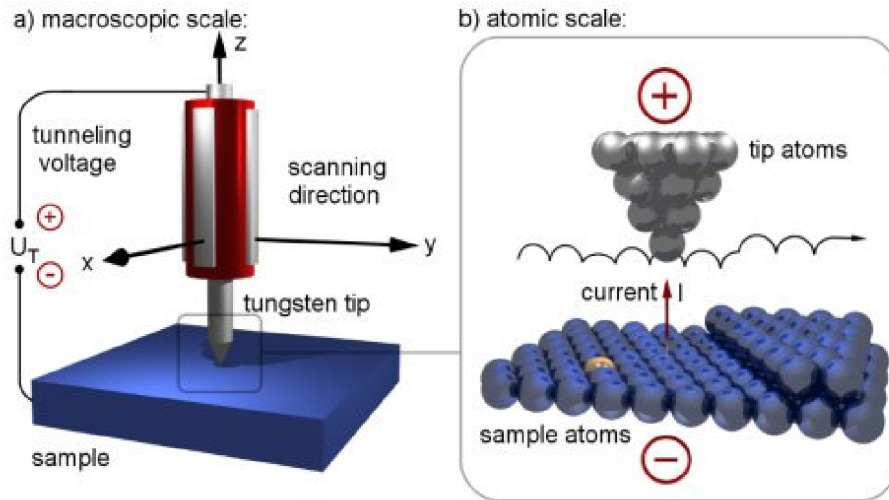
Fig. 1.1: Schematic view of a STM setup with a scanner and tungsten tip (a). View of a tip and sample at atomic scale (b).

1.2 Principles of Atomic Force Microscopy

The AFM methods are based on the force interaction between the atoms on the tip and a surface. The force interaction is detected by cantilever (tip holder) deflection. The acting forces between the atoms have different distance ranges (0.5 – 50 nm) and magnitude, according to the utilized sample and probe. The methods are known as very sensitive to the sample topography, chemical composition, and electric and magnetic properties. One of the critical parameters determining the ability of the methods are mechanical properties of cantilevers, which are available in a wide range of modifications (stiffness, size, and surface coverage). As for the sample and probe tip interaction, the five main forces can be identified:

- Van der Waals forces,
- capillary forces,
- chemical bonding forces,
- electrostatic forces,
- magnetic forces.

The forces between two atoms can be divided according to different criteria, e.g. to the long-range and short-range ones, or attractive and repulsive ones, etc. The total interaction can be approximated by the Lennard-Jones potential [6]:

$$U_{LJ}(R) = 4\varepsilon \left(\left(\frac{\sigma}{R} \right)^{12} - \left(\frac{\sigma}{R} \right)^{6} \right),$$
Eq. 1.1

14

where $U_{LJ}(R)$ represents the interaction potential between two atoms (molecules) depending on their distance R and $-\varepsilon$ is the value of the interaction potential in the minimum. The coefficient σ is determinated by the distance where the potential is zero. The Lennard-Jones potential is composed of a region where the repulsive forces expressed by the $(\sigma/R)^{12}$ term are dominant and a region of the attractive forces expressed by the $(\sigma/R)^{6}$ term. In Fig. 1.2 both regions are schematically shown.
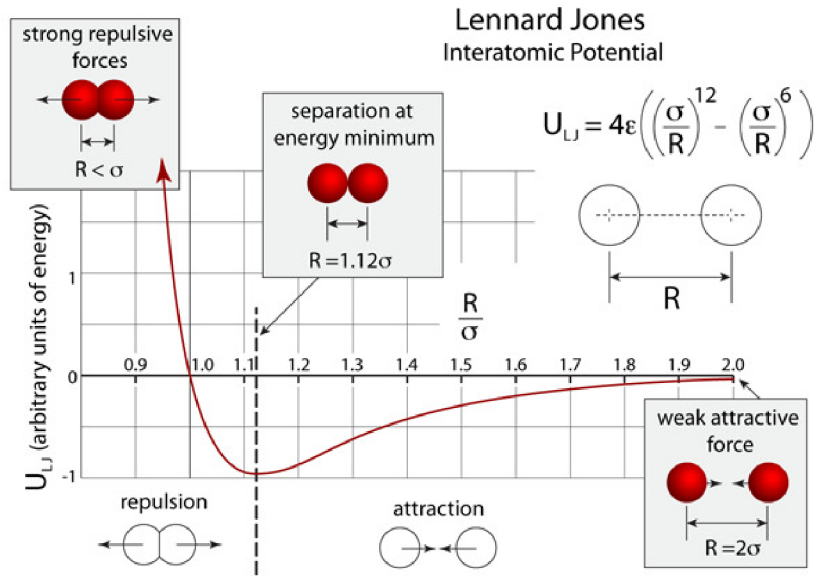
Fig. 1.2: Schematic interpretation of the Lennard-Jones potential, showing the main attractive and repulsive regions.

The total force acting between two atoms is expressed as the negative derivative of $U_{LJ}(R)$ according to R and hence

$$F(R) = -\frac{dU_{LJ}(R)}{dR}.$$

Eq. 1.2

The shape of the force $F(R)$ has a significant minimum which determines the basic modes of operation (Fig. 1.3). The contact and non-contact modes performed in the repulsive and attractive regions, respectively, utilize the local linearity of the $F(R)$. The intermittent (tapping) mode operate in both attractive and repulsive regimes as shown in Fig. 1.3. The non-contact and intermittent modes are also called as a dynamic or oscillatory modes based on their operation, when the cantilever oscillates close to its resonant frequency.
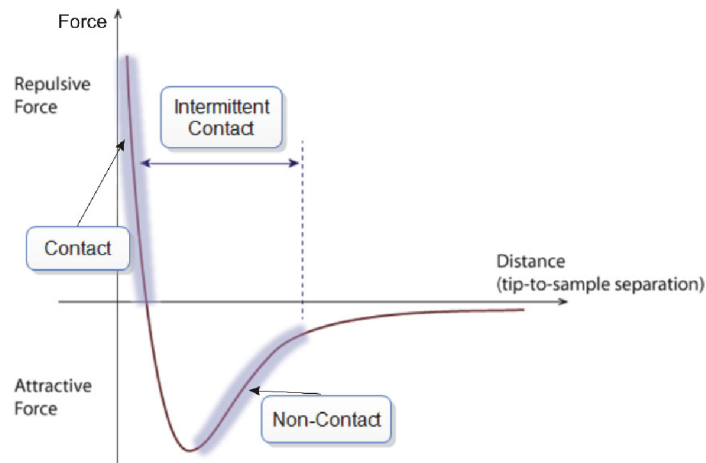
Fig. 1.3: Schematic illustration of the AFM operational modes having different working tip - sample distances.

1.3 AFM techniques

Interaction of the tip atoms with the sample ones is detected by a deflection of the AFM cantilever or a shift of the cantilever resonant frequency. Scanning the tip or sample in the XY direction enables the surface imaging. Hence, the basic set-up for all AFM techniques is composed of a XYZ scanning stage, detection system unit of the cantilever deflection, and electronics enabling to control the deflection set point or cantilever oscillations at resonant frequency. A schematic view of the typical AFM setup is shown in Fig. 1.4.

1.3.1 Contact mode

The force interaction is detected by the cantilever deflection in the distance where the repulsive forces are dominant. The applied force between the tip and the sample is typically in the range of nN units and can be determined from Hook's law reading $F = -kz$, where k is the cantilever stiffness and z is the displacement. One of the widely used methods of detection of the cantilever deflection is based on the shift of a laser beam reflected from the cantilever and detected by PSPD (Position Sensitive Photo-Diode). The contact-mode measurement can be operated in the regime of the constant height, where the signal representing the tip – sample interaction is proportional to the cantilever deflection during the X-Y scanning procedure. The second operating regime uses a PID (Proportional/Integral/Derivative) regulator and keep a constant deflection (force) by the movement of the scanner along the z-axis during X-Y scanning. The z-displacement then represents the topographical information about the sample. In Fig. 1.4 the contact mode is provided by the laser, photo diode, sample and cantilever. The control electronics for oscillation is not utilized. In the contact mode also Lateral Force Microscopy (LFM) can be carried out. The detected signal corresponds to lateral distortion of the cantilever. LFM mode provides the information about the surface adhesion between the tip and the sample, and, consequently, about various properties of the substrate itself.
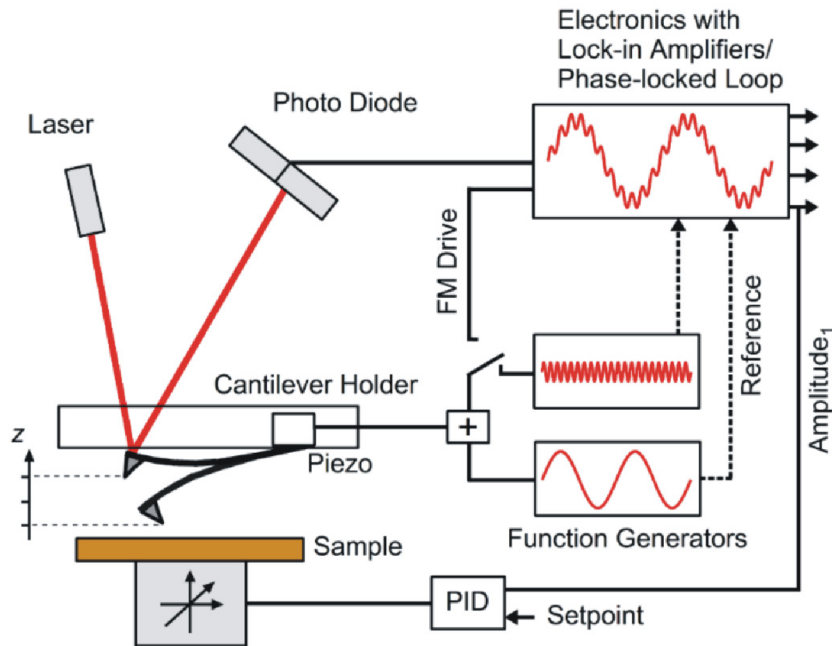
16

Fig. 1.4: Schematic view of an AFM set up with an optical detection unit, and electronics for oscillation- and sample position control [7].

1.3.2 Non-Contact mode

The force interaction can be determined also by the detection of the cantilever resonant frequency changes. The distance between the tip and the sample is kept in the range of the attractive forces in this mode. The experimental setup requires additional electronics for cantilever-oscillation control, it usually contains a lock-in amplifier enabling to excite cantilever oscillations at the required frequency and amplitude (Fig. 1.4). The typical amplitudes of cantilever oscillations in the non-contact mode are smaller than 10 nm and the resonant frequencies range from 30 to 1000 kHz, according to the cantilever stiffness. The cantilever oscillating at the resonant frequency is approached to the sample. The force interaction between the tip and the sample causes changes in oscillation frequency and amplitude. The resonant frequency shift is given by the approximate formula $\Delta\omega \approx (\omega_0 / k)(dF / dz)$, where ω_0 is the resonant frequency of a free cantilever, k is the cantilever stiffness and F is the interaction force between the tip and the sample [8]. Two different operating regimes can be set up: frequency modulation, where the PID regulator changes the scanner z axis to keep the frequency shift constant or the amplitude modulation, where the oscillation is set close to the resonant frequency and the change of the scanner z axis is to keep the oscillation amplitude the same.

1.3.3 Intermittent mode

The commonly used regime for the topographical imaging of surfaces is the intermittent (tapping) mode. In this mode the cantilever oscillates with a higher amplitude (10 – 100 nm)

than in the case of the non-contact mode. Here, both attractive and repulsive forces contribute to the tip-surface interaction. Information about the topography is acquired by the frequency or amplitude modulation, similarly to the non-contact mode [3].

1.3.4 Phase imaging

Additional information about the tip – surface interaction can be obtained from the phase lag of the cantilever oscillations relative to the excitation signal which is monitored and recorded while the feedback keeps the amplitude at a fixed value. This technique is used to obtain additional information during the tapping mode imaging. Topography and phase imaging are acquired simultaneously [3].

1.3.5 Other techniques

Both static and dynamic techniques can be also used for detection of magnetic and electrostatic forces between the tip and the sample. These methods are called MFM (Magnetic Force Microscopy) and EFM (Electrostatic Force Microscopy) [3]. They require special cantilevers coated with magnetic- and conductive layers, respectively. The principle is based on the long range effect of magnetic and electrostatic forces compared to the atomic ones. Hence, it is possible to isolate these long range interactions from the short range ones by enlargement of the distance between the tip and the sample. Another commonly used technique is KPFM (Kelvin Probe Force Microscopy) which enables to image the surface potential. The information about the potential is obtained by applying a special compensation bias voltage between the oscillating tip and the sample when the cantilever equilibrium deflection is kept constant during the scanning [3].

1.4 Development of UHV AFM at IPE BUT

As already mentioned above an UHV AFM/STM system was developed at the IPE BUT more a decade ago [5]. The developed instrument was designed as a part of a complex UHV system. The whole microscope with the feedthroughs for electric cables is placed on the UHV CF flange DN 150 as can be seen in Fig. 1.5. The microscope is composed of a measuring platform and an anti-vibration stage (Fig. 1.5).

18
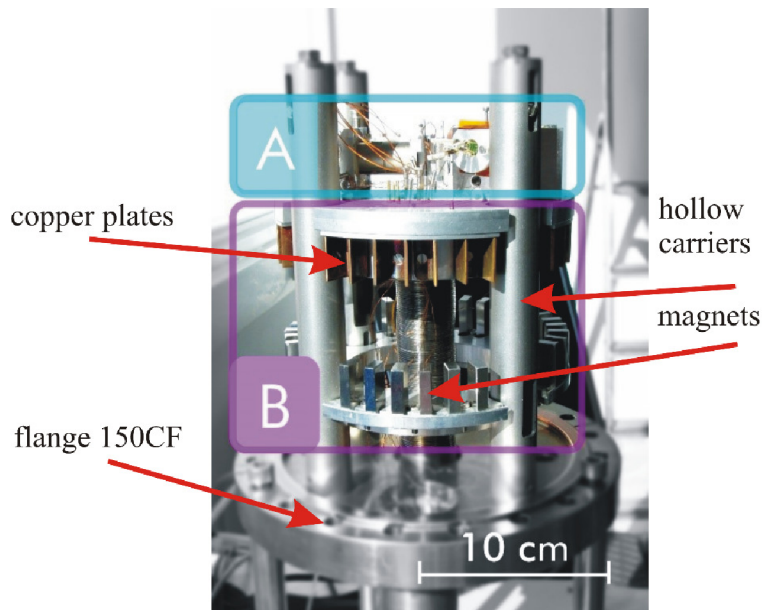
Fig. 1.5: UHV AFM/STM setup composed of a measuring head with a scanner and optical detection system (A) and anti-vibration stage with eddy current dumping (B).

This stage consists of four vertical tubes – carriers each of them having a spring inside not touching the inner tube wall and attached to the tube top. To reduce the transfer of vibrations from the flange, the platform is suspended on these springs. The resonant frequency of the platform on the springs is approximately 1.8 Hz [5]. Dumping of platform vibrations is achieved by the effect of eddy currents induced in the copper plates attached to the platform and moving at platform oscillations in an outer magnetic field generated by permanent magnets attached to the tubes. When no measurement takes place, the platform is locked in a rest upper position.

The measuring platform (Fig. 1.6) contains a macro-approach system, XYZ scanner and an optical system for detection of the cantilever deflection. The sample is inserted into a sample holder attached to the end of the scanner. The cantilever holder is attached to the optical detection system. The exchange of the sample and cantilever is provided manually by a wobble stick without breaking UHV conditions.
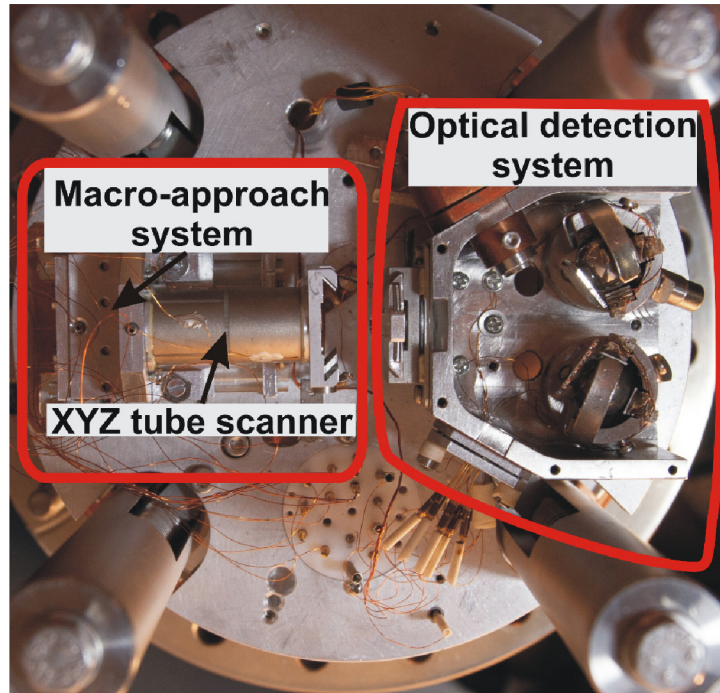
Fig. 1.6: Top view of the measuring platform with the highlighted parts such as a macro-approach system, scanner and optical detection system.

Macro approach is maintained by a linear slip-stick actuator which transports the XYZ piezo scanner. The macro approach works in the 1 cm-long range. The high voltage (300 V) wires are separated from the low-level signal wires connected to the detection unit. Both the piezo actuator and scanner are controlled by a newly developed electronics unit.

The optical detection system consists of a laser diode, two 3-axis rotary piezo actuators with glued mirrors and PSPD (Position Sensitive Photo-Diode). In Fig. 1.7a the optical path of the laser beam is marked. The beam is generated by the laser diode, than is reflected at the first adjustable mirror (glued to the rotary actuator) towards the cantilever. The beam is then reflected from the cantilever to the second adjustable mirror and from it continues to the PSPD. In such a configuration a deflection of the cantilever causes a movement of the laser spot on the PSPD. The 3-axis rotary actuator with the glued mirror is shown in Fig. 1.7b. A detailed description of the actuator and optimization of its movement in UHV conditions will be discussed in the separate part of this work.
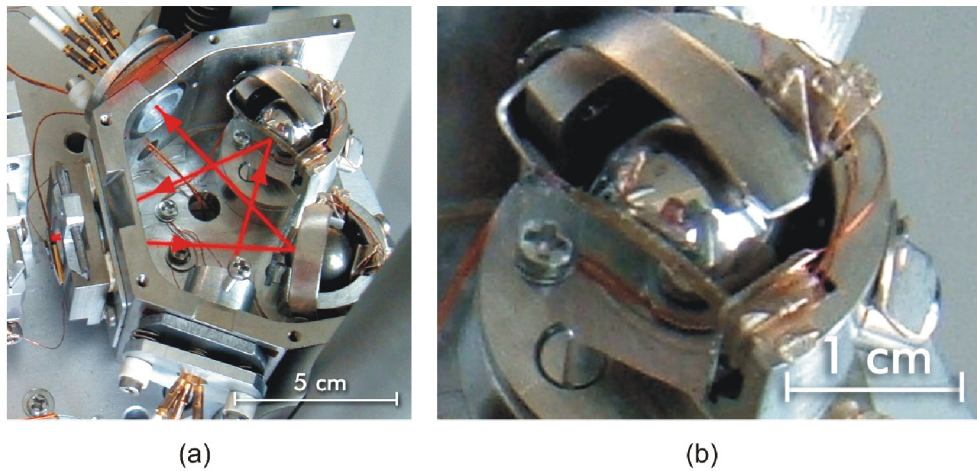
Fig. 1.7: Optical detection system with the marked laser-beam path (a). Adjustable mirror by the 3-axis rotary piezo actuator (b).

Within this PhD thesis, the original UHV AFM/STM instrument has been improved in several aspects. The original setup suffered from permanent problems connected with unreliable motion of the piezo actuators in UHV, stability of the laser diode, and old, not transferable electronics and software. The new electronic unit has been designed as a part of other PhD works by Z. Nováček, D. Šulc and P. Wertheimer and consists of the units for controlling the rotary piezo actuators, laser, PSPD and scanners. Macro approach originally provided by an inchworm motor was replaced by a linear slip-stick actuator designed by M. Pavera.

The most significant upgrade has been achieved by the utilization of the open-source control software GXSM communicating with a commercial control unit developed by the Soft DB company. This control unit was supplemented by a home built preamplifier for SPM signal detection and high voltage amplifiers for the scanner and piezo actuators operation. The proposed concept presents a good compromise between the cost and performance. The Open Source enables an additional extension of the control software which is an important advantage.

2. Optimization of the slip-stick piezo actuator motion

An impressive development of different precise analytical tools for surface science and nanotechnology research has been made in the last decades. A significant contribution to these results has been also achieved due to a progress in the precise positioning and actuating of samples, probes, and other tool elements. Micro- and nano actuators working with high accuracy and wide range of displacement, their fast response to the control signal, tunable displacement step and simple operation are the main features of the requirements laid upon these systems. Micro- and nano actuators generally utilize piezoceramics as the central part of their design. These piezoelectric actuators can be categorized according to their basic working principles [9] into the stepping inertial (slip-stick) actuators (also called the quasi-static actuators) [10-15] and the ultrasonic motors based on standing or propagating mechanical waves [16-18]. Special designs of actuators are also compatible with ultrahigh vacuum working conditions.

The angular slip-stick actuators rely on a difference in the static and dynamic friction force acting between the rotor and the stator [19], the setup of which works in a stepping mode. Within each step there is a period of the slow deformation of a piezoceramic plate during which the rotor and stator are in the sticking regime, and a period of the fast piezoceramic deformation providing the slipping regime between the rotor and the stator [14]. The deformation of piezoceramics is done by driving pulses, typically in a voltage range of 0.2 - 0.3 kV. This basic slip-stick principle is provided by simple and low cost designs and ensures relatively high-speed motion (~ 5mm/s), long-range displacement and the precise positioning with the accuracy below 5 nm [9]. To provide the stable and efficient operation of these actuators, it is crucial to find an adequate setup of optimum parameters such as the voltage, shape and frequency of driving pulses, load force and also materials ensuring appropriate friction coefficients, etc. [14].

The angular actuator tested in this paper is mounted in an UHV AFM setup and provides the alignment of a laser beam onto a cantilever and position sensitive photo detector (PSPD). To find the optimized parameters of this actuator, a simple testing system has been developed. It detects and records the angular motion of the actuator by PSPD in real time. The optimization is based on the measurement of the actuator response to driving pulses of various parameters being gradually changed by a computer software, at different load forces. To better understand and interpret the experimental results, supportive methods based on a simple analytical model and numerical simulations were used as well. Generally, this approach can be applied for testing and optimizing any linear or angular slip-stick actuator [20].

2.1 Optimization scheme

Motion of a slip-stick piezo actuator is generally controlled by the parameters related to its mechanical design and characteristics of the driving pulses applied to piezoceramic shear plates. An optimization of all parameters is necessary to reach the effective and stable

operation of the actuator. In the paper the procedure for the optimization of the actuator motion is proposed and tested on a rotary slip-stick piezo actuating system utilized in an atomic force microscope.

The optimization is based on the measurement of the actuator response to driving pulses of different shapes and repetition frequencies at various load forces. To provide it, a simple computer controlled testing system generating the driving pulses, and detecting and recording the corresponding angular motion response of the actuator by a position sensitive photo detector (PSPD) in real time has been developed. To better understand and interpret the experimental results, supportive methods based on a simple analytical model and numerical simulations were used as well.

In this way the shapes of the single driving pulses and values of the load force providing the biggest actuator steps were determined. Generally, the maximal steps were achieved for such a combination of the pulse shapes and load forces providing high velocities at the end of the sticking mode of the actuator motion and, at the same time, lower decelerations during the slipping mode.

As for the multiple driving pulses, the pulse shapes and values of repetition frequency ensuring the sticking mode of the actuator motion during the pulse rise time together with the maximum average angular rotor velocity were specified. In this way the effective and stable operation conditions of the actuator were provided.

In principle, the presented method can be applied for the testing and optimization of any linear or angular slip-stick actuator.

2.2 Actuator Setup

The actuator, the properties of which were optimized, is a three-axis rotary slip-stick piezo system designed according to [21]. Its cross section is shown in Fig. 2.1b. A couple of these actuators are used in an optical detection system of a cantilever deflection being a part of a home-built UHV STM/AFM unit. The unit provides the alignment of a laser beam with respect to an AFM cantilever and position sensitive photo detector (PSPD). The stator of the actuator is a right-angle 3D corner setup with three pairs of piezoceramic shear plates fixed to each corner wall with a UHV compatible glue (EpoTek H27D). A steel ball of a diameter of 10 mm with a glued mirror on it (EpoTek H27D) acts as a rotor. An Al-Ni-Co magnet protruding through the corner of the stator is used to control the load force by which the rotor acts upon the plates. Different load forces were chosen by setting specific distances between the magnet and the rotor sphere. For clarity, the forces are assigned in the paper as F_{load} 1 - 6. Only in the section devoted to the response to the multiple pulses the corresponding numerical values of the forces are specified as well, as they are needed in numerical simulations and fitting procedures.
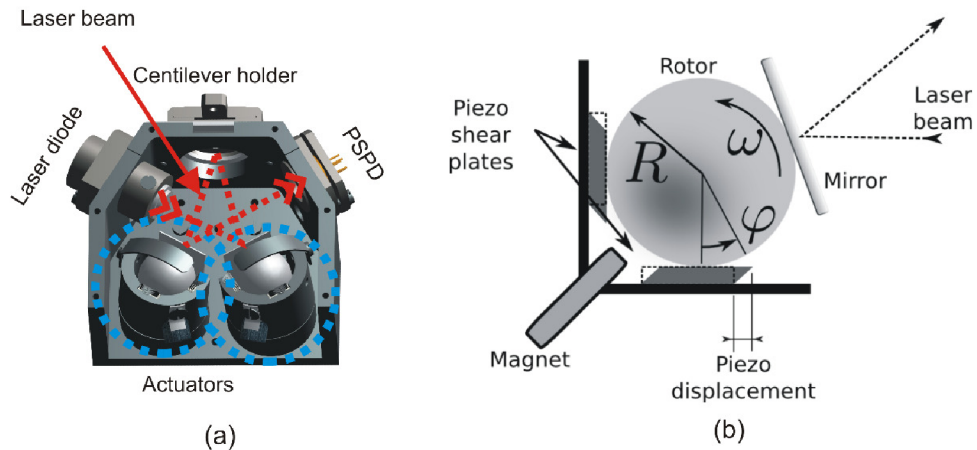
Fig. 2.1: A view of the optical detection system with a couple of the actuators used for the alignment of the laser beam with respect to the AFM cantilever and PSPD (a). Cross section of the three-axis rotary slip-stick actuator with the legend (b). For testing the actuator response the cantilever was replaced by a mirror.

2.3 Measurement setup

All the experiments for the optimization of the actuator operation were carried out with a measurement setup consisting of three basic parts as follows: an optical detection system, electronic system and control software.

The optical detection system is used to measure the angular displacement of an actuator and is identical with that one mentioned above (Fig. 2.1a) and which the actuator is part of. To modify such a system primarily developed for the detection of cantilever deflections in an AFM setup to this purpose, the cantilever just has to be replaced by a mirror.
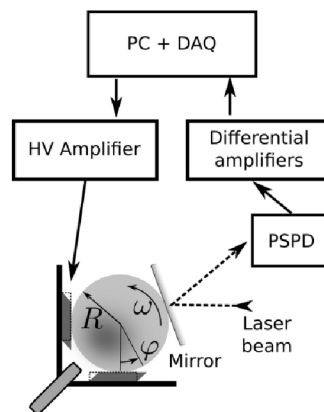
Fig. 2.2: Measurement setup for the optimization of the actuator motion.

In such a modified detection unit the laser beam generated by a laser diode with a collimating lens is reflected by mirrors to the PSPD. If the actuator is in motion, the laser spot is proportionally moving over the PSPD and the corresponding signal is used to monitor the displacement. The advantages of this technique can be listed as follows: almost no additional

load to the actuator (a small mirror can be used), high resolution (time development of a piezo-shear displacement during one single step can be observed – see Fig. 2.7), and non-contact remote measurements (e.g. through a view port of a vacuum chamber).
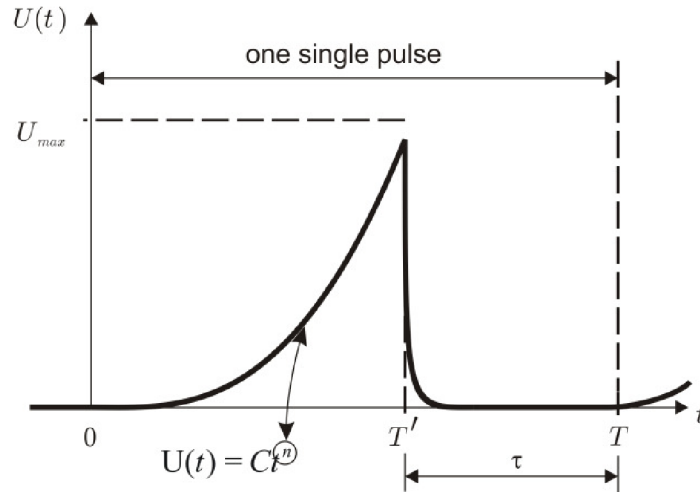

Fig. 2.3: Driving pulse put upon the piezoceramic shear plate. Pulse parameters: exponent n, rise time T', pause τ and period T.

The central part of the electronic system is a data acquisition computer card (DAQ). This card (NI 6221) with 800 kHz D/A sampling frequency was used to generate and measure all the pulses and signals, respectively (Fig. 2.2). The driving pulses processed by a D/A converter are led through a high voltage amplifier to piezoceramic shear plates. The high voltage amplifier [6] operating in the voltage range 0 – 1000 V consists of a low noise and low voltage op-amp driving high voltage MOSFET transistors to achieve the required amplification. The PSPD is a four segment photodiode. Two differential amplifiers provide output analogue signals giving information on the coordinates of the laser spot. These signals are consequently digitalized by DAQ.

The measurement itself consists of three consequent steps – specification of driving pulse parameters, measurement of actuator velocity, and saving the results.

The driving pulse parameters are defined in Fig. 2.3. The shape of the pulse is determined by the exponent n of the time function t^n, its rise time T' and the pause between two subsequent pulses τ. The period of the whole pulse is T. The repetition frequency f of the driving pulses is given by the reciprocal value of T as follows

$$f = \frac{1}{T} = \frac{1}{T' + \tau}.$$

Eq. 2.1

The power function of time was selected as it has two significant advantages. First, the mutual form of the equations of motion also has the form of a power function of time, which provides an option to drive the motor with e. g. constant acceleration. Second, its shape could

26

be varied from a convex through linear to concave one using one parameter only (exponent *n*).

At first approximation the displacement of the piezoceramic shear plate (Fig. 2.1) during its rise time ($t < T'$) is proportional to the voltage *U(t)* supplied to it:

$$s(t) \propto U(t) = \frac{U_{\max}}{T'^n} t^n ,$$

Eq. 2.2

where $U_{\max}$ is the maximal voltage brought to the piezoceramics. The relative actuator angular velocity is obtained from the time of the laser spot motion across PSPD and the corresponding voltage difference upon it.
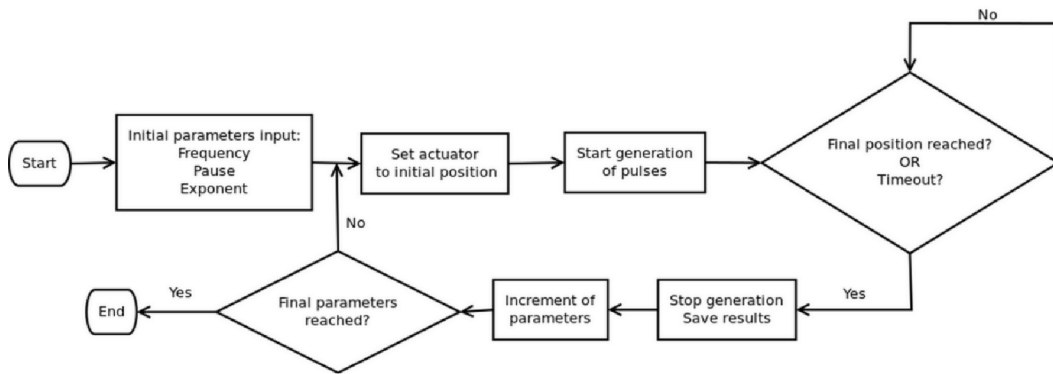
Fig. 2.4: Flow chart of the measuring software.

The measurement is controlled by a computer software written in the Python programming language using the NI-DAQmx driver [22]. The basic algorithm (Fig. 2.4) was improved by routines for controlling various situations that can occur (no actuator response to a selected pulse, backward motion, too slow motion, position correction along different axes, etc.). Therefore, a long term measurement cycle can be carried out automatically without operator's intervention.

The output file contains the pulse parameters and the corresponding values of the actuator velocity. This file is processed afterwards in order to find the optimal pulse parameters with respect to the actuator speed.

2.4 Simulation - numerical model

2D numerical simulations of the actuator response were carried out in the Matlab programming environment to better understand the experimental results. A schematic of the actuator model configuration is shown in Fig. 2.5. The main aim of the presented simulations was to find a theoretical response of the rotor to driving pulses put upon the piezoceramic plates of the stator.

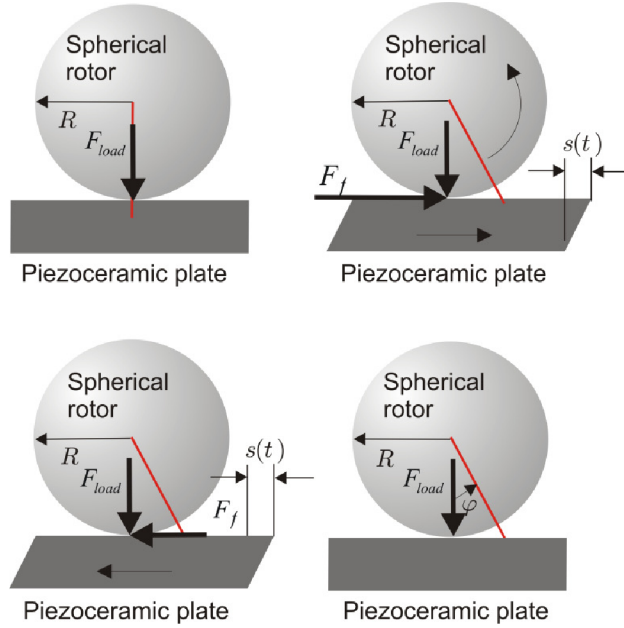Fig. 2.5: Schematic of a 2D actuator model configuration in 4 phases during one single step: (a) initial piezo plate position, (b) piezo plate forward motion, (c) piezo plate backward motion and (d) piezoceramic plate final position (R - rotor radius, F_{load} - load force, F_f - friction force, $s(t)$ - piezoceramic displacement, and $\varphi(t)$ - rotor angular displacement).

The rectangle representing a stator piezoceramic plate in the actuator moves horizontally forward and backward according to the driving signal. The transfer of the piezo motion to the rotor (sphere rotating around a fixed axis) is provided by the torque $M(t)$ caused by the friction force F_f between the spherical rotor and the piezoceramic plate. To calculate the response in form of the rotor angular displacement $\varphi(t)$, two distinct situations must be considered as follows:

2.4.1 Sticking mode

In this mode the acceleration of the rotor equals to the acceleration of the stator:

$$a_{rotor}(t) = a_{stator}(t)$$

Eq. 2.3

and so the rotor angular acceleration can be calculated as

$$\varepsilon(t) = \ddot{\varphi}(t) = \frac{a_{stator}}{R} = \frac{\ddot{s}(t)}{R} = \frac{M(t)}{I},$$

Eq. 2.4

where $s(t)$ is the displacement of the stator (piezoceramic plate) and R is the rotor radius. Knowing $\varepsilon(t)$, the torque $M(t)$ can be calculated from the basic relation

$$M(t) = \varepsilon I,$$

Eq. 2.5

where I is the rotor momentum of inertia. In the sticking mode the torque $M(t)$ must meet the following condition:

$$M(t) \leq M_{max} \qquad \text{Eq. 2.6}$$

with

$$M_{max} = F_{load} f_s R, \qquad \text{Eq. 2.7}$$

where F_{load} and f_s are the load force and static friction coefficient, respectively.

2.4.2 Slipping mode

In this mode the system is not able to transfer the torque $M(t)$ from the stator to the rotor as

$$M(t) > M_{max}, \qquad \text{Eq. 2.8}$$

and so

$$a_{rotor}(t) \neq a_{stator}. \qquad \text{Eq. 2.9}$$

One can calculate the rotor angular acceleration according to the formula

$$\varepsilon = \frac{M(t)}{I}, \qquad \text{Eq. 2.10}$$

where the torque is given by the time independent relation

$$M(t) = F_{load} f_d R, \qquad \text{Eq. 2.11}$$

where f_d is the dynamic friction coefficient.

2.5 Analytical model

To find an analytical formula for the actuator response (average rotor angular velocity $\overline{\omega}$) the repetition period T is divided into three time sections as shown in Fig. 2.6. In addition to the already specified symbols T and T' (Fig. 2.3) there is also the symbol T_d representing the right margin of a time interval Δt_d. Within this interval, defined by the relation $T' < t < T_d$, the rotor is slipping and slowing down due to dynamic friction until stops. The analytical model is valid only for the case when the sticking mode during the rise time ($t < T'$) takes place.
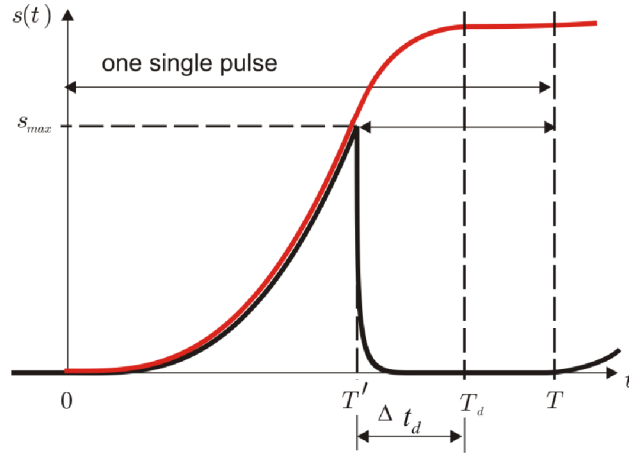
Fig. 2.6: Schematic view of the driving pulse (black) and actuator response (red) with three specific time sections defined by T', T_d and T.

The analytical description of the actuator angular displacement is given by the following equations for three distinct time intervals:

$$\varphi(0 < t < T') = \frac{s(t)}{R} = \frac{s_{max}}{R}\left(\frac{t}{T'}\right)^n, \qquad \text{(sticking mode)}$$

$$\varphi(T' < t < T_d) = \varphi(T') + \omega(T')(t - T') - \frac{1}{2}\varepsilon_d(t - T')^2, \qquad \text{(slipping mode)}$$

$$\varphi(T_d < t < T) = \varphi(T_d), \qquad \text{(resting mode)} \quad \text{Eq. 2.12}$$

where the exponent n meets the condition $n \geq 2$, s_{max} is the maximal piezoceramic displacement and ε_d is the actuator deceleration occurring within the time interval Δt_d and obtained from Eq. 2.10 and Eq. 2.11 as follows

$$\varepsilon_d = \frac{F_{load} f_d R}{I}. \qquad \text{Eq. 2.13}$$

The deceleration interval Δt_d defined by the relation $T' < t < T_d$ can be calculated by

$$\Delta t_d = \frac{\omega(T')}{\varepsilon_d}. \qquad \text{Eq. 2.14}$$

The analytical expression for the average angular velocity $\overline{\omega}$ is defined as

$$\overline{\omega} = \frac{\varphi(T)}{T} \qquad \text{Eq. 2.15}$$

and derived using additional Eqs. (resting mode) Eq. 2.12, Eq. 2.13, and Eq. 2.14 reads

30

$$\overline{\omega} = \frac{s_{max}}{RT} + \frac{I}{2F_{load}f_d RT} \omega(T')^2 .$$

Eq. 2.16

Eq. 2.16 shows up the linear dependence of $\overline{\omega}$ on the square of the actuator angular velocity at the time T', i.e $\omega(T')^2$. The average angular velocity $\overline{\omega}$ also depends on the set of parameters representing the actuator design and defining driving pulse as well.

In the analytical model the sticking mode is supposed to be valid for all the times $t \le T'$, which means the torque M related to the instantaneous angular acceleration ε by Eq. 2.5 is not higher than the maximal torque M_{max} (Eq. 2.6 and Eq. 2.7). In this mode the corresponding maximum angular acceleration ε_{max} is achieved at $t = T'$ and can be calculated as

$$\varepsilon_{max} = \varepsilon(T') = \ddot{\varphi}(T') = \frac{s_{max}}{R} \frac{n(n-1)}{T_c'^2}$$

Eq. 2.17

and using Eq. 1.1 it can be expressed by

$$\varepsilon_{max} = \frac{s_{max}}{R} n(n-1) \left(\frac{1}{f_c} - \tau \right)^{-2} ,$$

Eq. 2.18

where T_c' and f_c is the critical minimal rise time and maximal frequency, respectively, of the given actuator which can be used while keeping the sticking mode during the pulse rise time for a given driving pulse shape. One can get expression for the critical frequency f_c from Eq. 2.18 as follows:

$$f_c(n) = \frac{1}{\tau + \sqrt{A^{-1}n(n-1)}} ,$$

Eq. 2.19

where A is given by the relation

$$A = \varepsilon_{max} \frac{R}{s_{max}} = \frac{F_{load}f_s R}{I} \frac{R}{s_{max}}$$

Eq. 2.20

and depends only on the actuator design.

Similarly, the maximal angular velocity ω_{max} and so its maximal average value $\overline{\omega}_{max}$ (see Eq. 2.16) is achieved when the critical frequency $f_c(F_{load}, n, \tau)$ is chosen.

2.6 Results and discussions

The goal of this work was to find the optimal parameters of the driving pulses to reach the stable actuator motion at a maximum speed. To do it, the results achieved from experiments, simulations and analytical model have been utilized.

2.6.1 Response to a single driving pulse

The resolution of the optical detection system allows us to measure the actuator response to a single driving pulse. The response to a single pulse was measured by using a sequence of pulses with a relatively long pause between the pulses ($\tau = 10$ ms) and repetition frequency $f = 94$ Hz. Different load forces (F_{load}) and pulse shapes (exponent n) were applied here. The temporal record of the actuator response to various single pulses measured for distinct load forces is shown in Fig. 2.7. The dependence of the actuator angular displacement at $t = T_d$ (actuator step) on load forces is depicted in Fig. 2.8.
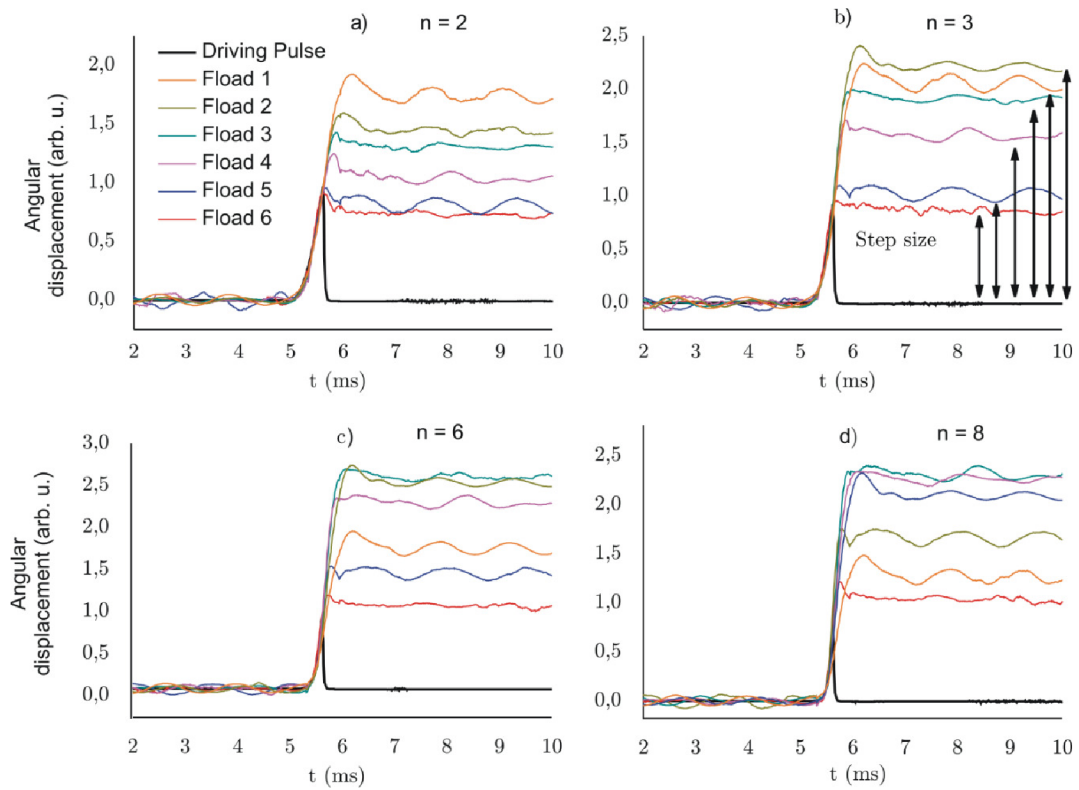

Fig. 2.7: Actuator response expressed by the PSPD signal (proportional to the angular rotor displacement) to the single driving pulses (black curves) with $f = 94$ Hz and $\tau = 10$ ms for six incremental load forces ($F_{load}1$ – the smallest force) and four driving pulses of the shapes given by the exponents (a) $n = 2$, (b) $n = 3$, c) $n = 6$, and (d) $n = 8$.

In case of the exponent 2 (Fig. 2.7a), the rotor response follows the driving pulse during the sticking phase ($t \leq T'$) for all load forces. A significant difference in the actuator response is observed for distinct F_{load} at $t > T'$. The higher load forces result in smaller displacements (Fig. 2.7a and Fig. 2.8) due to higher friction forces and thus more intense deceleration in the deceleration phase. Hence, the maximal displacement at $T = T_d$ for $n = 2$ is achieved for the smallest load force ($F_{load}1$). The actuator response to sharper pulses having the exponents 3, 5, and 8 (Fig. 2.7b - d) differs for distinct load forces in the time phase $t > T'$ as well. However, the maximum displacements for these pulses were obtained for bigger load forces ($F_{load}2$ and $F_{load}3$) compared to the pulse with $n = 2$ (Fig. 2.8). The bigger forces allow us to

32

achieve higher instantaneous velocity at T' as they better provide the sticking mode of the actuator at $t < T'$. In addition to that, for the sharper pulses even the bigger load forces do not already protect the rotor from slipping at $t > T'$ and, hence, its deceleration is not so efficient compared to the pulses with $n = 2$. It is obvious from Figs. 7 c, d that for the curves with $n = 5$ and 8 the rotor starts to slip for F_{load} 1 at $t < T'$. The biggest actuator steps were achieved for the driving pulse with $n = 6$ and load force F_{load} 3 (Fig. 2.8).
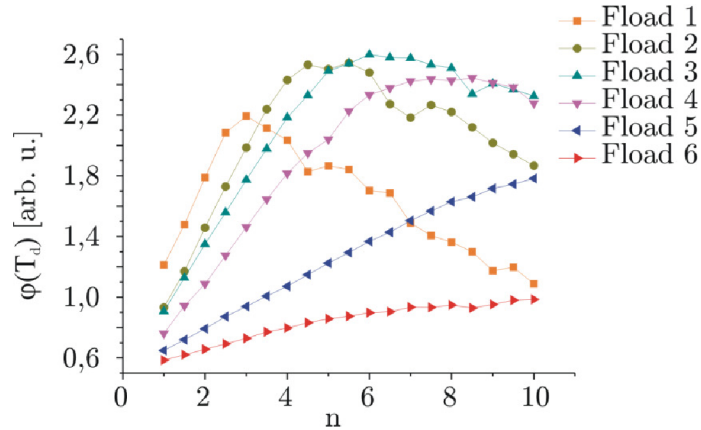

Fig. 2.8: Actuator angular displacement at $t = T_d$ obtained from the single pulse measurements as a function of the pulse shape (exponent n) for incremental load forces F_{load} 1 - 6, the same pulse repetition frequency and pause between pulses as defined in Fig. 2.7.

The analytical model predicts the linear relation between the average angular velocity $\overline{\omega}$ and the second power of instantaneous angular velocity at T' for a single pulse (Eq. 2.16). The experimental relationships between these two quantities for single pulses of various shapes (exponent n) and different load forces F_{load} 1 - 6 are presented in Fig. 2.9. Here, each experimental point corresponds to the pulse with an exponent from the interval $n = 1$ - 10. The data were processed using the Savitzky-Golay high pass filtering [23]. In accordance with Eq. 16 the data can be fitted by the linear relation

$$\overline{\omega} = a + b\omega(T')^2,$$
Eq. 2.21

where a and b are the constants. The constant b is determined from the individual experimental curves obtained for specific load forces F_{load}. The higher load forces lead to smaller line slopes b, which is in agreement with the formula

$$b = \frac{I}{2F_{load}f_d RT},$$
Eq. 2.22

resulting from Eq. 2.16. This analytic formula can be for instance used for the calculation of the dynamic friction coefficient.
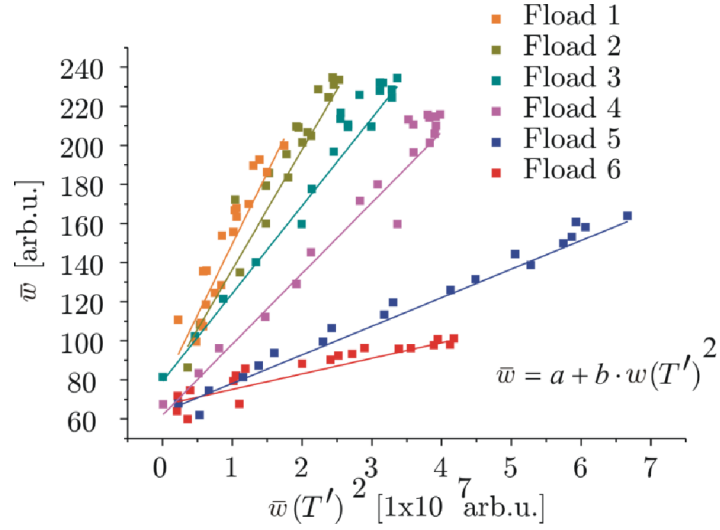
Fig. 2.9: Experimental dependence of the average angular velocity $\bar{\omega}$ on the second power of the instantaneous angular velocity of the actuator at T', i.e. $\omega(T')^2$, for the pulses of various exponents (n = 1 - 10) and different load forces F_{load}. Repetition frequency of the pulse sequence was f = 94 Hz and pause τ = 10 ms.

2.6.2 Response to multiple driving pulses

The actuator motion is provided by a sequence of individual pulses. Therefore, in addition to the single pulse response it also depends on the repetition frequency f of the single pulse and the pause τ between two consequent pulses. Hence, all the relevant parameters have to be optimized simultaneously to reach the maximum average velocity. The experimental and simulated (numerical model) maps of the average angular rotor velocity as a function of pulse frequency and shape for three different load forces F_{load} are presented in Fig. 2.10. In the simulations the friction coefficients f_s = 0.3 and f_d = 0.1 were chosen according to [24]. To avoid the direct influence of the neighboring pulses, the pause τ between each pulse should be longer than the deceleration time Δt_d. The deceleration time Δt_d in the multiple-pulse experiments was in the range 0.1 – 0.8 ms and, hence, the pause in the measurement and simulation of average angular velocity $\bar{\omega}(n, f)$ was chosen 1 ms.
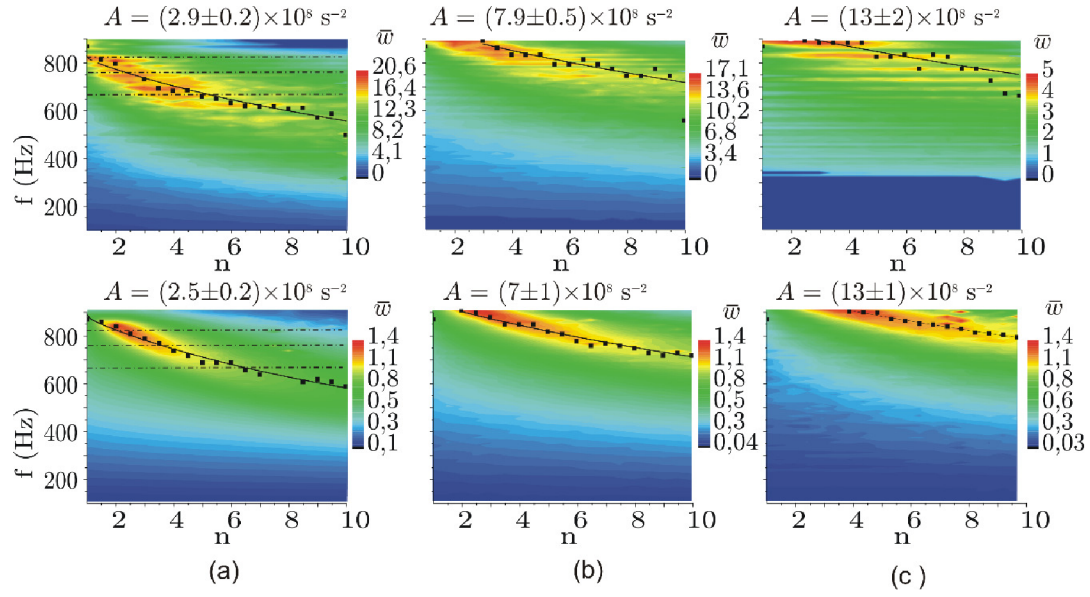
Fig. 2.10: Experimental (upper row) and simulated (bottom row) *f-n* maps of the rotor average angular velocity $\bar{\omega}$ (arb. u.) for the pause between the pulses τ =1 ms and load forces (a) F_{load} 1 ($\approx$0.1 N), (b) F_{load}2 ($\approx$0.3 N) and (c) F_{load}3 ($\approx$0.35 N). The fitting parameter A (defined by Eq. 2.20) is shown for each experimental and simulated map. Frequencies marked by dash-dotted lines: f_{1m} = 655 Hz, f_{2m} = 763 Hz, and f_{3m} = 830 Hz.

Both in the experimental and simulated maps the areas of the maximal values of the actuator average angular velocity $\bar{\omega}_{max}$ are remarkable. At the same time, there is a very good agreement between the experiment and simulations. In the maps, the maximal average velocities $\bar{\omega}_{max}$ for the corresponding exponents *n* are represented by dots which are then fitted by the curves given by the relation for the critical frequencies obtained from the analytical model (Eq. 2.19). The resulting fitting parameters A both for the experimental and simulated maps are shown in Tab. 2.1.

	F_{load} 1 [0.1 N]	F_{load} 2 [0.3 N]	F_{load} 3 [0.35 N]
	A [$10^8 s^{-2}$]		
Experiment	2.9 ± 0.2	7.9 ± 0.5	13.0 ± 2.0
Simulation	2.5 ± 0.2	7.0 ± 1.0	13.0 ± 1.0

Tab. 2.1: Fitting parameters A for the multiple pulse measurements and numerical simulations of $\bar{\omega}_{max}(n,f)$ for three different load forces F_{load}.

The fitting curve in each map separates two areas of different operational modes during the pulse rise time ($t < T'$). The parameters f and n determining the points below the curve provide the sticking mode, meanwhile those above the curve the slipping mode. From the

shape of the curves it is obvious that to keep the sticking mode during the pulse rise time at higher repetition frequencies the lower coefficients n must be chosen.

Comparison of the dependence of average velocity $\overline{\omega}$ on the pulse shape (exponent n) obtained from the single-pulse experiments, multiple-pulse measurements (Fig. 2.10, upper row) and numerical simulations (Fig. 10, lower row) is presented in Fig. 2.11 for the applied load force F_{load} 2 ($\approx$0.3 N) and different pulse frequencies. For the single pulses these frequencies were $f_{1s} = 95$ Hz, $f_{2s} = 97$ Hz, and $f_{3s} = 98$ Hz, and for the multiple pulses (both experimental and simulated) $f_{1m} = 655$ Hz, $f_{2m} = 763$ Hz, and $f_{3m} = 830$ Hz (marked in Fig. 10a by dash-dotted lines). Taking into account the pause $\tau = 10$ ms for the single pulses and $\tau = 1$ ms for the multiple ones, the shape and length of the pulses of the relevant frequencies f_{is} and f_{im} (where i=1, 2, 3) are identical. Hence, the actuator response to these pulses can be directly compared. The qualitatively same curve shapes possessing maxima at the same values of n have been obtained for all these three different repetition frequencies of pulses.
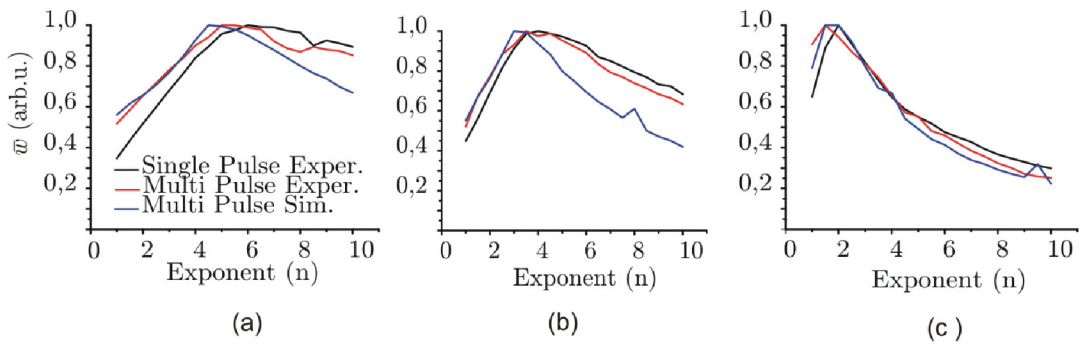

Fig. 2.11: Average angular velocity of the actuator as a function of the pulse shape for a single-pulse experiment (τ=10 ms), and multiple-pulse measurements and numerical simulations (τ=1 ms) for a) $f_{1s} = 95$ Hz, $f_{1m} = 655$ Hz, b) $f_{1s} = 97$ Hz, $f_{1m} = 763$ Hz, and c) $f_{1s} = 98$ Hz, $f_{1m} = 830$ Hz. Applied load force F_{load}2 ($\approx$0.3 N).

The multiple-pulse curves obtained from cross sections of the maps in Fig. 2.11 at corresponding frequencies (see dash-dotted lines there).

2.7 Conclusion

The method for the optimization of slip-stick actuator motion has been proposed and successfully tested on the rotary slip-stick piezo actuating system being a part of the UHV STM/AFM unit. The optimization is based on the measurement of the actuator response to driving pulses of different shapes and repetition frequencies at various load forces. To carry out this task, a simple computer controlled testing system has been developed. It consists of an electronic unit and control software making possible to gradually change the pulse parameters, and optical detection system based on PSPD providing real time detection of the angular motion of the actuator.

Experimental measurements of the actuator response to single driving pulses showed the strong influence of the pulse shape given by exponent n and load force F_{load} on the final actuator step size (angular deflection). The maximal steps were achieved for such a combination of the pulse shapes and load forces providing high instantaneous velocities at the end of the sticking mode of the actuator motion ($t = T'$) and , at the same time, lower decelerations during the slipping mode ($t > T'$). These experiments also confirmed the linear relation between the average angular velocity $\bar{\omega}$ and square of instantaneous angular velocity at $t = T$ (time of maximal piezo displacement), as predicted by the theoretical model. This formula can be used for finding actuator material characteristics, for instance the dynamic friction coefficient.

Actuator response to the multiple driving pulses, both experimental and simulated, was presented in the form of maps of the average angular rotor velocity $\bar{\omega}(n, f)$ as a function of the pulse shape and frequency. Both the experimental and simulated maps show a very good correspondence. By fitting the maximal values of $\bar{\omega}(n, f)$ in the maps by a curve meeting the theoretical relation for the critical frequency, the phase area (n, f) providing the sticking mode during the pulse rise time ($t < T'$) can be separated from that one typical for the slipping mode. In addition, the parameters A typical for the actuator design were determined by this fitting procedure as well.

Finally, the comparison of the dependence of average velocity $\bar{\omega}$ on the pulse shape obtained from single-pulse experiments, multiple-pulse measurements and numerical simulations was presented. The qualitatively same curve shapes possessing maxima at the same values of n were obtained for equivalent repetition frequencies in case of all these three methods.

Generally, the proposed method can be applied for testing and optimizing any linear or angular slip-stick actuators.

3. Morphological changes of metallic films at elevated temperatures

Rapid development in the areas of nanotechnology and surface science achieved in the recent decades has led to number of procedures for preparation and characterization of nanostructures [25-30]. Utilization of gold nanoparticles on insulating or semiconducting supports lays in focus of research interests of many groups pursuing different applications. In this work we have investigated the thermally induced changes of gold thin films evaporated on silica substrates. Before discussion of experimental results, the main process involved in the morphological changes at elevated temperatures is described and discussed.

Thermal evaporation of gold on a chemically inert silica substrate leads to formation of a polycrystalline film. The layers were prepared at room temperature at which motion of individual atoms is restricted and structures far from equilibrium are obtained. Annealing of these films below the melting temperature (1063 °C) induces spontaneous processes accompanied with morphological changes of the surface. The main involved processes are diffusion, solid state dewetting, island crystallization and the Ostwald ripening.

The changes in morphology require the mass transfer, which can be described by thermodynamics. The motion of gold atoms occurs either within the object (self-diffusion) or between the two separated objects (surface diffusion) [25]. Both diffusion processes significantly differ in the length and time scale. As an example the fast atom diffusion at the island perimeter compared to the slow atom exchange between the islands can be given. In the other words, the islands are in thermodynamics equilibrium despite the fact that the surface is not in equilibrium at the large scale [31].

Let us define the chemical potential of the surface μ as the free energy change when one atom is add or remove from the system. The mass transfer observed during the annealing can be then described by the generalized form of Fick´s first law, where the transform equation that relates the particle current $\vec{J}$ to the gradient in the chemical potential [31] μ can be written as

$$\vec{J} = -L_D \nabla \mu, \qquad\qquad \text{Eq. 3.1}$$

where L_D is the transport coefficient for diffusion.

The driving force of the transformations is then a reduction of the free energy by moving the atoms. The relation between the local curvature and the chemical potential of a structure is described by the Gibbs – Thomson formula

$$\mu = \mu_0 + \kappa \gamma \Omega, \qquad\qquad \text{Eq. 3.2}$$

where, μ_0 is the chemical potential of the flat surface, κ is the local curvature ($1/R$), γ is the surface tension and Ω is the volume of an individual atom. The atom flux $\vec{J}$ can occur

in islands (self-diffusion) or can induce a mass transfer between the separated islands (Ostwald ripening). The flux of the atoms during the self-diffusion within the single island is schematically shown in Fig. 3.1a.

As an application example of thermodynamics principles is the transformation of a gold thin film induced by elevated temperatures [32-36]. In the case of the gold film with the nominal thickness below 20 nm deposited on a silica substrate, the voids and holes are already present in the film as it possesses the so called percolated structure. The process of surface transformation at elevated temperatures caused by the capillary forces and the gradient of the chemical potential is called wetting/dewetting and is schematically shown in Fig. 3.1. The capillary forces are induced at the interface between the gold and the silica surface, which have different surface energies. The conditions of equilibrium require a relation between the surface- and interface tensions and the corresponding angles Fig. 3.2. The transformation can be described as a process driving the surface evolution to equilibrium.

(a)   (b)
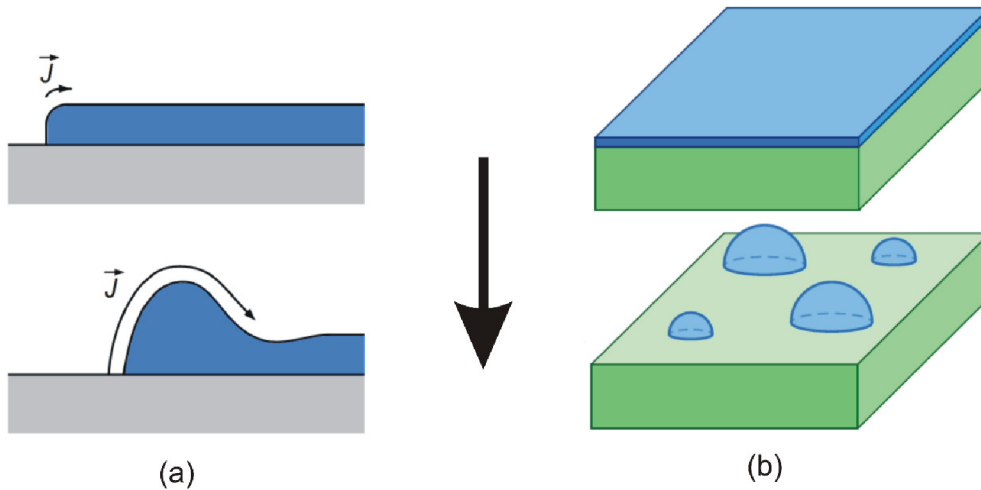
Fig. 3.1: Schematic illustration showing the retraction of an edge and development of a rim (a). Illustration of the dewetting process and islands formation (b). Both images taken from [37].

In the special case of a flat surface the equilibrium is described by the Young equation as follows

$$\gamma_s = \gamma_i + \gamma_f \cos\theta,$$

Eq. 3.3

where θ is the equilibrium contact angle between three-phase boundary, γ_s is the substrate surface tension, γ_f is the film surface tension and γ_i is the film-substrate interface tension (Fig. 3.2a). In the case that substrate is not rigid, the equilibrium of the islands is given by the relations

$$\gamma_s = \gamma_f \cos\theta_1 + \gamma_i \cos\theta_2$$

Eq. 3.4

and

$$\gamma_f \sin\theta_1 = \gamma_i \sin\theta_2,$$
<div align="right">Eq. 3.5</div>
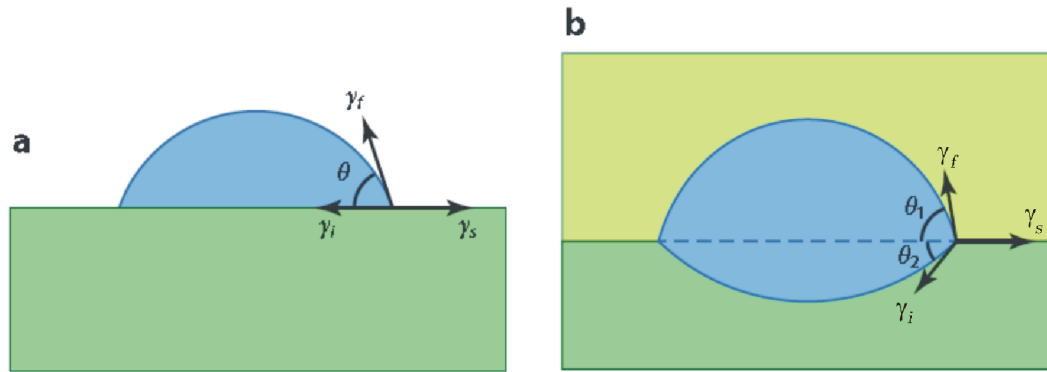
where θ_1 and θ_2 are angles shown in Fig. 3.2b.

Fig. 3.2: Schematics of a metal island in an equilibrium shape on a rigid surface with the contact angle θ and surface tensions γ_s, γ_f and γ_i (a), and on a not rigid substrate with the contact angles θ_1 and θ_2 (b).

A detailed study of the dewetting process and especially behavior of thin metallic films on SiO_2/Si substrates at elevated temperature was reported by Thompson [38, 39]. A similar observation on a glass substrate was also reported by Rubinstein and Vaskevich [40, 41]. They have shown that the dewetting temperature and the size of the formed islands are strongly influenced by the initial film thickness, as shown in Fig. 3.3.

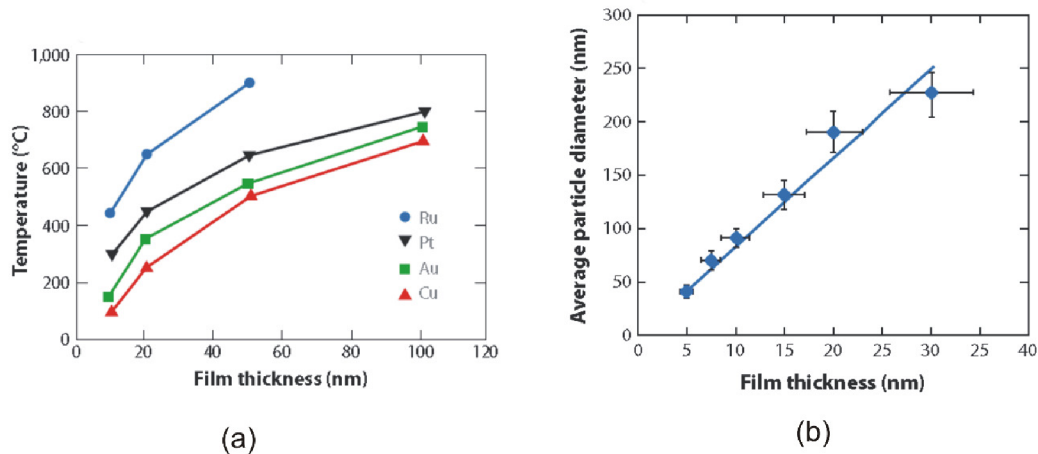(a)   (b)

Fig. 3.3: Dependence of dewetting temperature as a function of film thickness for four different metals (a). Average particle size as a function of film thickness of fully dewetted Ag films (b). Taken from [25].

At elevated temperatures the crystallization of the metal film has to be taken into account. For the crystalline material, the surface tension depends on the crystallographic surface planes - facets. The minimization of the Helmholtz surface free energy depending on the surface tension γ is the main driving force of the formation of metallic crystals [31]. The shape of the crystal with the minimal surface free energy can be determined for the anisotropic surface by the Wullf construction. [31].

The crystallization process of a gold thin film evaporated onto a silica substrate is initiated at relatively low temperatures, slightly above 180 °C. The crystallization causes the formation of faceted crystals, where the preferential orientation of the facets is (111). Even though the shape of the crystal influences the chemical potential (Eq. 4.2) and the diffusion process, the contribution of the crystallization is not assumed as a dominant effect.

Additional significant changes caused by the Ostwald ripening process are observed during annealing of the gold layer at a temperature of 1000 °C. Compared with dewetting and crystallization the Ostwald ripening is a slow process. Description of this phenomenon was first made by Wilhelm Ostwald in 1896 and then the theory was significantly extended by Lifshitz, Slyozov and Wagner 1961, so called LSW theory [42]. The proposed and experimentally confirmed model is based on a non-equilibrium state of particles which is followed by a transfer of gold atoms from the smaller particles (bellow the critical radius R_c) to the bigger ones (bigger than R_c). The gold atom transfer is mediated by surface diffusion. The schematic illustration of the island size evolution is shown in Fig. 3.4.
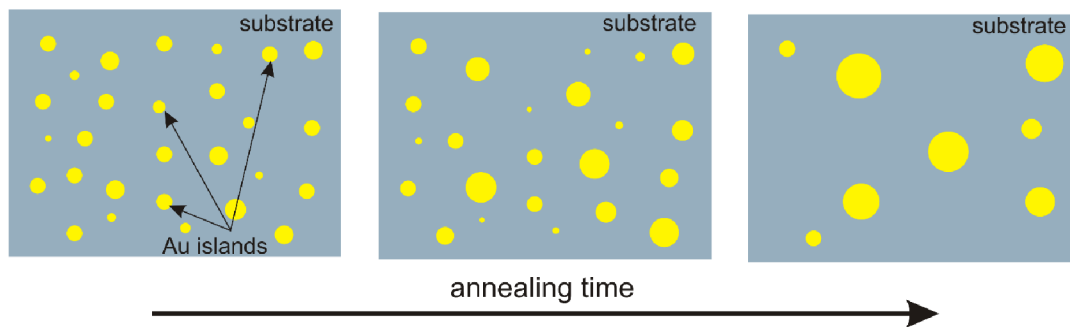

Fig. 3.4: Schematic illustration of the time evolution of island sizes caused by the Ostwald ripening process.

Using the classical approach LSW shows that the equilibrium concentration of atoms C_r at the grain boundary depends on the particle radius

$$C_r = C_\infty + \frac{\alpha}{R},$$
Eq. 3.6

where C_∞ is the atomic concentration of the saturated solution, R is the particle radius, $\alpha = (2\sigma / kT)\Omega C_\infty$ is the parameter containing interphase surface tension σ, Boltzmann constant k, temperature T and volume of the single atom Ω. The flux of atoms j between the islands can be expressed as

$$j = \frac{D}{R}\left(\Delta - \frac{\alpha}{R}\right),$$

Eq. 3.7

where D is the diffusion coefficient of atoms and Δ is $C - C_\infty$ [42].

The particle size distribution is characterized by $f(R,t)$ defined as the number of particles of the size R per unit volume at time t and therefore, the time rate of a change of f is given by the continuity equation

$$\frac{\partial f}{\partial t} = -\frac{\partial}{\partial R}\left(f\frac{dR}{dt}\right),$$

Eq. 3.8

where the time evolution of the radius corresponds to the flux of atoms and can be thus expressed according to Eq. 4.5 by

$$\frac{dR}{dt} \approx \frac{D}{R}\left(\Delta - \frac{\alpha}{R}\right).$$

Eq. 3.9

Another approach for description of the Ostwald ripening is based on the rate of attachment and detachment of atoms to/from the islands. Utilization of the approach was done by Zhadov in [43], where he showed that the surface heterogeneity can induce a bimodal distribution of the island sizes. The surface heterogeneity can be induced either spontaneously or prepared by a nanofabrication process. The influence of the surface modification on the Ostwald ripening can be explained as follows. The number of atoms N in individual islands is evolving during the time and can be expressed by

$$\frac{dN}{dt} = W_a - W_d,$$

Eq. 3.10

where W_a and W_d are the attachment and detachment rates. The activation energy ΔE for an atom detachment is given by the contribution of surface tension and curvature island and can be expressed as

$$\Delta E = -\frac{2\gamma\Omega}{R},$$

Eq. 3.11

where γ is the surface tension and Ω is the atomic volume and R is the local radius of the surface. Thus the surface modification affect the activation energy required for the atom detachment which results in splitting the size distribution function into two parts. The time evolution of each size distribution sub-function is then independent. The impact of the surface modification is shown in Fig. 3.5 where the bimodal size distribution is formed.
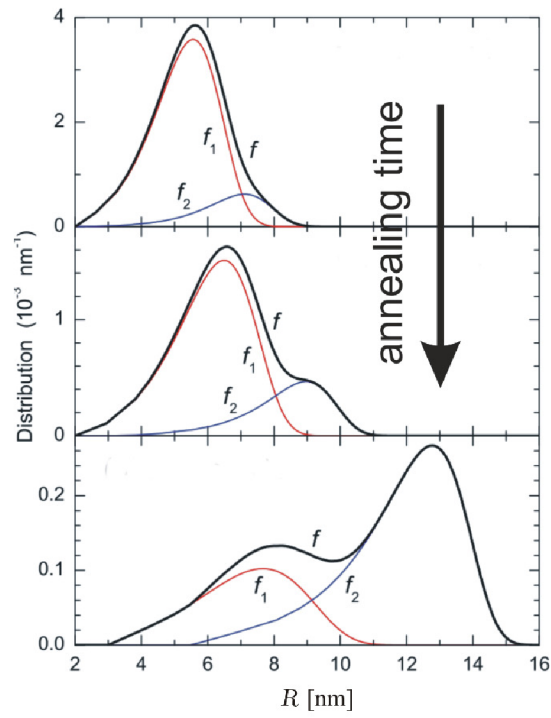
Fig. 3.5: Time evolution of the average radius of islands with different activation energies resulting in the distinct size distribution sub-functions f_1 and f_2. Taken from [43].

4. Solid-state dewetting of gold layers on the pre-patterned substrates

Metallic nanoparticles are of a great interest for a broad range of applications, e.g. in plasmonics (biosensing), for magnetic memory media, growth of nanowires and nanotubes, and as a catalyst. Utilization of nanoparticles in these fields requires development of procedures enabling the full control of the fabrication process. The metallic nanoparticles can be also prepared on surfaces by solid-state dewetting of thin metallic layers. One of the current challenges in the research is positioning of nanoparticles and precise control over their size. My research has concentrated on the preparation of ordered arrays of gold nanoparticles (islands) with a definite shape and size using solid-state dewetting of thin layers on the pre-patterned surface.

Recently, the groups of Carl V. Thompson [25-27, 44] and Peter Schaaf [28, 29, 45, 46] have made an impressive progress in this field. They have fabricated well separated ordered arrays of gold islands on patterned surfaces by thermal annealing. They have shown that topographical modification of a surface can be employed to control the solid-state dewetting process. The mechanism is based on differences in the chemical potential of the substrate, depending on the surface curvature given by the Gibbs-Thomson relation. Hence, gold islands were formed in the areas with the minimal chemical potential.

According to the theory of solid-state dewetting, the transformation of the continuous metal layer into islands starts with the formation of holes and voids. The metallic film of a thickness $5 - 20$ nm [40, 47, 48] prepared by evaporation forms a percolated structure already during deposition. It has been shown that the density and size of the voids is directly related to the nominal thickness of the deposited metallic film. Additionally, the formation of voids can be also controlled by the presence of an underlying topographical pattern.

In this work I report the experimental study of the island formation on topographically modified substrates. First, we present the results obtained on a non-ordered surface pattern on glass and silicon dioxide substrates. Moreover, silica substrates with grid patterns prepared by electron beam lithography (EBL, Tescan, MIRA FEG-SEM) were fabricated and employed as substrates for dewetting of the thin (10 and 15 nm) gold layers [49]. The sample characterization were performed mainly by SEM (Carl Zeiss, ULTRA FESEM and Tescan, LYRA FIB-FESEM) and SPM (NT-MDT, NTEGRA Prima).

4.1 Gold island formation on patterned boron silicate glass- and silica substrates

4.1.1 Preparation of glass and silica patterns

Here, the patterning is understood as a specific modification of substrate topography. In the first set of experiments we used a simple approach for preparation of a random topographic

pattern of circular craters surrounded by a rim. The pattern was created by embedding the gold islands into glass and silica substrates [41]. The prepared systems were utilized to obtain basic information on the void formation during the thin gold layer dewetting on substrates patterned by Electron Beam Lithography (EBL).

The recent studies show that the embedding of gold islands into boron silicate glass substrates takes place during annealing above glass transition temperature (557 °C) [50]. The gold islands are the well separated single crystals and their embedding into the glass substrates creates pits with well determined geometry and almost an atomically flat bottom. Their lateral size and height depend mainly on the initial thickness of deposited gold layers [51] (usually 5 – 15 nm thick). A randomly patterned surface is obtained from gold islands (Fig. 4.*1*a) and subsequent gold removal in iodine tincture or aqua regia (Fig. 4.1b). The depth of the prepared craters can be controlled by annealing time. The usual preparation procedure consists of a 10-hour sample annealing at 600 °C which results in a mean crater depth of 13 nm. Annealing was performed in the laboratory oven with air atmosphere.
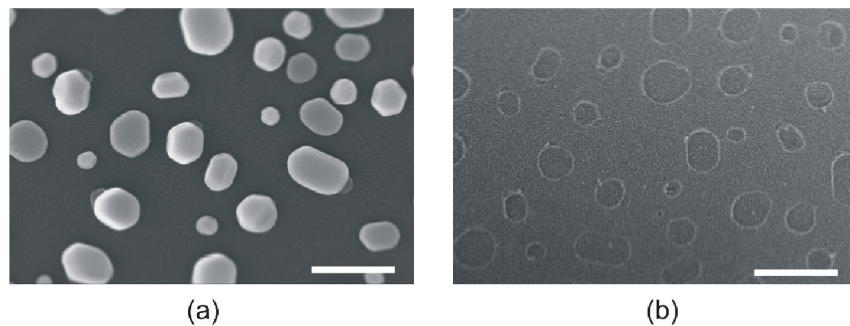

(a)   (b)

Fig. 4.1: SEM images of islands prepared by thermal evaporation of a gold thin film with a nominal thickness of 12 nm on a cover glass slide annealed at 600 °C for 10 hours (a), and subsequently dissolved in aqua regia (b). The scale bar is 300 nm.
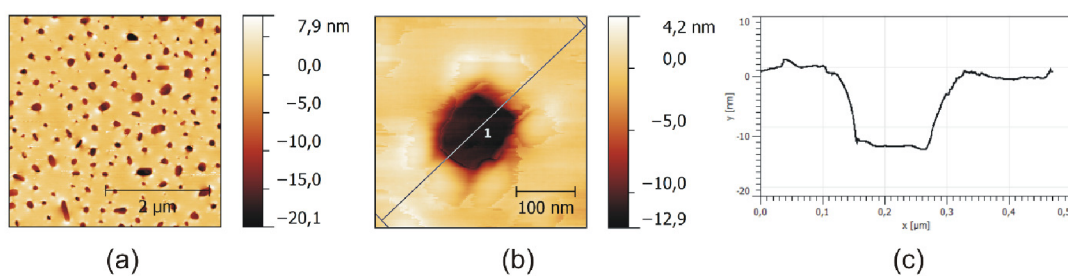

(a)   (b)   (c)

Fig. 4.2: AFM images (a, b) of the pattern prepared by annealing of a 12nm-thick gold layer at 600 °C for 10 hours. The detailed view (b) and depth profile (c) of the crater.

The previous experiments [40, 41, 50] were performed using borosilicate glass substrates. We have shown that similar pattern can be prepared by a high temperature annealing of a gold thin film on thermally grown silica on silicon wafers (SiO_2/Si substrate). The samples were cut from a Si (111) wafer covered with a 40nm- thick silica layer.

The thermally grown silica substrate was chosen according to the following criteria: (1) dewetting of the gold film on the silica substrate is well known and reported, (2) it is a suitable material for the EBL fabrication process, (3) substrates can be reproducibly prepared in house by thermal oxidation of silicon wafers, (4) thermally grown silica substrates are commercially available enabling thus scaling up technology.

The gold islands formed after dewetting of the evaporated film showed embedding into the silica layer after annealing at 900 – 1000 °C. The annealing was performed in the laboratory oven in air atmosphere. After gold dissolution in aqua regia a random pattern of craters is obtained. An example of the patterned silica surface analyzed by SEM and AFM is shown in Fig. 4.3. The sample was prepared by the thermal evaporation of 10 nm of gold on to the thermally grown SiO_2 substrate and annealed for 24 hours at 1000 °C.
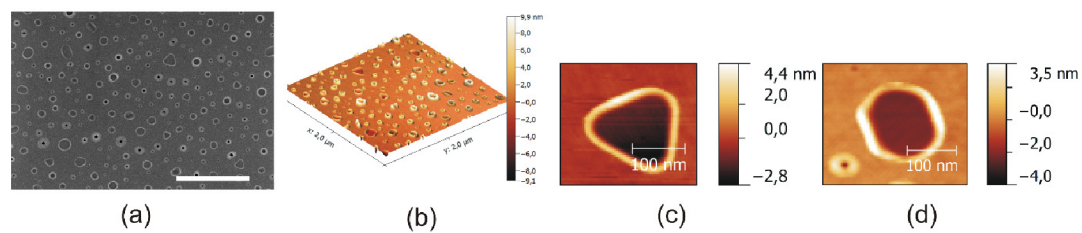

(a) (b) (c) (d)

Fig. 4.3: SEM (a) and 3D AFM images (b) of the patterned silica substrate. High magnification AFM images of formed craters (c, d). The pattern was prepared by the annealing of an Au thin film with a nominal thickness of 10 nm at 1000 °C for 24 hours. The depth of the craters is in a range of 2-15 nm. The scale bar in the SEM image (a) is 1 µm.

4.1.2 Voids formation in gold thin films induced by patterned substrates

The dewetting process is initialized by the formation of voids in evaporated gold thin films [52]. The gold films with a nominal thickness of 3 and 10 nm were evaporated on pre-patterned glass substrates (Fig. 4.4). Density and size of the voids depends on the nominal thickness of the evaporated gold film. The Au island film of a nominal thickness 3 nm does not show any redistribution of islands caused by substrate patterning (Fig. 4.4a). As can be seen in Fig. 4.4b, in case of the 10nm-thin film, the crater perimeter is decorated with long-void segments, while the void network outside this perimeter is random. Controlled voids formation can be achieved when the size of the pattern elements and voids are adjusted.
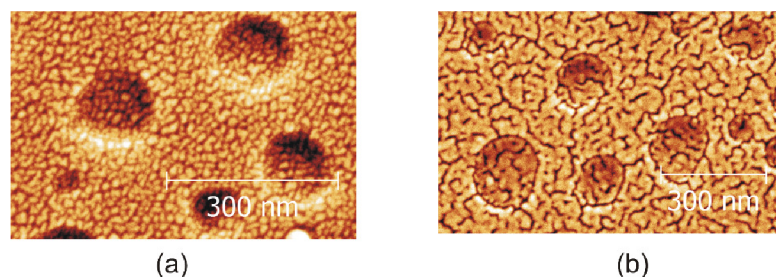

(a) (b)

Fig. 4.4: SEM images of as deposited 3nm- (a) and 10nm- (b) thick gold layer on the patterned glass substrate.

Further investigation of the void formation was then carried out on a system where the pattern and voids have comparable sizes. It can be achieved by using Au thin films of the same thickness (10 nm)   as for pattern preparation and gold deposition. The formation of the voids on the crater perimeter can be observed by SEM and AFM as demonstrated in Fig. 4.5. The SEM image (Fig. 4.5a) shows the void structure and void opening along the crater perimeter. The AFM imaging (Fig. 4.5b, c) is a more topography sensitive method limited by the tip radius of typical size 10 – 20 nm. The AFM images show that the percolated gold layer is composed of separated, randomly distributed gold clusters covering the surface. The individual voids are not clearly visible. The void formation observed by SEM shows that an interaction between the gold clusters and substrate pattern has to be considered. It can be demonstrated on the voids formed around the craters in pattern visible by SEM. AFM shows that the clusters are arranged into a chain forming a regular wall. The voids are then created in the space between the wall and gold clusters at the bottom of the crater (Fig. 4.5).
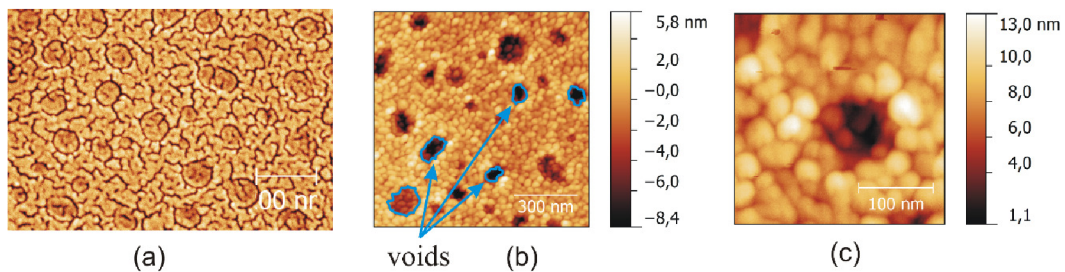

Fig. 4.5: SEM (a) and (b) AFM image of the 10 nm-thick gold layer evaporated on the patterned glass. (c) Detailed AFM image of the crater with the deposited gold. The pattern was prepared by annealing of a 10 nm-Au thin film at 600 °C for 10 hours.

4.1.3 Low temperature annealing of gold on patterned substrates

The solid-state dewetting process is driven by the capillary forces and occurs at elevated temperatures. The annealing temperature required for the initial stage of dewetting was determined as a $0.2T_m$ [25], where T_m is the melting temperature of the material. The structural changes of the gold layer were then studied at 200 °C. As can be seen in Fig. 4.6, the 15 nm-gold thin film deposited on a patterned glass substrate and annealed for 2 hours at 200 °C possesses voids along the crater edges.
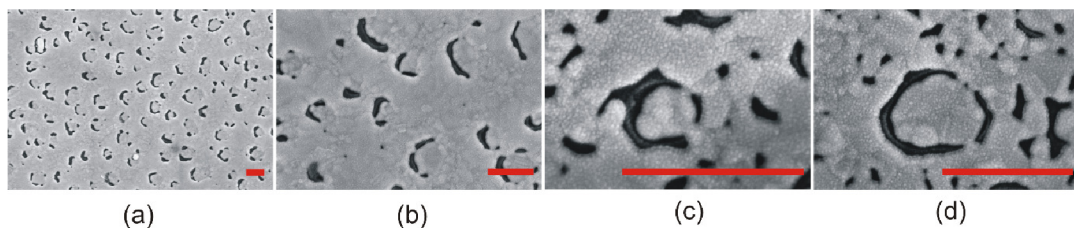

Fig. 4.6: SEM images of the deposited 15nm- gold layer annealed at 200 °C for 2 hours on the pre-patterned glass substrate taken at different magnification. The scale bars are 300 nm.

48

The initial morphological changes are driven by a decrease of the chemical potential in the area with a high negative local curvature (see Eq. 4.2) shown in Fig. 4.7a. This mainly occurs at the crater perimeter where the initial voids appear after deposition. The annealing initiates a decrease of the local curvature which causes the edge retraction and void enlargement Fig. 4.7b).
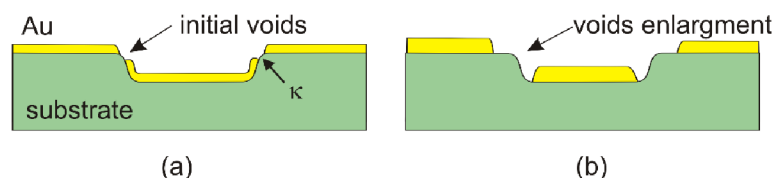

Fig. 4.7 Schematic side view on the pre-patterned substrate with the deposited gold film with the initial voids opening in the area with the negative curvature κ (a) and further island formation after annealing (b).

The low temperature annealing shows interesting results. The formation and enlargement of voids predetermine the further evolution of the annealed gold. The ability to control the void formation open the possibilities to fabricate regular arrays of precisely positioned gold islands. Another perspective is directly connected to annealing at low temperature, which allows us also to control the shape of detached gold areas.

4.1.4 Gold annealing and island formation on patterned substrates

The dewetting process at 500 °C causes formation of separated crystalline islands. The precise positioning of these islands into craters might be generally desirable and was the main task of this study. The random patterns with the wide range of crater radius 60 ± 40 nm were mainly utilized in this task. As discussed previously, the nominal thickness of the evaporated gold thin film significantly influences the size of gold islands after dewetting. The films of different nominal thicknesses (5, 10 and 15 nm) were deposited and annealed (500 °C) on the patterned glass substrates shown in Fig. 4.8. Each nominal thickness result in the different size of island size distribution. The annealing of a 5 nm-thick gold layer results in formation of small, roughly circular islands with the average radius 10 nm (Fig. 4.8a). The longitudinal size of the craters may exceed that of islands and even more islands can be formed at the crater bottom (Fig. 4.8a). On the other hand, in the case of the 15 nm-thick layer the large gold islands span over several craters (Fig. 4.8c) as the size of the islands was 150 nm. In both cases the task of this study was not achieved. The best results were obtained using the 10 nm-thick gold layer (Fig. 4.8b). The size of the islands (50 ± 40 nm) was roughly comparable to that one of the craters. It can be seen that in most cases the craters are occupied by single gold islands. However, the wide size distribution of the used random crater pattern makes further improvements impossible.

It should be also pointed out, that at 500 °C the dewetting proceeds within the first minutes of annealing. Longer annealing times do not significantly influence the island shape and position.
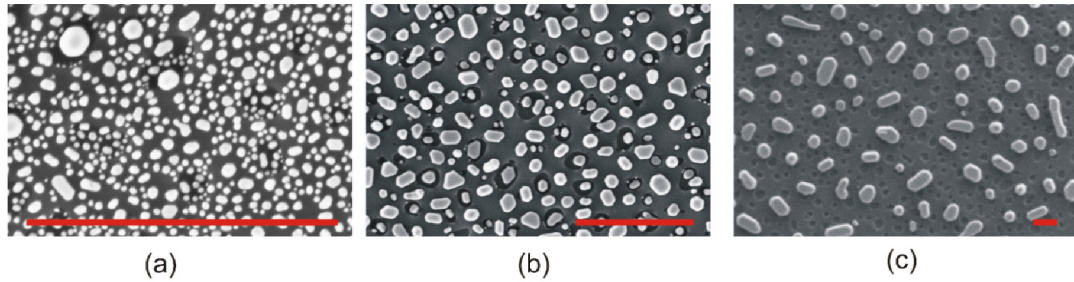
Fig. 4.8: SEM images of the gold thin film with the nominal thickness 5 nm (a), 10 nm (b) and 15 (c) on the patterned surface annealed at 500 °C. The scale bars are 500 nm.

4.1.5 Summary of the experiments

The solid-state dewetting of gold films is influenced by substrate topography if the voids formed in this film follow a pattern motive, i.e. when the voids are preferentially formed at the crater perimeter. In the case that the size of craters and voids is, the dewetting and island formation follow the pattern.

4.2 Fabrication of ordered arrays of gold islands

The previous results have shown that the solid state dewetting of gold films is influenced by substrate topography. The preferential opening of the voids was observed on the edges of the pattern elements. In this section we will show that this can be used for directing of the dewetting process, i.e. for the precise positioning and size control of gold islands. The general strategy for achievement of this control is based on the replacement of a random pattern by regular one. Here, electron beam lithography (EBL) was used for fabrication of a pattern with regularly arranged topographical edges which define circumscribed areas. The preferential dewetting of an evaporated gold film proceeds along a regular pattern of topographic edges and, consequently, results in producing individual islands. Their size is controlled by volume of gold trapped inside circumscribed areas. The islands are positioned in the vicinity of the center of these areas.

The ordered arrays of gold islands reported in this work have been achieved by annealing of a 15 nm- gold thin film evaporated on a silica substrate with a pre-fabricated pattern. The employed pattern presents a regular grid of the square-shaped elementary units with the repeating size A ranging from 100 to 500 nm (Table 4.1). The complete range of distinct patterns was fabricated on each sample to study an influence of the pattern repeating size on the final film morphology while keeping the gold layer thickness and other parameters the same.

4.2.1 Design of the pattern

In order to design the pattern suitable for fabrication of ordered arrays one has to consider several aspects:

- **The nominal thickness of the evaporated gold thin film** strongly influences the island structure. The mean size of gold islands formed after dewetting depends on the gold nominal thickness and void density. It has been already shown that the mean void length observed on the patterned substrate has to be of the similar size to the pattern units in order to obtain the desired results. Hence, the pattern size has to be chosen according to the selected gold nominal thickness. In this work the nominal thicknesses of the gold thin film of 10 and 15 nm were used.
- **The shape and size of the elementary units** define the area from which the material is collected for a single island during dewetting. To avoid formation of non-ordered islands and errors in the periodical structure, the gap between adjoining units should be as small as possible.
- **Sharpness (radius of curvature) of the topographical edges** is related to the local chemical potential which is strongly affecting the void formation in the gold film. The depth profile of fabricated edges should be as sharp as possible to reach the maximum in the local curvature.
- The depth of the pattern is given mainly by the application requirements and do not directly affect the dewetting process. In this work the relatively shallow pattern (22 nm) was used.
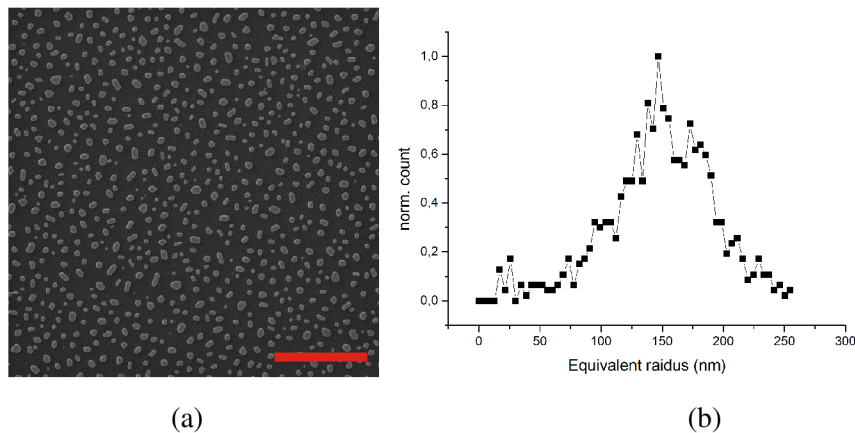

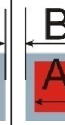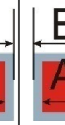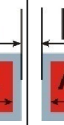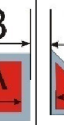(a)   (b)

Fig. 4.9: SEM image of the 15 nm-thick gold layer after one-hour annealing at 600 °C (a) and the corresponding size (equivalent radius) distribution function (b). The scale bar is 5 µm.

The size of the islands formed on the flat substrate (i.e. outside the craters) obtained in the previous section was used to estimate the initial parameters for our study: thickness of the gold thin film and appropriate pattern design. The SEM image of gold islands formed after the dewetting of 15 nm-thick gold layer on a non-patterned substrate after annealing at 600 °C for 1 hour is shown in Fig. 4.9a. Using the Gwyddion software [53] the particle size distribution (PSD) (Fig. 4.9b) and surface coverage were determined. Fitting the obtained island size distribution by the Gauss function gives the mean island radius 150 nm with a FWHM of 80 nm. The surface coverage α was 16 %. One can calculate the collection area

S_c of a single island as $S_c = \pi r_m^2 / \alpha$, where r_m is the mean equivalent radius. On the surface without patterning S_c is approximately 0.5 µm². It has been reported that patterned substrates cause a decrease in the islands size [45]. Therefore, to prepare a structure where each cell contains a single island collection area, S_c should be smaller than that for the non-patterned surface. The pattern collection area S_{pc} is determined by the parameter B shown in Tab. 4.1. The depression area (i.e. the area lowered by etching) is smaller due to the gap between two squares and can be defined by the groove size A, where A was 100, 200, 300, 400 and 500 nm. The designed elementary units dimensions and parameters of islands formed on an unpatterned substrate are given in Tab. 4.1. The expected size r_m of the islands formed on the proposed grids can be calculated as $r_m = \sqrt{S_c \alpha / \pi}$.

Pattern Unit Shape	B / A	B / A	B / A	B / A	B / A	B / A	No pattern
Groove area size A [nm]	100	200	300	400	500	600	
Elementary unit size B [nm]	200	300	400	500	600	700	670*
Pattern collection area $S_{pc} = B^2$ [10³nm²]	40	90	160	250	360	245	
Single island collection area S_c [10³nm²]	-	-	-	-	-	-	448
Estimated equivalent radius r_m [nm]	45	56	79	102	124	104	152

Tab. 4.1: Parameters of elementary units. The equivalent radius was measured only on the surface with no patterning. *at flat surface without patterning calculated as $B = \sqrt{S_c}$.

The triangular shape of the elementary unit was also implemented assuming that the crystallization at low temperatures (200 – 300 °C) will allow the shape of gold islands to follow the shape of the pattern. The dewetting process at higher temperatures (> 300 °C) leads to the formation of crystalline islands the shape of which is defined by faceting. In such a case the relevant parameter is only the size of the collection area S_c.

A schematic view of the proposed elementary units and SEM- and AFM images of fabricated grids are displayed in Fig. 4.10. The difference in the designed and obtained shapes is given by the inaccuracies during the lithographic process used for the pattern fabrication and will be discussed in detail later.
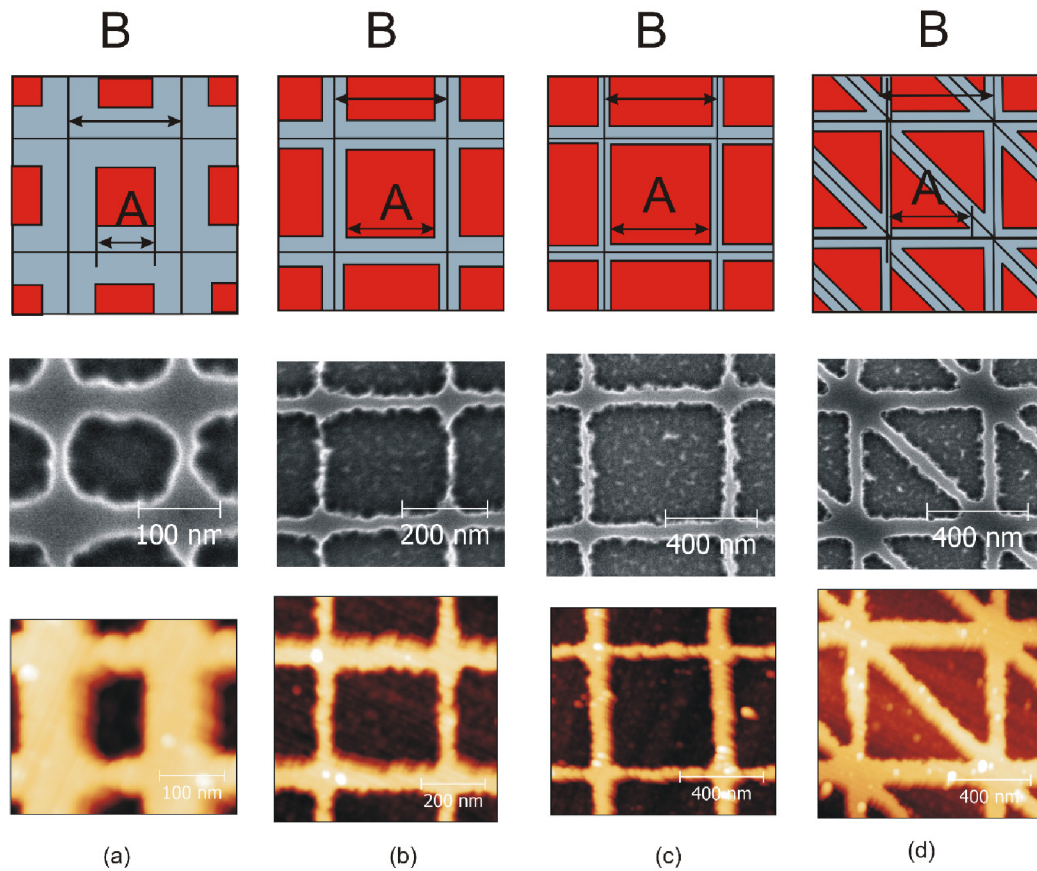
Fig. 4.10: Schematic view of different elementary units (upper row) and corresponding fabricated patterns imaged by SEM (middle row) and AFM (bottom row). The size *A* of the square shaped units is 100 nm (a), 300 nm (b), and 500 nm (c). The characteristic size of the right-triangle shape *A* is 600 nm (d).

4.2.2 Fabrication of grid patterns by e-beam lithography

Electron beam lithography (EBL) [19] is one of the fabrication techniques suitable for preparation of nanostructures. The complete procedure consists of several steps which are depicted in Fig. 4.11. The first step (Fig. 4.11a) is the removal of all organic impurities from the sample surface by the piranha solution ($H_2SO_4:H_2O_2$, 3:1) followed by ethanol cleaning and drying by nitrogen flow. The second step is the deposition of a PMMA (Poly (methyl methacrylate) thin film by spin coating (Fig. 4.11b). The positive PMMA A2 950K resist was used; two step spin coating of 80 µl of solution was carried out: 5 seconds at 500 rpm and 55 seconds at 6000 rpm. The sample with PMMA was baked at 180 °C for 1.5 minute. The thickness of the PMMA film was in the range of 80 – 100 nm. The electron exposure proceeded at three different electron doses (150, 200 and 250 $\mu C/cm^2$) with the beam energy 30 keV (Fig. 4.11c). The exposed PMMA resist was developed in the 3:1 (IPA: MIBK) solution for 1.5 minutes and in IPA stopper for 30 seconds (Fig. 4.11d). The bare silica surface (e-beam exposed area) was etched in the NH_4F (40%):HF(40%) (5:1) solution for 10 seconds (Fig. 4.11e), typical etching rate of the solvent for SiO_2 was 2 nm/second.

The mean depth of the etched area (after removal of the resist in acetone) measured by AFM was 22 nm (Fig. 4.13).
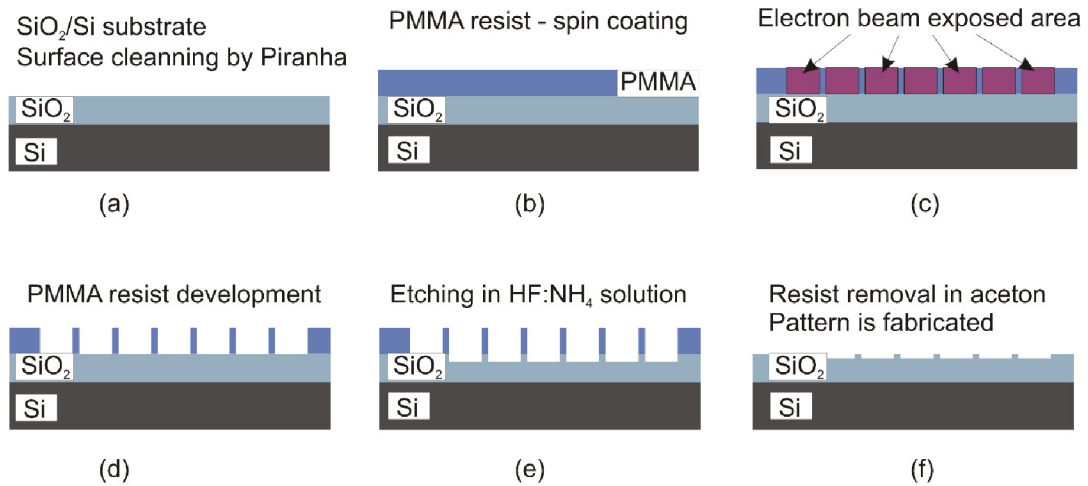

Fig. 4.11: Schematic view of the pattern fabrication on SiO₂/Si substrate by EBL.

The set of grid arrays fabricated on the sample surface is shown in Fig. 4.12. The gray squares represent an exposed area. The square size A varies from 100 nm to 500 nm with a constant gap between each unit of 100 nm. In addition, the right-triangle shape pattern with a unit side size of 600 nm and gap distance 100 nm was prepared.
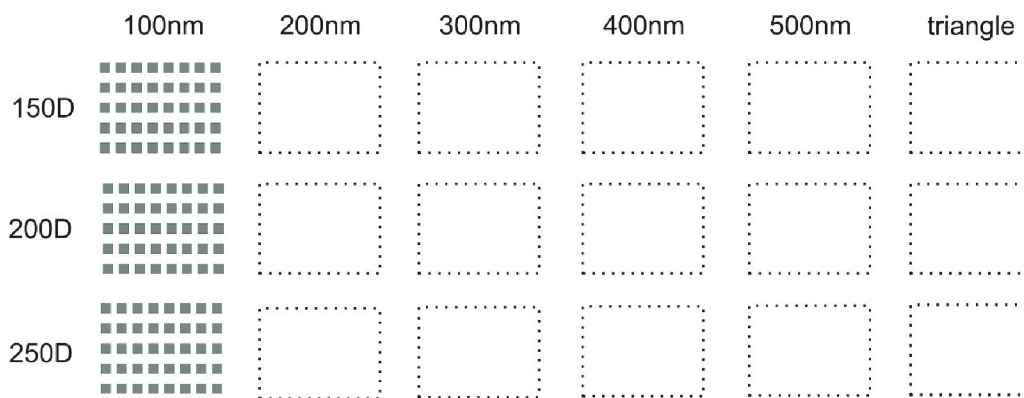

Fig. 4.12: EBL grid pattern matrices designed for electron beam lithography consisted of elementary square-like units of the size 100 – 500 nm and an elementary triangle unit. Three different exposure doses 150 – 250 $\mu C/cm^2$ were used.

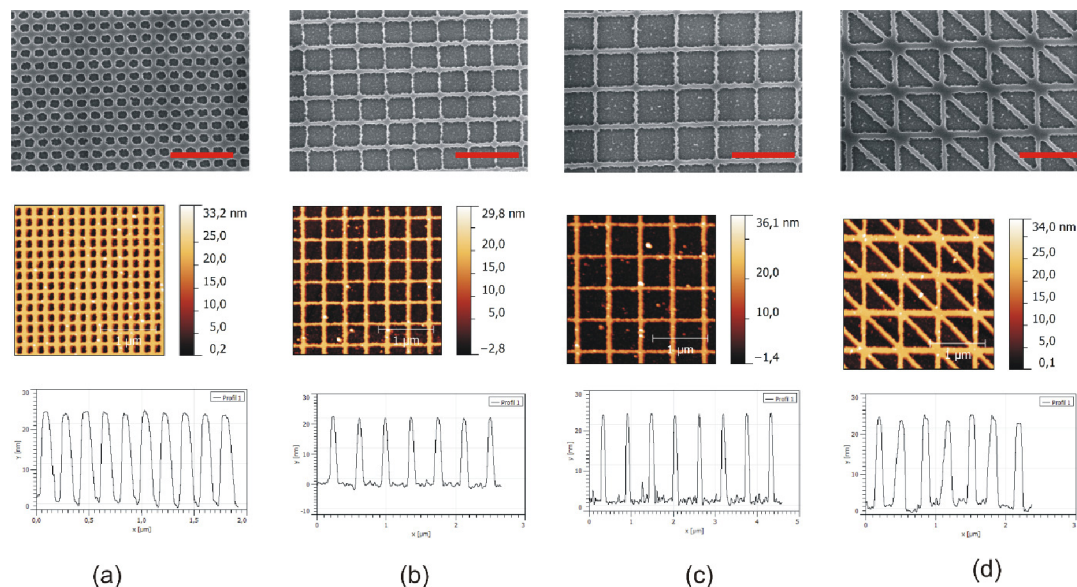The fabricated grids with the different unit size are shown in Fig. 4.13.

Fig. 4.13: SEM images (upper raw) and AFM images (middle raw) of the grid patterns made into a SiO2 layer using EBL. The square motive with the different cell sizes 100 – 500 nm (a - e) and a triangle one with the edge 600 nm (f). The bottom raw shows the topography profiles of different grids obtained from AFM images. The scale bar is 1 µm.

4.2.3 Void formation induced by the silica pattern

As discussed previously, the nominal thickness of the gold thin film strongly influences the formation of voids. The films of 10 and 15 nm nominal thicknesses were used to study the difference in the void formation.

As evaporated, the Au films were studied using HRSEM. While secondary electrons (SE) are better for detection of surface topography, backscattered electrons (BSE) are more sensitive to the material contrast, allowing imaging the voids. The contrast between the silica and the gold film is noticeable. Observing the material contrast for seeing voids and surface topography was done by simultaneous utilization of SE and BSE (Fig. 4.14).

The density of voids is higher for the 15 nm-thick gold layer compared to the 10 nm-thick one as can be seen from the BSE images in Fig. 4.14 (a, c) for the pattern with the square size $A = 300$ nm. In both cases the voids are preferentially formed at the pattern edges and so the motif can be recognized. For the 10 nm film the voids are wide enough to be clearly seen also using the SE detector (Fig. 4.13 d). However, the voids in this film are also formed inside the square units as can be seen in Fig. 4.14 c, d. Hence, based on the designed pattern the void density in the gold film with a nominal thickness of 15 nm is more suitable for fabrication of the ordered arrays of gold islands.
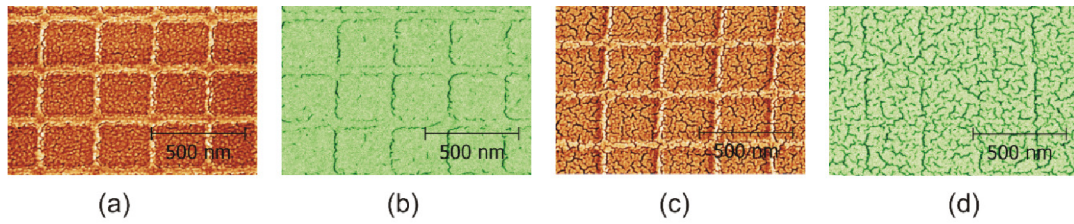
Fig. 4.14: SEM images of 15 nm (a, b)- and 10 nm (c, d)- Au thin film with the pattern size A = 300 nm imaged by BSE (a, c) and SE (b, d) detectors.

Generally, it can be concluded that the pattern design can be chosen according to the applied nominal thickness of the gold thin film and known density of voids.

4.2.4 Low temperature annealing

The evolution of the gold film morphology is strongly influenced by the annealing conditions (temperature and time). Transformation of the gold film into a regular array of fully separated gold islands was experimentally studied in several experimental series. Annealing temperatures were sequentially raised to 200 °C, 220 °C, 250 °C, 270 °C and 300 °C, and the transformation was monitored by SEM.

Annealing at relatively low temperature 200 °C induces recrystallization and growth of gold grains followed by the voids opening [25]. All these processes occur after a short annealing time. Both effects are strongly influenced by the local curvature of the substrate and gold grains. The study of gold film evolution on the patterned surface was carried out with respect to temperature and duration of annealing, and size of pattern units.

The initial morphological changes at 200 °C occur in the areas with the high local substrate curvature which induces the void formation occurring already during evaporation, as shown in the study of randomly patterned substrates. After a decrease of the local curvature by voids enlargement the island separation slow down [25]. Such a process saturation was experimentally confirmed by annealing at 200 °C for 1, 9 and 20 hours as shown in Fig. 4.15. After the initial voids enlargement, additional changes include only recrystallization resulting in formation of a more uniform Au film in separated areas.
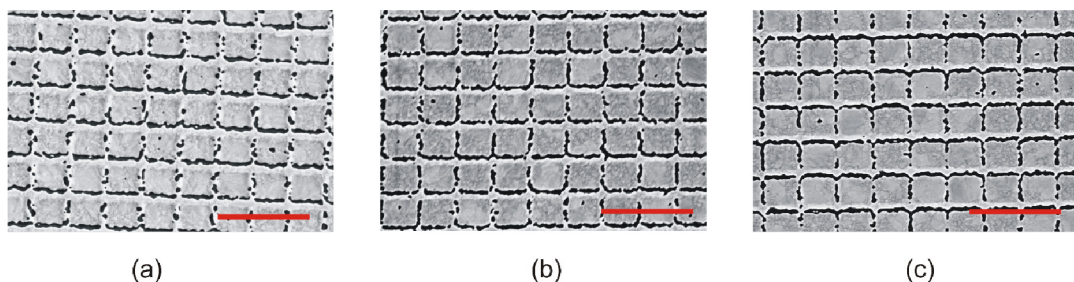

Fig. 4.15: SEM images of the 15nm-thick gold layer deposited on to the SiO_2 grid pattern with A = 300 nm and annealed at 200 °C for 1 hour (a), 9 hours (b) and 20 hours (c). The scale bar is 1 μm.

56

The SEM images of the annealed film evaporated on the SiO$_2$ patterns with different unit sizes show very similar morphology (Fig. 4.16). On each grid the visible voids follow the pattern edges of the underlying substrate. The film morphology development saturation occurs for all the patterns. It can be concluded that at low annealing temperature the pattern size does not affect the film evolution.
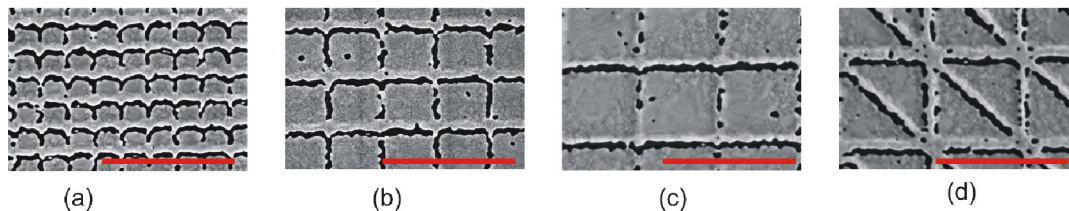

(a)　　　　　　　(b)　　　　　　　(c)　　　　　　　(d)

Fig. 4.16: SEM images of the 15 nm-gold layer deposited on to the SiO$_2$ pattern grids and annealed at 200 °C. The square-like patterns with a unit size of 100 nm (a), 300 nm (b) and 500 nm (c), and the triangular shape pattern (d). The scale bar is 1 μm.

Surprisingly, the void opening is not identical in all directions. This is evident in Fig. 4.16a, b where the bottom parts of each square are not opened. This effect is most probably caused by a slight tilt of the sample during gold deposition. The tilted deposition causes a nonuniform distribution of gold, which is pronounced mainly on the grooves. To suppress it, a special attention was paid during the mounting and aligning of the samples before the gold evaporation. However, we were not able to completely eliminate film inhomogeneity.

An example of the transformation of the Au thin film into various patterns during annealing at 250 °C and 270 °C is shown in Fig. 4.17. Even though the voids have become enlarged the layer still shows a percolated structure.
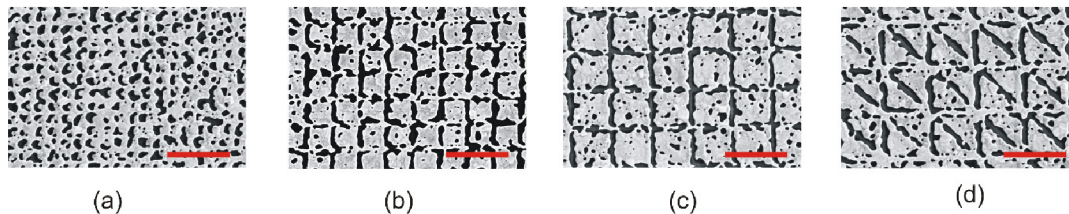

(a)　　　　　　　(b)　　　　　　　(c)　　　　　　　(d)

Fig. 4.17: SEM images of the 15 nm-gold thin film deposited on the square-like patterns with a unit size of 100 nm (a), 300 nm (b), 500 nm (c), and triangles (d) annealed at 250 °C for 3 hours and, subsequently, at 270 °C for 3 hours). The scale bar is 1 μm.

The increase of annealing temperature to 300 °C resulted in a qualitative change of the film morphology (Fig. 4.18). After the first hour only an opening of the voids (Fig. 4.18a) was observed, similarly to the films annealed at lower temperatures (Fig. 4.15, Fig. 4.16). The void opening was not terminated after the initial stage and after 13 hours of annealing the Au film was completely dewetted, forming separated islands correlated with the topographic pattern of the substrate (Fig. 4.18b).

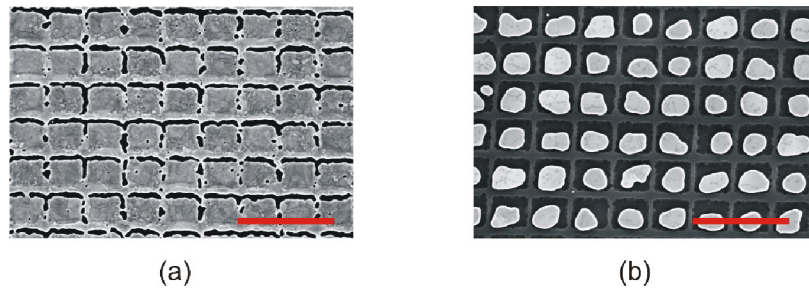(a)   (b)

Fig. 4.18: SEM images of the 15 nm-gold thin film deposited on to the square-like patterns with a unit size of 300 nm annealed at 300 °C for 1 hour (a) and 13 hours (b). The scale bars are 1 μm.

The dewetting process and progress of the transformation can be characterized by the surface coverage which decreases with increasing annealing temperature. The surface coverage was determined from SEM images using the Gwyddion software. The typical annealing time leading to the formation of a stable structure ranges from a few minutes to several hours and rapidly decreases with increasing annealing temperature. The surface coverage comparison was done after a 3-hour annealing. The relation between annealing temperature and surface coverage is shown in Fig. 4.19. This relation can be divided into two parts representing different processes. At annealing temperatures below 300 °C (critical temperature) the void enlargement is a dominant effect. The saturation of film transformation takes place and separated islands are not formed. Above the critical temperature the dewetting fully takes place and islands are formed. Hence, determination of the critical temperature is an important parameter for the dewetting process.
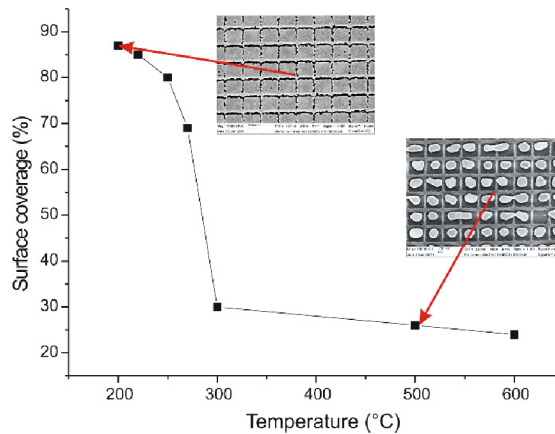

Fig. 4.19: Dependence of the surface coverage on the annealing temperature. The data were obtained from the analysis of SEM images of the annealed 15 nm gold layer on the patterned substrate.

A complete separation of gold islands driven by the shape of the pattern could be a very promising method for the preparation of gold islands of various shapes.

58

4.2.5 Optimization of the annealing procedure

Thermal annealing of gold thin films on patterned surfaces above the critical temperature (300 °C) results in the formation of an array of separated gold islands. However, irregularities and imperfections in a periodical structure, e.g vacant sites and merged islands, can be found. An improved regularity was achieved by an optimization of the annealing process by a two-step annealing procedure. The purpose of the two-step annealing is to extend the annealing period below the critical temperature and, consequently, to enlarge the void size along the pattern edges which leads to well-defined collection areas. An additional annealing above the critical temperature improves the separation of the islands. Comparison of gold arrays prepared by the one- and two-step annealing process is shown in Fig. 4.20.
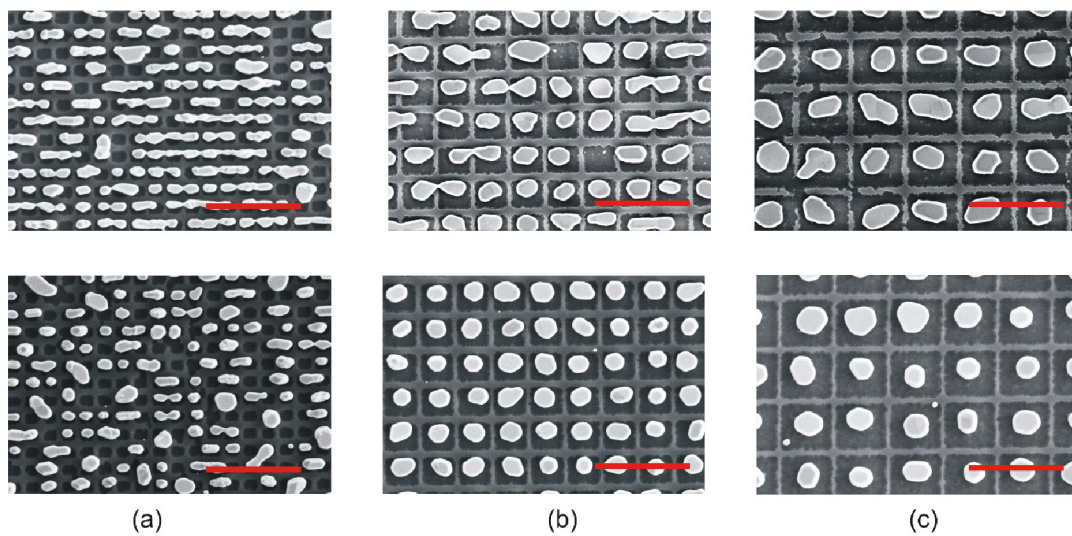

(a)   (b)   (c)
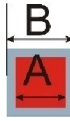
Fig. 4.20: SEM images of the 15 nm gold layer deposited on the square-like grid pattern with a unit size 100 nm (a), 300 nm (b) and 500 nm (c) annealed in the one step process at 500 °C for 1 hour (upper row) and in the two-step process at 200 °C for 1 hour and at 600 °C for 1 hour (bottom row). The scale bars are 1 µm.

The optimized procedure consists of annealing at 200 °C for 1 hour followed by 1 hour annealing at 600 °C. Ordered arrays of gold islands were observed for the pattern with A = 200, 300, 400 and 500 nm as shown in Fig. 4.21. The size of the formed islands was determined by PSD (Particle Size Distribution) and fitting by the Gauss function. The obtained parameters are shown in Tab. 4.2. The size of the islands on the grids is reduced compared to the flat substrate. The FWHM of island size distribution is significantly reduced on the grids (30 nm) with respect to the islands on the flat surface (80 nm).

Pattern Unit Shape	B / A	B / A	B / A	B / A	B / A	No pattern
Depression size A [nm]	100	200	300	400	500	
Mean equivalent radius [nm]	59	88	111	133	143	152
FWHM [nm]	10	17	24	30	34	80
Height [nm]	NA	63	70	78	92	NA

Tab. 4.2: Parameters of the size distribution function of gold islands on different grids. NA – not available.
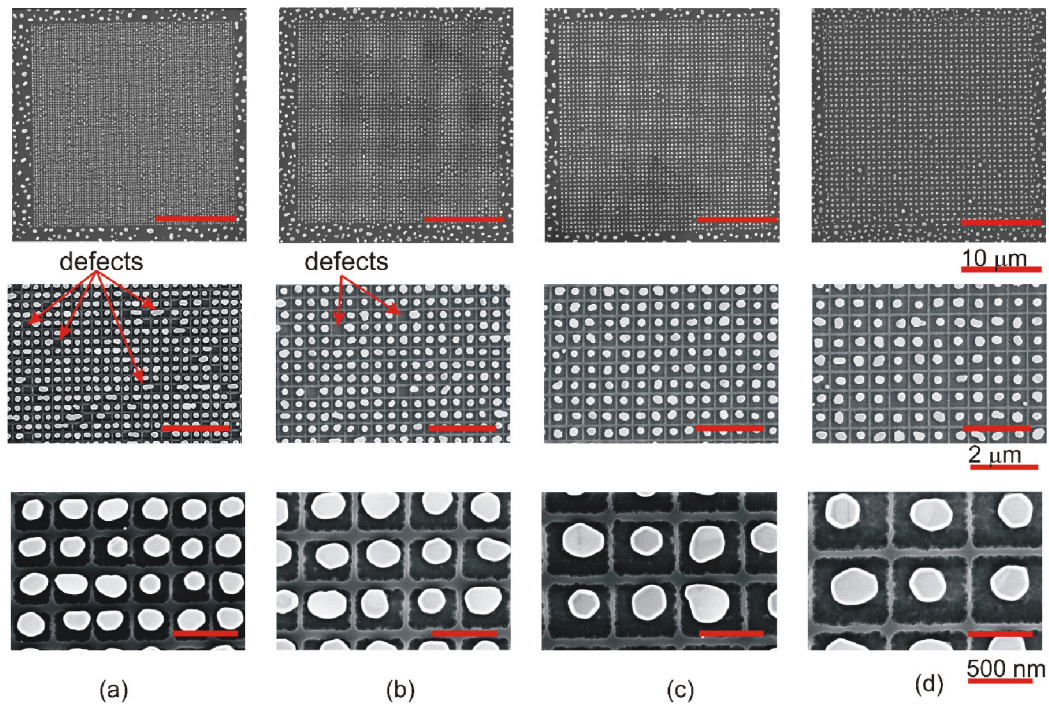
Fig. 4.21: SEM images of the gold island arrays with a grid size 200 nm (a), 300 nm (b), 400 nm (c) and 500 nm (d) prepared by dewetting of a 15 nm thick gold layer annealed in two steps: at 200 °C for 1 hour and at 600 °C for 1 hour.

The presented results have shown a few defects such as vacancies and large islands originated from doubling of the collection areas. The latter type of defect occupies the adjacent cells forming a vacancy and large island pair as can be seen in SEM images (Fig. 4.21). Irregularities are most probably caused by inaccuracies in grid patterns and asymmetric void opening resulting from a previously discussed shadowing effect during gold evaporation. The formation of separated gold islands has been achieved on the maximum area 30x30 μm^2, which is limited by the size of grid patterns. The size of these

patterns can be enlarged or adjusted according to the application requirements. It has been also demonstrated that it is possible to fabricate different patterns on one sample resulting in formation of islands of different size and spacing. The island size distribution for different grids is shown in Fig. 4.22b.

(a)   (b)

Fig. 4.22: Size distribution of gold islands prepared by annealing of a 15 nm-thick gold layer on different grids with $A = 100$ nm (a), 200 nm, 300 nm, 400 nm and 500 nm (b) after a two steps annealing process at 200 °C for 1 hour and 600 °C for 6 hours.
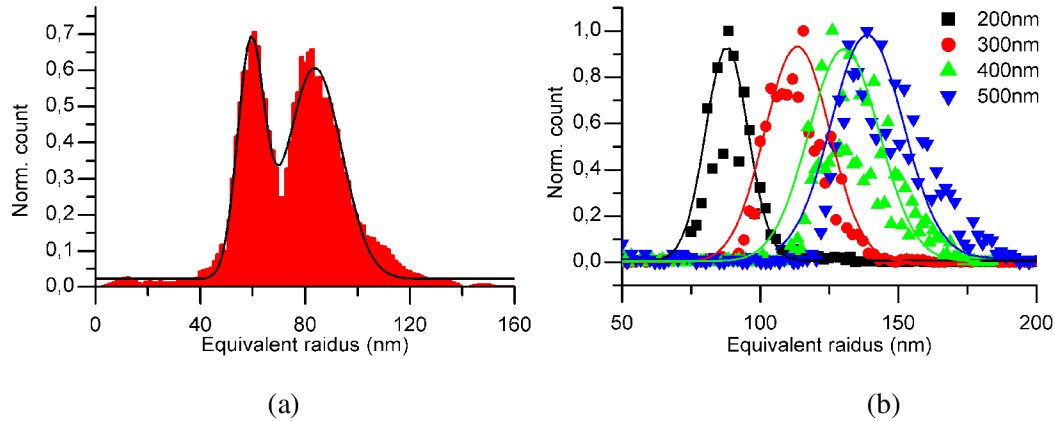
The array with $A = 100$ nm shows significant defects caused mainly by the merging of two adjacent islands and formation of a vacant cell in the pattern (Fig. 4.20a). The merged islands can be recognized in the size distribution function with two peaks shown in Fig. 4.22a. The two Gauss functions were used for fitting, and as a result equivalent radiuses of 59 nm and 83 nm were determined. The larger islands with a 83 nm equivalent radius are formed by merging gold from two adjacent square units, which is in good agreement with the equivalent radius of islands formed from the double collection area with $A = 200$ nm (Tab. 4.2).

4.3 Conclusion

It has been shown that topographical modification of substrates can be used for fabrication of ordered arrays of gold islands. Dewetting of the just-percolated Au thin film follows the topography of a pre-designed pattern. Preferential opening of voids induced by morphology of a patterned substrate allows fabrication of an ordered array of gold islands. The film dewetting scenario depends on the nominal thickness of the gold layer, annealing temperature and parameters of the pattern. It has been found that for gold films with a nominal thickness of 15 nm an ordered array gold islands can be prepared using a square pattern with the cell unit in the range 200 – 500 nm and a two-step annealing process (1 hour at 200 °C and 1 hour at 600 °C). The representative 3D images of ordered island films are shown in Fig. 4.23. The size of the gold islands in the range 59 – 149 nm can be controlled by the size of the square elementary unit (collection area).
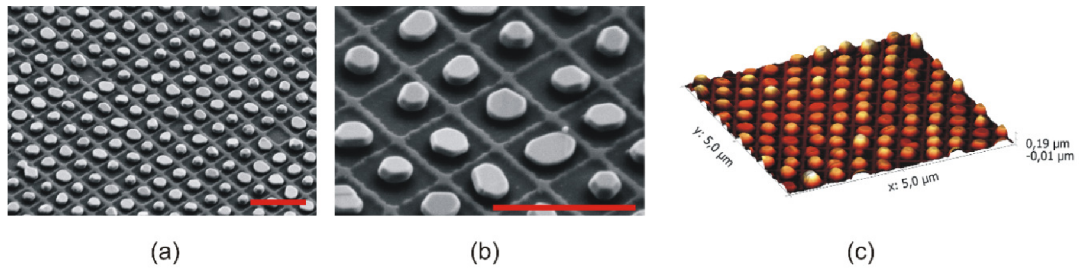
Fig. 4.23: Tilted (70°) SEM (a, b) and AFM (c) image of a gold island array formed by annealing of a 15 nm-thick gold layer on the grid pattern with the size $A = 400$ nm. The scale bar is 1 µm.

The proposed fabrication procedure is based on well-developed and easily scalable techniques (e-beam lithography, thermal evaporation, annealing) opening possibility of their commercial applications. The further studies should include the fabrication of more sophisticated patterns and application of topographically controlled dewetting of materials different from gold. This will extend the areas of possible practical applications.

5. High temperature annealing of gold thin films

Preparation of semiconductor- or oxide supported metal particles is of a great importance due to their applications in catalysis [54, 55], nanowire growth [56], and plasmonic sensors [51, 57]. Embedding metallic nanoparticles into an oxide substrate was reported for several systems such as Pt/SiO$_2$ [58, 59], Au/SiO$_2$ [60-62], Au/glass [52], Au/TiO$_2$ [63] and others. Previous investigations have shown that the embedding process can be induced by ion irradiation or annealing while the threshold temperature for the inset of this process depends strongly on a specific support material.

A full understanding of the embedding process has not been achieved yet. In this work we report on the gold embedding into a silica thin film thermally grown on (111) silicon wafers (denotes below as the "silica substrates") at the high temperature (1000 °C) close to the melting point of Au (1064 °C). The aim of this work was related to potential applications in plasmonics.

5.1 Description of experimental results

Gold thin films with a thickness of 10 nm were prepared by thermal evaporation of gold on silica substrates. The (111) silicon wafers pre-treated with the piranha solution were oxidized at 1000 °C under ambient atmosphere. The thermal growth was terminated at the silica thickness ≈ 500 nm. The initial (as deposited) gold layers form percolated polycrystalline structures shown in Fig. 5.1a. Their annealing at 1000 °C under the oxidation atmosphere leads to a quick (minutes) layer dewetting and formation of separated gold islands. HR SEM images of the films annealed for a prolonged time reveal complex changes in the film morphology. A representative SEM image of the film after annealing for 6 hours presented in Fig. 5.1b shows gold islands and partly filled or empty pits. The morphology of modified silica surface after the etching of Au in aqua regia is shown in Fig. 5.1c. Comparison of images in Fig. 5.1b, c indicates that large faceted Au islands are also embedded in the silica.

(a)   (b)   (c)
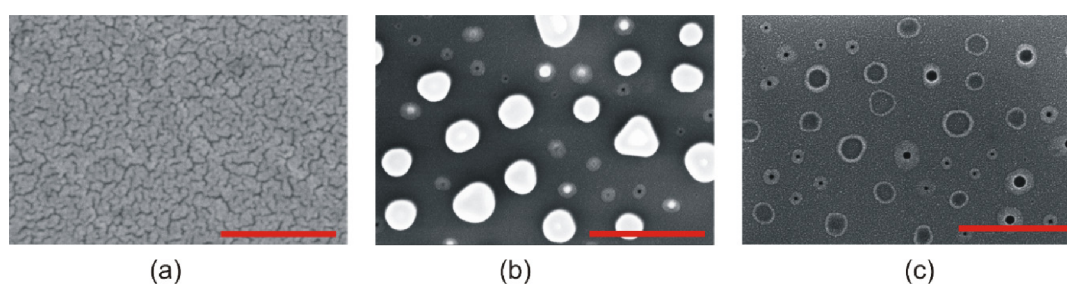
Fig. 5.1: SEM image of as a deposited 10 nm-thick gold layer on silica (a), the sample after annealing at 1000 °C for 6 hours (b) and after gold dissolution in aqua regia (c). The scale bar is 500 nm.

After prolonged annealing three characteristic morphological structures can be clearly distinguished: a) faceted single crystal islands with the diameter > 100 nm (Fig. 5.1b), b) rounded gold islands with the diameter < 60 nm enclosed by wide craters with the

surrounding silica rim (active craters) and having the different stage of embedding (see Fig. 5.2 b), and c) empty craters without any gold islands inside (Fig. 5.2c). Some apparently empty crates clearly showed the presence of small Au nanoparticles (NP) after image contrast variation in Fig. 5.1b. Some craters contained deeply embedded small Au NPs which could be seen from images obtained by a SE detector (not shown). The depth of the craters was in the range of 1 – 15 nm and varied with their size: the small craters were deeper and the large ones shallower.

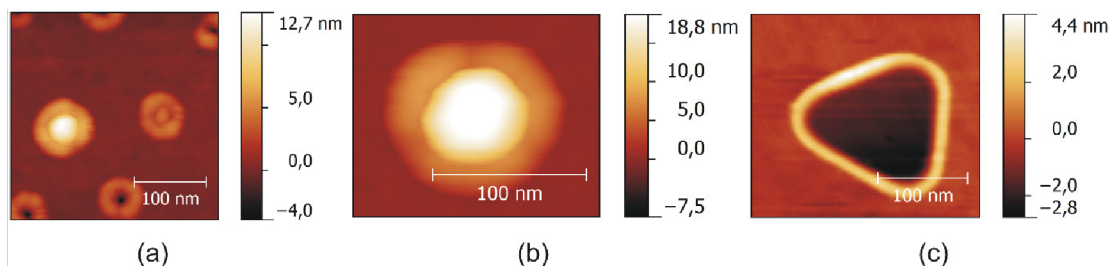(a)   (b)   (c)

Fig. 5.2: AFM images of the modified silica surface with empty- and partially immersed in craters (a), a crater with the surrounding rim and remaining gold island inside (b), an empty crater with the surrounding rim (c).

5.2 Gold island transformation

Morphological changes in the gold layers are driven by minimization of the total energy of the system. Here, two main processes are involved: dewetting and Ostwald ripening. Separated gold islands are relatively quickly formed by dewetting in the timescale of minutes during sample heating. An additional mass transfer between adjoining islands due to Ostwald ripening proceeds at a much longer timescale. A continuous macroscopic flux of gold atoms from the smaller to larger islands is driven by the curvature-dependent difference in the chemical potential (see Eq. 3.2), [64]. As a result, due to the Ostwald ripening the smaller islands slowly disappear while the Au is transferred to larger islands. This process occurs during the whole annealing treatment.

As shown in Fig. 5.3a, after a 5 minutes annealing no empty craters were detected. After 3 hours of annealing (Fig. 5.3b) the concentration of the islands decreases and several craters can be identified. The annealing time prolonged to 24 hours (Fig. 5.3c) leads to a further decrease of the island concentration and an increase of the density and size of craters. An Ostwald ripening-induced decrease of small islands is schematically shown in Fig. 5.3, where empty craters remain after a complete dissolution of small islands.
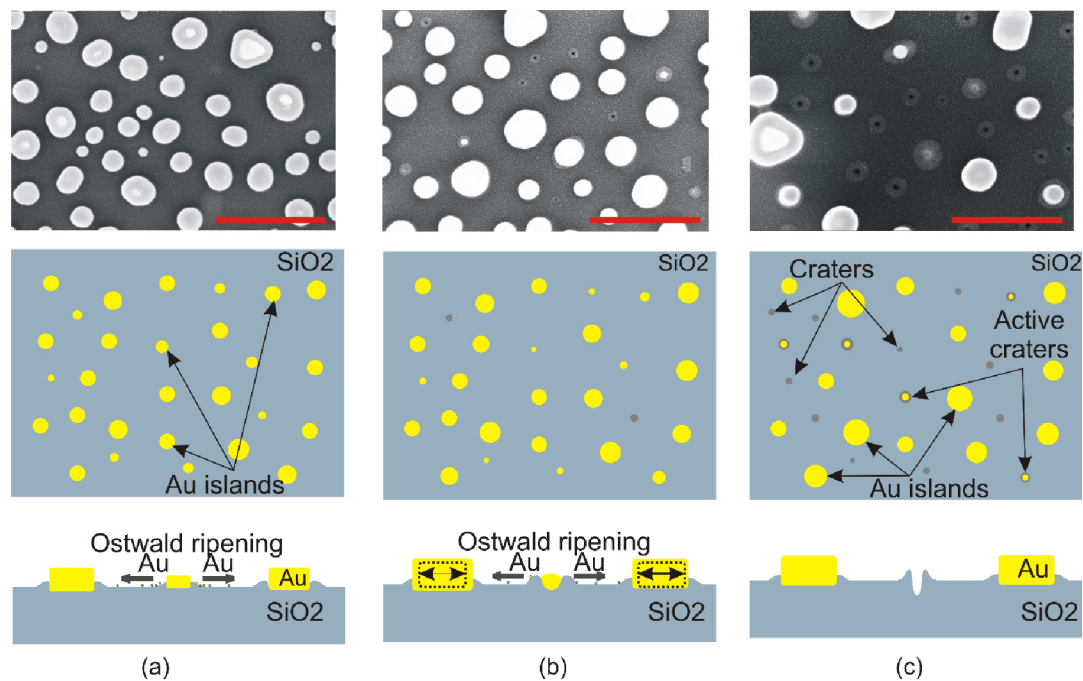
Fig. 5.3: Evolution of morphology of gold islands after annealing at 1000 °C for 5 minutes (a), 3 hours (b) and 24 hours (c) imaged by SEM (upper row) and its schematic representation in a top (middle row)- and cross section (bottom row) view. The scale bar is 1 µm.

5.2.1 Time evolution of particle size distribution

The PSD (Particle Size Distribution) was determined by a processing and analysis of SEM images in the Gwyddion software [53]. A reasonable accuracy and reproducibility was achieved by analyzing hundreds of gold islands spread over an area of 20 µm^2 (Fig. 5.4).

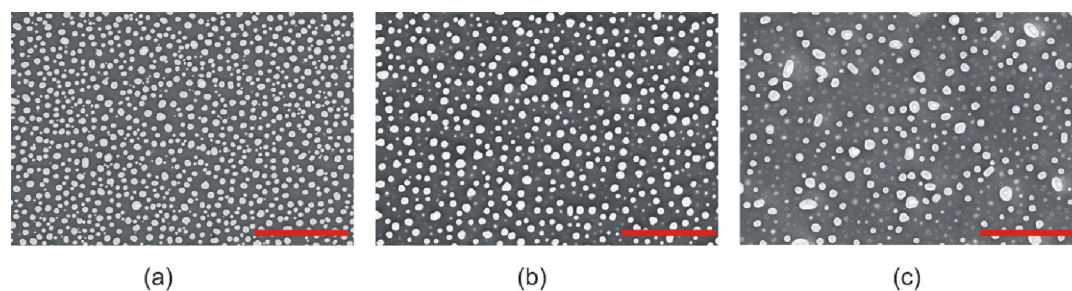Fig. 5.4: SEM images of gold islands after their annealing at 1000 °C for 5 minutes (a), 6 hours (b) and 24 hours (c). The scale bar is 2 µm.

The obtained PSDs for different annealing times are shown in Fig. 5.5. The distributions were fitted by Gaussian-like curves in order to determine the peak positions. In the case, that a bimodal distribution is recognized, two Gaussian-like curves were used for fitting.
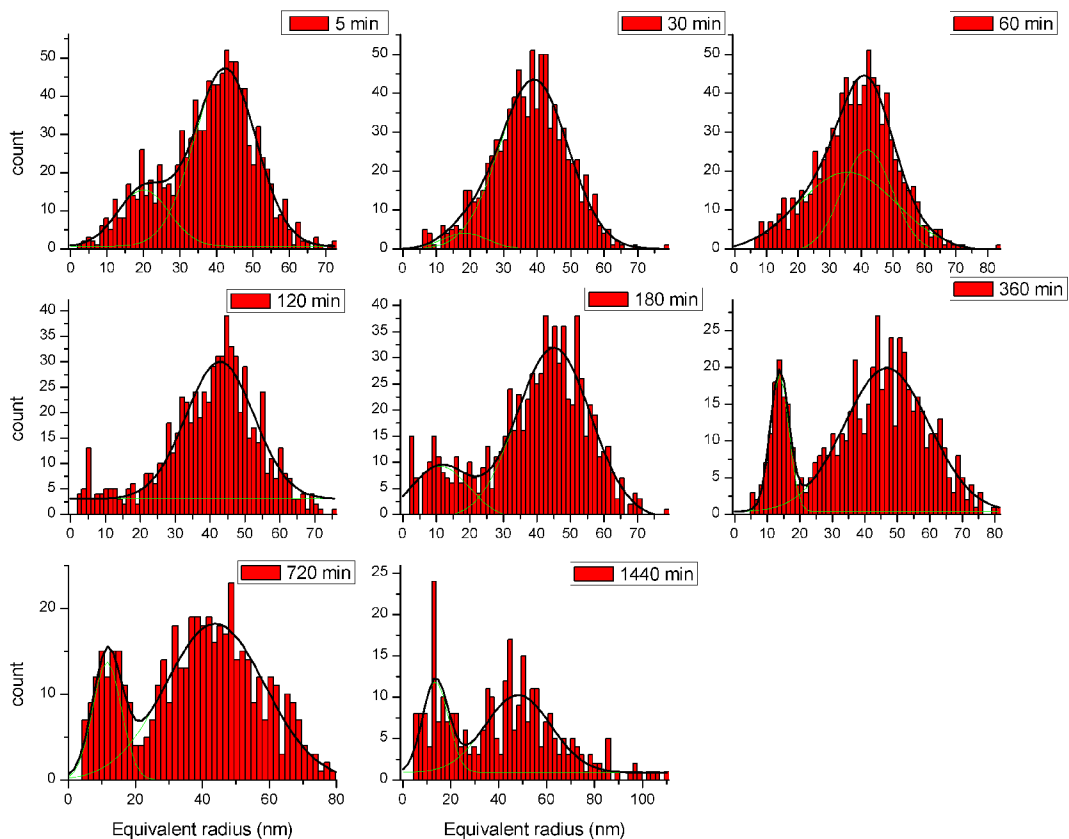
Fig. 5.5: Time evolution of the size distribution function of gold islands annealed at 1000 °C.

After annealing for 5 minutes the gold film is already dewetted and separated gold islands with the mean radius 42 nm are observed. At the same time two populations of these islands distinct in the diameter can be observed. A study of the mechanisms of formation of these two populations just after 5 minutes of annealing was out of the scope of the current work. After additional annealing the population of islands with a small radius quickly diminishes due to the Ostwald ripening, and after 30 minutes of annealing is no longer observed. After 3 hours of annealing the bimodal distribution reappears.

The evolution of PSD of Au islands during annealing can be described by the Ostwald ripening, which is, however, more complex in case of formation of deeply embedded NPs. As will be discussed later, the digging rate is strongly dependent on the particle size, where small islands are being embedded faster. In the first period of annealing, defined as $t < 180$ min, the formed craters are relatively shallow. Hence, the presence of craters does not significantly affect the PSD.

Fig. 5.6: Schematic (upper row) and SEM images (bottom row) of the size distribution evolution influenced by the gold embedding and craters formation during annealing at 1000 °C for the annealing times as 5 min (a), 60 min (b), 180 min (c) and 720 min (d). The scale bar is 1 μm.

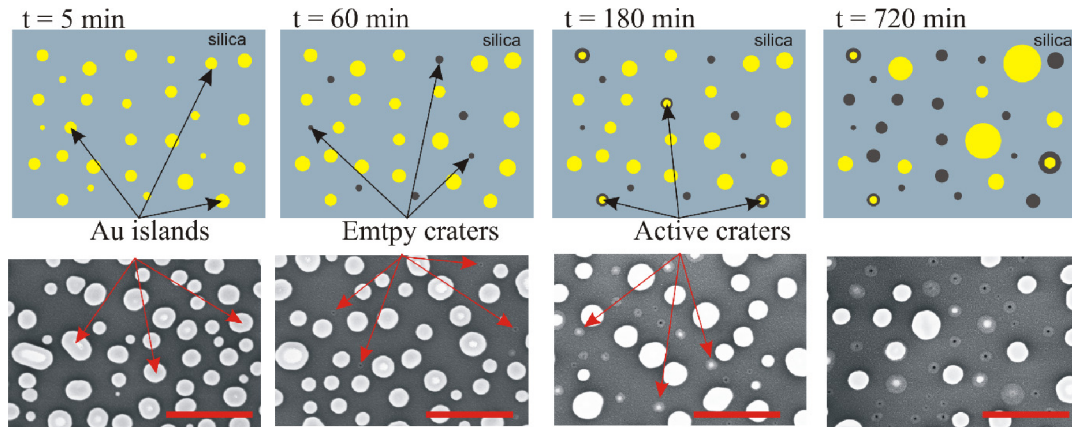A transient state between the first and the second period ($t > 180$ min) occurs around $t = 180$ min when a bimodal distribution reappears (Fig. 5.5, 180 min). The bimodal character of PSD can be explained by an increasing heterogeneous character of the surface. It has been already reported by Zhdanov [43], that the Ostwald ripening on heterogeneous surfaces can induce the bimodal PSD. In our case it is caused by the presence of localized craters. The embedding of islands causes changes of the local curvature which affects the activation energy for detaching the atoms. The flux rate of gold atoms leaving the embedded island is decreased which influences the Ostwald ripening process.

As it was already mentioned, the depth of the craters is inversely proportional to the particle size and increases with annealing time. When the embedding of islands reaches a critical depth (about 1/3 of the island height) the net flux of gold atoms from the islands is rapidly reduced due to the formed rim. These partially embedded gold islands are shown in Fig. 5.7 and will be further marked as "active craters". Due to the reduced flux of gold atoms their size is stagnating in time. The active crater can be then recognized in PSD by the appearance of the second peak as shown in Fig. 5.7c. A schematic drawing of the sample cross section shows their embedding into the silica (Fig. 5.7b).
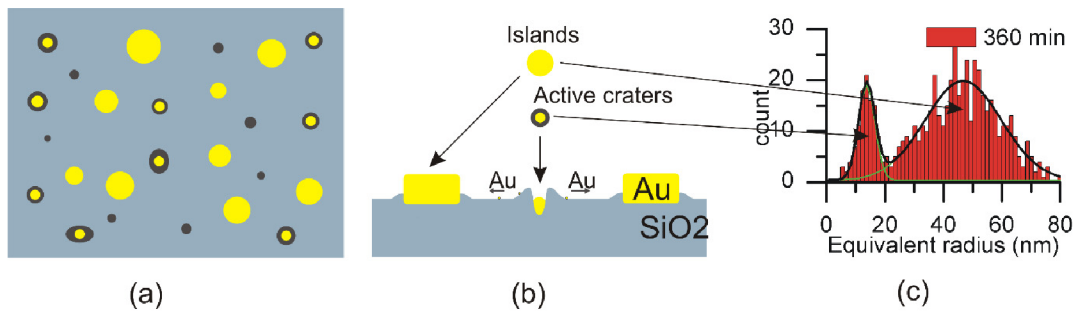
Fig. 5.7: Schematic drawing of the silica surface with Au islands, active and empty craters - top (a) and side (b) view. Corresponding experimental PSD (c) with a characteristic bimodal distribution for gold annealed for 6 hours at 1000 °C.

We have carried out further analysis by the manual labeling of different observed features (islands, craters and active craters) in SEM images. Each feature was marked with the corresponding size and color indicating its type. In Fig. 5.8 blue color represents the crystal islands, green the active craters and red the empty craters. It should be mentioned that the markers were also drawn on the area containing surrounding rims. A separate analysis of PSD was performed for each type of the features.
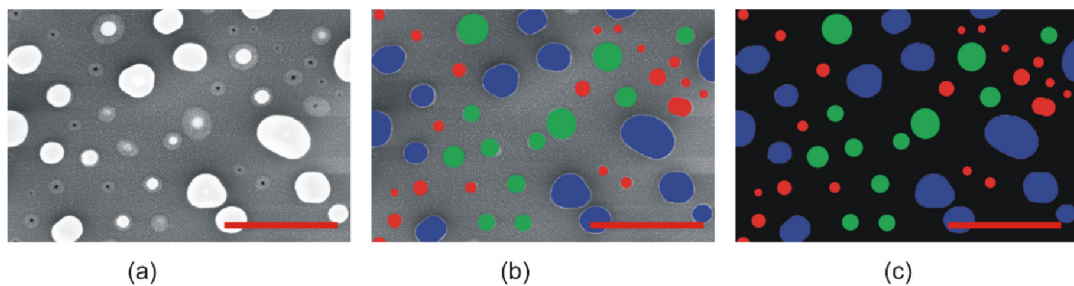
Fig. 5.8: SEM image of the gold islands formed after a 6-hour annealing (a) with manually colorized elements (b), where the islands are blue, the craters red and the active craters green. Extraction of the masks of different colors from the SEM image for elements characterization (c). The scale bar is 300 nm.

As can be seen in Fig. 5.9a, the original SEM image with a bimodal PSD (black line) can be substituted by the PSD calculated only from islands (blue bars) and active craters (green bars). The contribution of the islands to the total PSD is shown in Fig. 5.9b, c. Direct compares of SEM images and calculated PSD shows that specific peak (18 nm) for active islands causing bimodal distribution. Therefore appearance of bimodal distribution is directly related to the digging process.
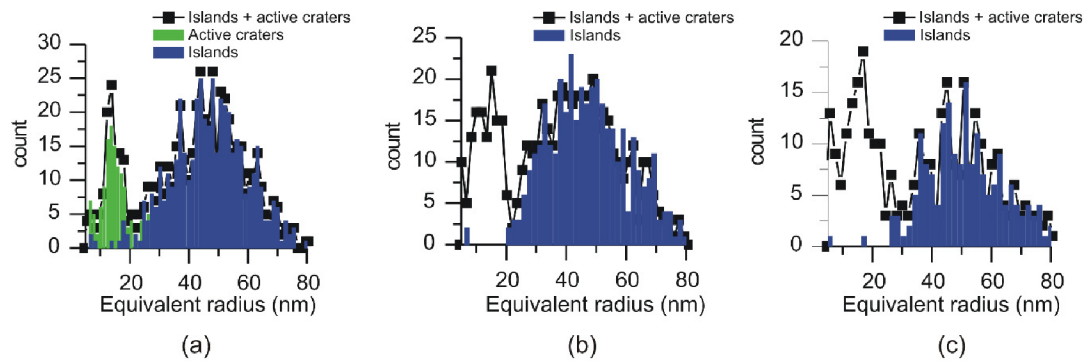
Fig. 5.9: PSD of gold islands obtained by analysis of original SEM images including islands and active craters. The same data analysis was done for an annealing time of 6 hours (a), 12 hours (b) and 24 hours (c).

5.2.2 Statistical analysis of surface features

The proposed manual marking of different features in SEM images enables an additional statistical evaluation. A sufficient statistical sample was obtained by analyzing the area of $21.6\ \mu m^2$ which contains hundreds of islands as shown in Fig. 5.4. The time evolution of counts (i.e. the number of features), surface coverage and the mean size for different features is shown in Fig. 5.10, where all the data were collected from the area of the same size.
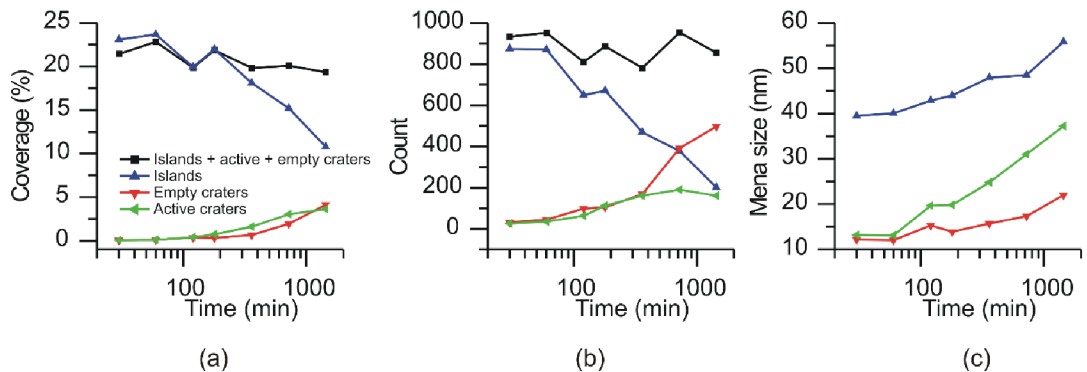
Fig. 5.10: Time evolution of surface coverage (a), counts (b) and mean lateral size (c) of the islands, craters and active craters during annealing at 1000 °C. The data were collected from the area $21.6\ \mu m^2$.

In separated experiments we determined the mass thickness of a gold film after annealing for different times using a chemical analysis [65]. Based on these results the conservation of a gold volume (mass) on the surface will be assumed in further discussions. A decrease of the mass thickness due to evaporation didn't exceed 3 %. The decrease of the surface coverage and number of islands (counts) continues at the expense of the increasing mean size of gold islands. These expected results correlate well with the Ostwald ripening process on the flat substrate.

More interesting appeared the evolution of empty and active craters. The mean size and number of empty craters is continuously growing (red lines in Fig. 5.10). This indicates that empty craters are formed continuously. The size of the craters is related to the life time of the islands, which is proportional to their size. Hence, the longer time necessary for disappearing the larger islands results in larger empty craters. The similar trends have been observed for the active craters with the gold remaining inside. The longer annealing times result in larger morphological changes enabling that the larger islands are trapped in the crater. The growing number of the active craters shows that the longer annealing times enable a deeper embedding at which the island size stagnates.

It should be pointed out that the sum of the number of islands, active and empty craters remain the same as can be seen in Fig. 5.10b. These results indicate that all the islands formed after the initial dewetting are transformed into the larger islands, active craters or empty craters. Hence, it can be concluded that the active and empty craters are "fingerprints" of the original islands.

5.3 Characterization of the digging process and crater formation

Previously, we have shown that the time evolution of PSD is influenced by the surface heterogeneity and surface modification. This part is devoted to a detailed analysis of the digging phenomena. Embedding or digging phenomena can be described as a local modification of the surface morphology leading to the formation of a crater with the surrounding rim, the morphology of which evolves simultaneously with the size changes of gold particles (islands) during annealing. The long-term annealing experiments were performed at 1000 °C, close to the melting point of the bulk gold (1064 °C) [66]. The samples were prepared by the thermal deposition of a 10 nm nominal thick gold film on a 300 nm thick thermally grown silica layer on a silicon wafer.

5.3.1 Crater morphology and different stages of digging

The craters formed in the silica substrates have a different shape and size. AFM images of the craters formed after annealing at 1000 °C for 24 hours and processed in aqua regia for gold dissolution are shown in Fig. 5.11. Imaging the surfaces with islands by AFM is complicated due to large differences in the height scale. Therefore, the imaging of larger areas is carried out mainly by SEM. As can be seen, each crater is surrounded by an adjacent rim being formed suggesting that the rim is formed only on the island perimeter. The width of the rim depends on an evolution of the island size during the Ostwald ripening and differs for increasing and shrinking islands.

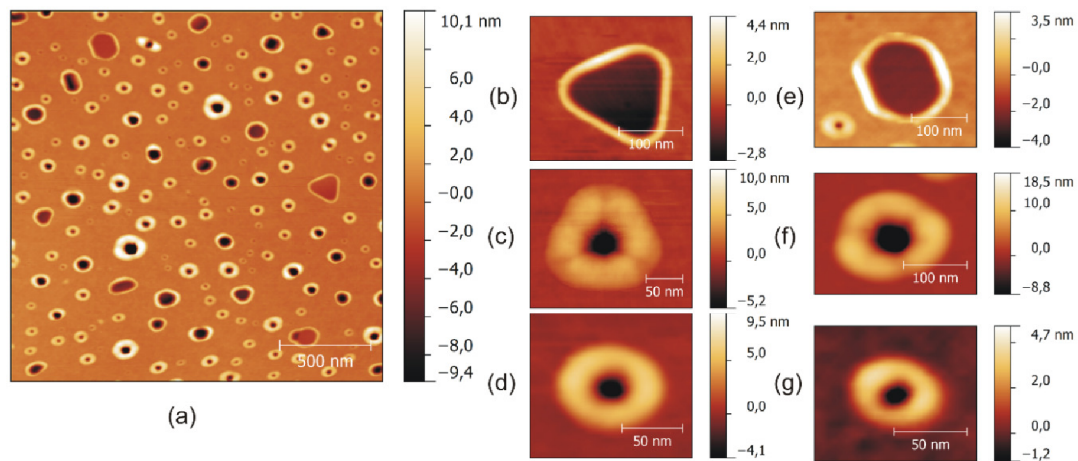Fig. 5.11: AFM images of a silica substrate with a gold layer after annealing at 1000 °C for 24 hours and gold dissolution (a). Different types of the craters observed on the surface (b - g).
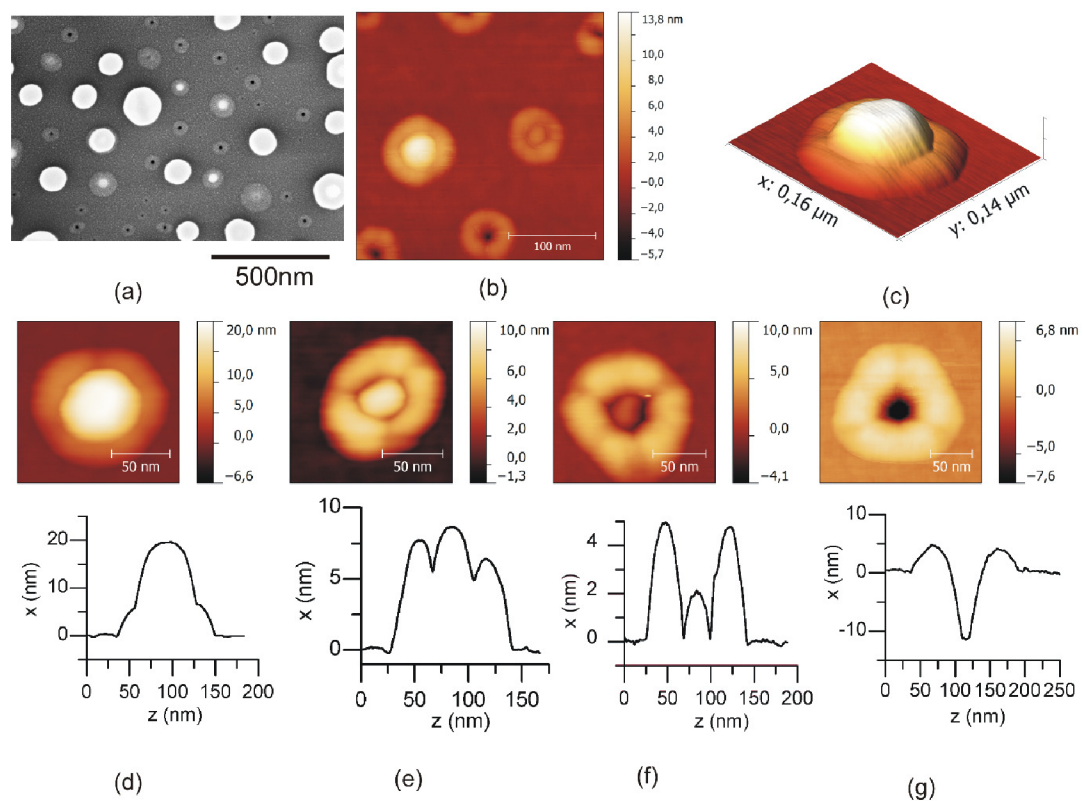

Fig. 5.12: SEM (a) and AFM (b - g) images of the craters and gold islands formed after annealing at 1000 °C for 12 hours. Different stages of the gold embedding (d - g) with the corresponding height profiles.

The characterization of different types of craters is important for the understanding of the digging process. Based on the analysis of SEM and AFM images, three different types of craters have been identified as follows:

Crater type I: the largest (side 200 – 300 nm) and relatively shallow (1 – 5 nm deep) craters are shown in Fig. 5.11b, e. They are typical for large faceted single crystal islands continuously growing during the Ostwald ripening process with the shaper following the island shape. Different shapes of the craters correspond to different crystallographic orientations of the islands. The height of the surrounding rim is small (2 – 5 nm) compared to the other types. The bottom of the crater is atomically flat.

Crater type II: the size of the crater is of an intermediate range (100 – 200 nm) as shown in Fig. 5.11c, f and Fig. 5.12b - g. Here, the relatively wide rim ($\approx$ 50 nm) with the height 5 – 15 nm can be identified. The height of the rim significantly changes along the island perimeter and forms a "rim decoration". The remaining gold islands are typically present inside this type of the craters as shown in Fig. 5.12d – f. The formation of this type is associated with intermediate-sized islands, the size of which is reduced due to the Ostwald ripening.

Crater type III: the smallest type of the craters (< 100 nm) is characteristic in a symmetrical rounded rim with no decoration and no gold inside the crater as shown in Fig. 5.11d, g and in Fig. 5.12a. In SEM images they appear as small pits. They are formed from the small gold islands observed mainly after the initial dewetting. The gold islands disappear during annealing and, consequently, the digging is terminated.

In Fig. 5.11b, e the rimmed craters type I formed from faceted islands are shown. The similar faceting can be found for the most of the craters type II, where the width of the rim is bigger as shown in Fig. 5.11c, f and Fig. 5.12 d - g. It confirms a direct correspondence between the shape of crystal borders and the shape of the crater and rim.

We assume that the formation of the rim and increase of the crater depth proceed simultaneously during the island shrinking caused by the Ostwald ripening. The relevance of this model is supported by experimental observations. The transformation of morphology can be explained by an analysis of a motion of the island-silica-air triple interface line.

Let the volume of the silica rim constantly grow with annealing time. It means that a "linear source" continuously delivers a new material to the rim. The volume of the rim depends on the annealing time and is proportional to the length of the triple line. The height of the rim around a triangle-shaped monocrystal island is different in the corners and along the facets as depicted in Fig. 5.13a. In Fig. 5.13b the segments of circular areas (orange) of the same diameter r located at the side of the triangle and in the corner are schematically shown. The length of the linear source inside these areas is the same ($2r$), thus the volume of the released material inside the marked area in the corner and on the side is the same. Nevertheless, the segment area in the corner is larger compared to the side one (Fig. 5.13b). Consequently, the height of the rim is smaller in the corner than on the side. Hence, the shape of the triple phase line influences the rim height.
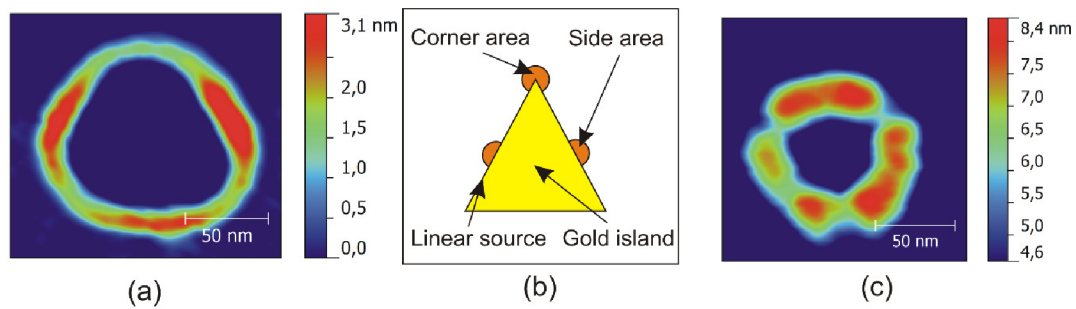
Fig. 5.13: AFM topography image of a smaller (a) and larger (c) rim after gold dissolution. A schematic view of the gold island and the effect of the "linear source" (b).

The proposed mechanism can be used for explanation of the rim decoration observed in the case of the crater type II. As can be seen in Fig. 5.13c, the rim decoration consists of the humps on each faceted side. The correlation between the shapes of the triple phase line and rim topography is evident.

Experimental observations have shown a wide range of the rims as can be seen in Fig. 5.14a. Some of the rims are extremely wide compared to the others. This can be explained by the fact that the size of gold islands changes and the "linear source" of silica follows the triple phase line. The smaller islands which are shrinking during the annealing are surrounded by a wide rim shown in Fig. 5.14c, d. In this case the "linear source" is moving with the shrinking islands and the rim width grows. The original size of the gold islands can be then estimated from the size of the outer perimeter of the rim. The process is terminated when the gold island disappears. The empty craters (Fig. 5.14e) are typically small and assigned as the type III.

The size stagnation of gold islands during annealing was already discussed in part 5.2.1. The image in Fig. 5.14d shows that the islands assigned to the figures (c) and (d) have a similar radius but the width of the rim is significantly different. It indicates that when the gold islands of initially different sizes reach the same size due to the size stagnation, the different size of the rims is observed.
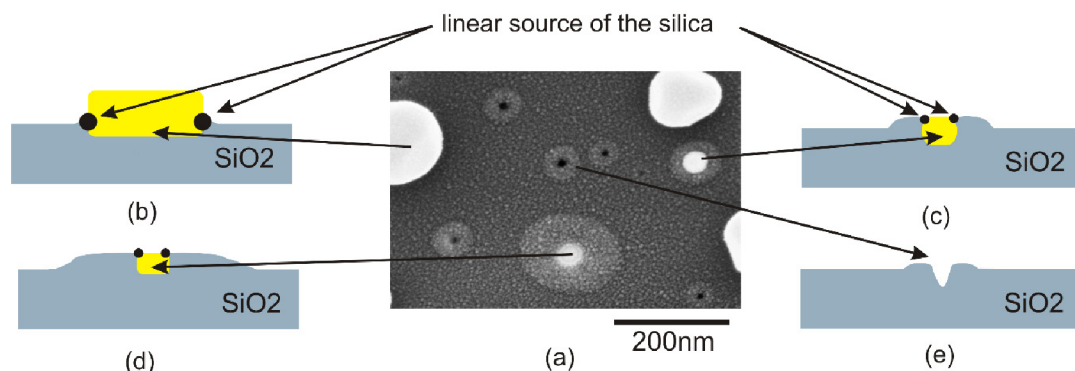

Fig. 5.14: SEM image with the rims formed around the islands (a). A schematic view of the islands surrounded by the rims of different size (b, c, d). An empty crater with the rim (e).

73

5.3.2 Mass transfer and depth analysis

Characterization and classification of the crater types presented previously was mainly based on the analysis of the crater size and rim shape. Further information about the digging process can be obtained from the analysis of the crater and rim volume. Additionally, small islands are typically found in deeper regions than the bigger ones, which suggests that the small islands are being dug in faster. In order to investigate the mass transfer and correlation between the island size and the crater depth, a simple analytical model was proposed.

Let's assume the following:

      1) the silica rim is formed by the release of a material provided by a "linear source" at the triple-phase line with the flux τ,

      2) the released material is taken from the crater below the island,

      3) the volume of the material added to the rim V_{rim} is equal to the volume V_{cr} removed from the crater.

The volume of the rim V_{rim} depends on the length of the triple-phase line and the annealing time (Fig. 5.15a, b). The rim volume can be then calculated as $V_{rim} = \tau l t = \tau 2\pi r t$, where l is the length of the gold island perimeter (triple-phase line), r is the equivalent island radius and t is the annealing time. The volume of silica removed from the bottom of the island V_{cr} can be calculated as $V_{cr} = \pi r^2 h$, where h is the depth of the crater (Fig. 5.15c). From the condition that $V_{rim} = V_{cr}$ follows that the depth of the crater is inversely proportional to the island/crater radius:

$$h = \frac{2\tau t}{r}.$$

Eq. 5.1

The relation between the crater radius and depth can be experimentally determined by the analysis of AFM images shown in Fig. 5.15a. The measurements at a sufficiently low noise level were achieved only for the samples annealed for 2, 3, 6 and 24 hours. The data were analyzed by the Gwyddion software which allows us to select individual craters as shown in Fig. 5.15a. For each selected crater the area (represented by the equivalent radius) and maximal depth were determined. The correlation between the crater depth and the reciprocal value of the equivalent radius for different annealing times is shown in Fig. 5.15c. The presented results confirm the linear dependence given by Eq. 5.1, i.e. that the narrower craters are deeper.
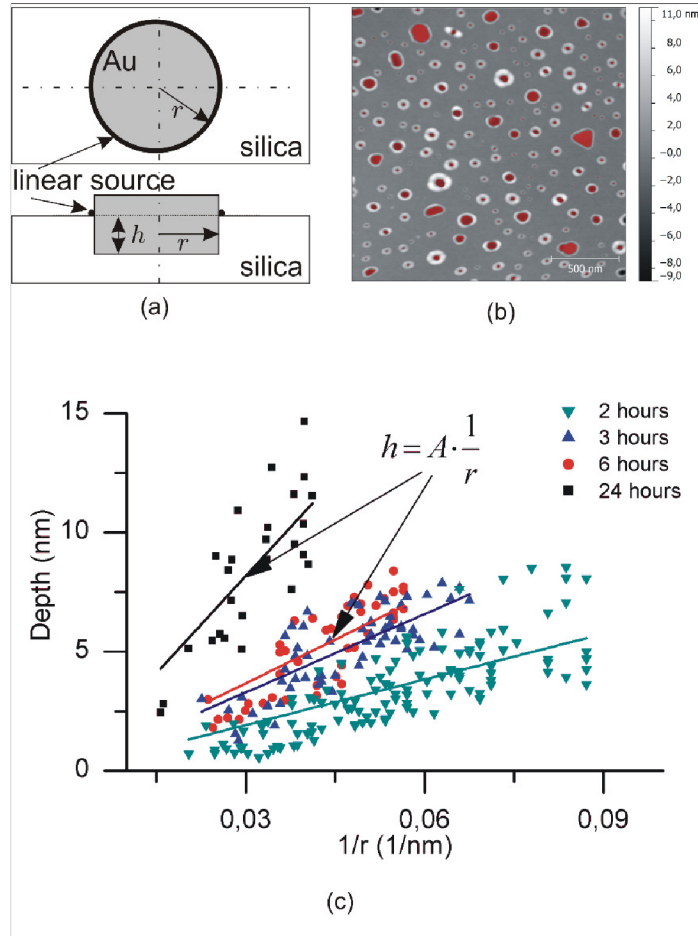
Fig. 5.15: A schematic view of the sphere-linear source configuration (a). AFM image of selected craters in a silica substrate surface annealed for 6 hours and chemically processed afterwards to remove gold (b). Dependence of the maximal depth of craters on their reciprocal radius for different annealing times (c).

According to Eq. 5.1 the slope of the linear dependence is given by the expression $A = 2\tau t$, which is proportional to the volume of the transferred silica per unit length of the perimeter. The fitted parameters A are given in Tab. 5.1. The rising parameters A (the volume of transferred silica) for increasing annealing times correspond to the growing volume of the craters and rims. The time evolution of the fitted parameter A is shown in Fig. 5.16a. Using the linear formula $A = 2\tau t$ we can fit this dependence by the least mean squares method and get for τ the value $\tau = 0{,}0012$ nm^{2}s^{-1}.

Time (hours)	2	3	6	24
A (nm^2)	63±1.7	109±2.6	122±3.7	277±11

Tab. 5.1: Fitting of experimentally measured relations between the equivalent radius and the cater depth for different annealing times.

The digging velocity v_{digg} normal to the surface can be obtained from Eq. 5.1 as follows

$$v_{\mathrm{digg}} = \dot{h} = \frac{2\tau}{r}.$$

The dependence of the digging velocity on the island radius is shown in Fig. 5.16b. The experimental results and the proposed model for silica mass transfer are in a good agreement.

(a)

(b)
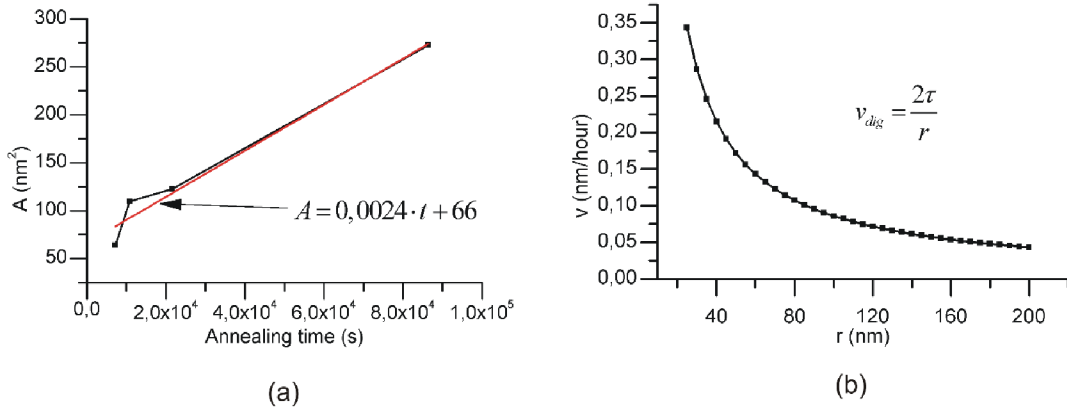
Fig. 5.16: Time evolution of the volume transferred per the unit perimeter length A (a). Digging velocity v_{digg} as a function of the islands radius for theoretical (solid curve) and experimental (squares) data (b).

The volume of the transferred silica can be also evaluated using 3D AFM images of the craters. As previously mentioned, the proposed model assumes that the silica is transferred from the area bellow the island to the rim. Then the volume of the crater and the rim should be equal. The analysis of AFM images enable direct estimation of the both volumes. The representative high quality AFM images used to such a volume determination are shown in Fig. 5.17.

(a)

(b)
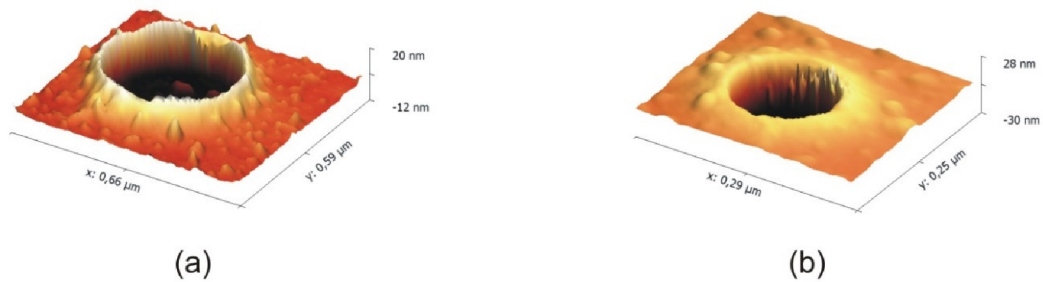
Fig. 5.17: AFM images of two different craters with rims (a, b) used for the volume analysis after gold removal.

The calculations were performed using the Gwyddion software which allows measuring the volume of objects under (craters) or above (rims) the selected area - see the mask selection of the plane for the crater and rim volume estimation in Fig. 5.18. To minimize the influence of the AFM tip, the larger craters were selected for the analysis where the image distortion caused by the tip can be neglected.
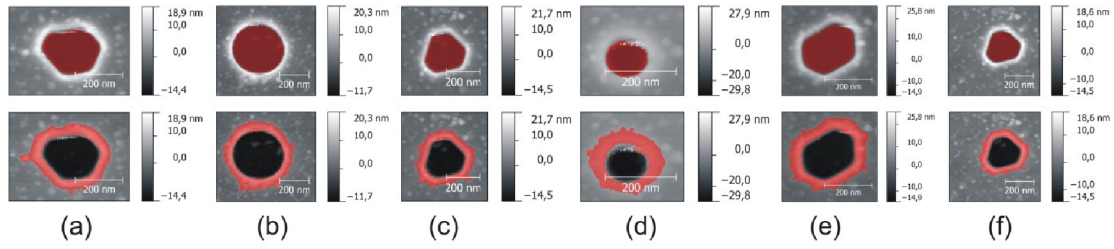
Fig. 5.18: AFM images of the craters with the selected plane of the craters (upper row) and rims (bottom row) used for the volume calculation. The estimated volumes of the relevant rims and craters were compared as shown in Fig. 5.19. The mean relative difference between the estimated volumes is 15 %, which can be caused by the AFM imaging- and data analyses inaccuracy.
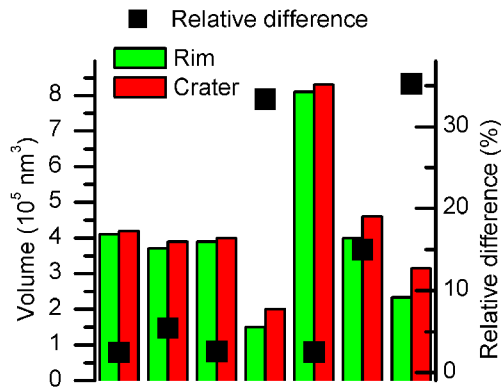
Fig. 5.19: Comparison of the volumes of the selected craters and corresponding rims. The relative difference is indicated by the black squares.

5.3.3 Digging into different types of silica substrate

The Au island embedding has been observed on various oxide substrates. In this section we present the results of comparative studies of the gold embedding into different silica substrates, i.e. quartz, fused silica glass and commercially available silicon wafers–with thermally grown silica.

It should be mentioned that the previously reported observation of the gold embedding into the thermal silica layer on the silicon substrate was done by Bowker [60]. The suggested mechanism of the island digging into the substrate is related to the smaller growth rate of the thermally grown silica layer under the gold islands compared to that at the bare surface. To verify this mechanism the high temperature annealing of a silica substrate such as quartz or fused silica glass, where silicon is not present, should be carried out.

Four different silica substrates were chosen. The first two, crystalline (quartz) and non-crystalline (fused) silica, do not contain an underlying silicon substrate. Other two tested substrates were composed of a silica top layer on a silicon wafer. The first of the latter type

77

of the substrates was prepared by the thermal growth during the silicon wafer annealing at 1000 °C for 12 hours. The thickness of the silica layer measured by ellipsometry was 380 nm. The second substrate with the silica layer was a commercially available sample with the 270 nm-thick silica film on the silicon (100) wafer (On-Semi).

All the substrates were cleaned in IPA and covered by a 10 nm-thick gold layer. Annealing at 1000 °C for 12 hours was performed simultaneously for all the samples to avoid difference in annealing and cooling conditions. As can be seen in Fig. 5.20 (upper row) the formation of gold islands is observed on all substrates. The embedding process and rim formation was clearly recognized after the gold removal in aqua regia as shown in Fig. 5.20 (bottom row). The presence of the formed craters is evident.

It should be pointed out that in experiments with the silica substrates the crystallization of silica surfaces was observed. It might have been only caused by the fact that the experiments with the silica substrates were performed in a furnace which did not allow the fast cooling rate and so the cooling time to room temperature was ~ 6 minutes. Despite this crystallization, the formation of the craters and rims was clearly identified.
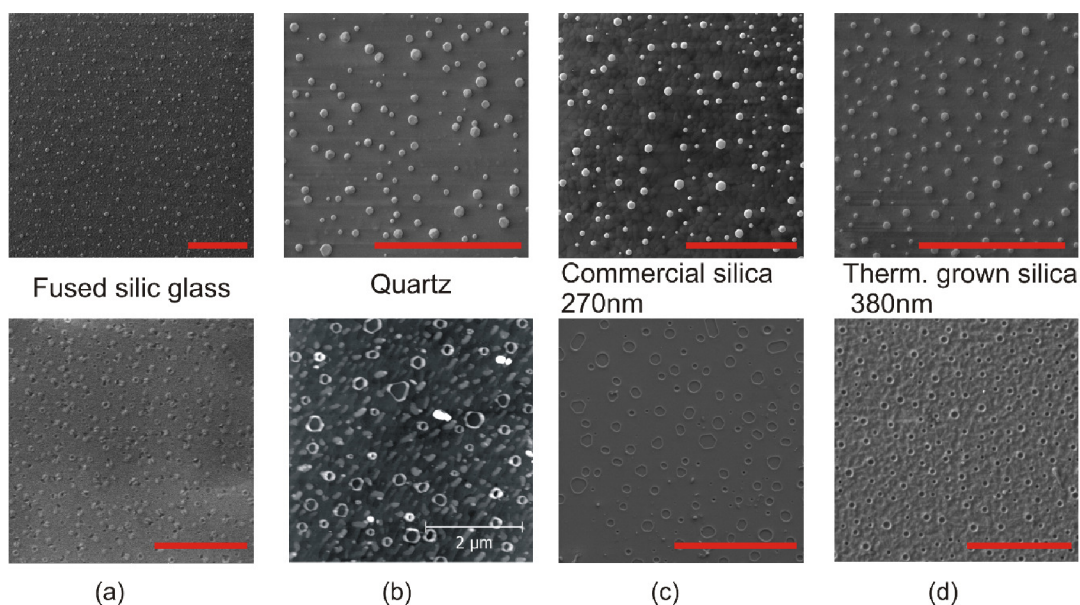
Fig. 5.20: Images of the different silica surfaces with a deposited 10 nm-thick Au layer annealed for 12 hours at 1000°C taken before (upper row) and after (bottom) gold removal: fused silica (SEM), (a); quartz substrate (AFM), (b); commercial silica layer (270 nm, SEM), (c); and thermally grown silica (380 nm, SEM), (d). The red scale bar is 5 μm.

The experimental results with quartz- and fused silica (Fig. 5.20 a, b) substrates show that embedding is not conditioned by the presence of silicon in the substrate. Further discussions about the digging mechanism can be thus focused only to the interface between silica and a gold island. It can be concluded that the silica mass transfer is observed at the interface of any type of the silica substrate and a gold island at high temperatures.

78

It should be mentioned that the unwanted silica surface crystallization was observed after slow cooling only in the case when gold islands were present on the surface The annealing of the bare fused silica surface (without deposited gold) did not lead to silica crystallization as shown in Fig. 5.21a. Therefore, the presented results indicate that the surface crystallization is catalyzed by the gold islands.

<div align="center">(a)   (b)</div>
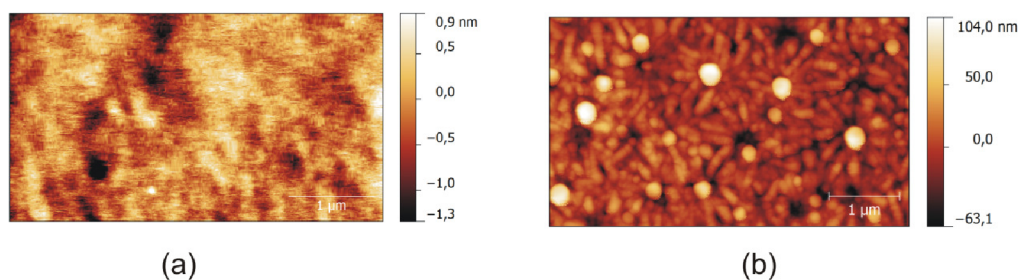
Fig. 5.21: AFM images of the fused silica glass substrates annealed at 1000 °C for 12 hours a) without deposited gold and b) with a deposited 10 nm-gold layer.

5.3.4 Depth of Au island immersion

A deep immersion of small gold islands (particles) was observed by SEM imaging of a sample cross section (Fig. 5.22). The original gold islands are buried in the form of spherical particles in the silica bulk in the depth 40 – 80 nm (Fig. 5.22a - c). The particle radius is approximately 15 nm and correlates with the peak of active craters observed in PSD and described in part 5.2.1. This observation indicates that the most effective digging process is performed only by the islands inside of a narrow size window.

<div align="center">(a)   (b)   (c)</div>
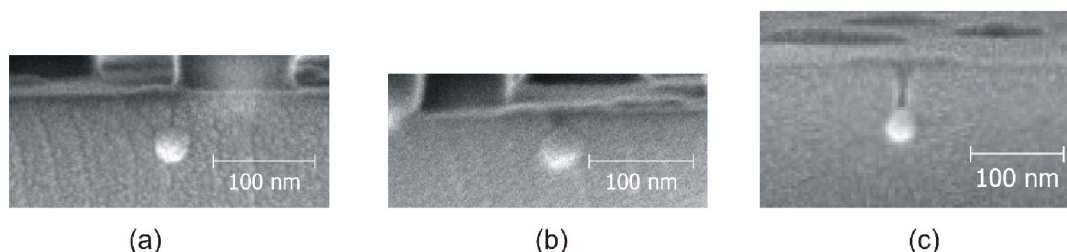
Fig. 5.22: SEM-images of the cross section of a silica sample with embedded gold is particles of various sizes.

There is a narrow channel above each particle so the gold particles are not fully encapsulated. A schematic of gold embedding evolution is shown in Fig. 5.23. The size of the island/particle is reduced until a critical depth is achieved. In such a case the further size reduction is stopped while the digging process continues (Fig. 5.23c, d).
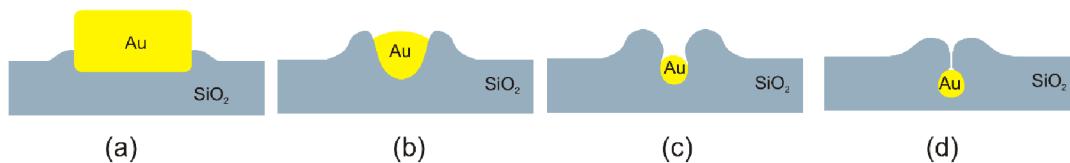
Fig. 5.23: A schematic of the embedding process of a gold island into the silica substrate. The size of the island/particle gradually decreases during the digging process (a - c) until the specific depth is achieved. The particle is dug deeper into the substrate having a narrow channel above it (d).

Deeply immersed gold particles are usually not visible by secondary electrons (SE) in SEM imaging. However, these embedded particles can be imaged by "chemically" more sensitive backscattered electrons (BSE) as shown in Fig. 5.24. The same area was imaged both by SE and BSE electrons.

BSE images correlate with the cross section images showing that some of the gold islands are deeply embedded into to the substrate. This observation also confirm that long time annealing leads to formation of three different types of elements - islands, and empty and active (with gold island) craters as was previously mentioned in part 5.3.1.
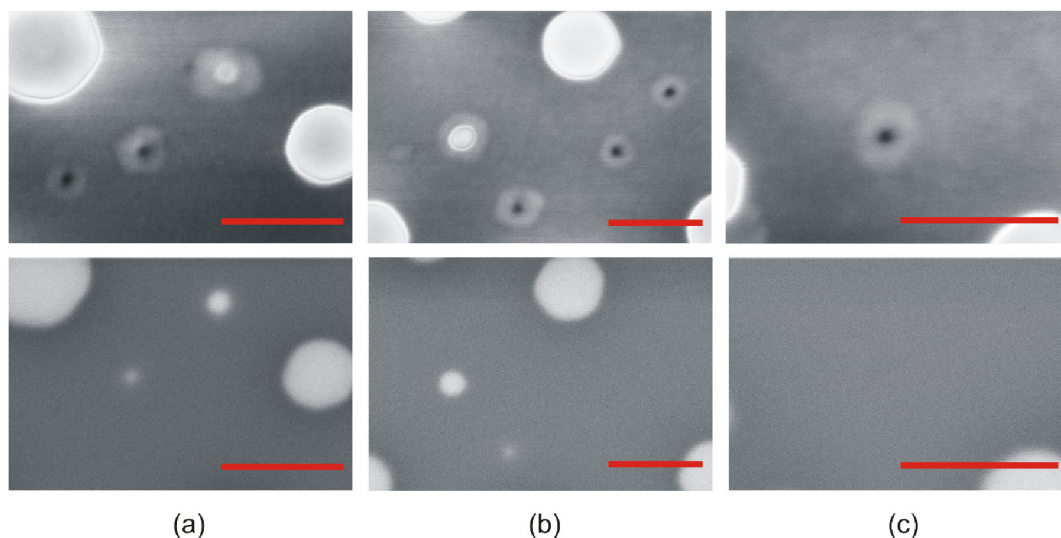
Fig. 5.24: SEM images provided by secondary electrons (upper row) and backscattered electrons (bottom row) related to different sites (a, b) of the silica surface possessing gold islands, and empty and active craters. Details of the empty crater (c). The scale bars are 100 nm.

5.4 Discussion of the mechanism of the embedding process

Several stages of the gold digging process on the silica substrate have been described in the previous sections. Although several authors have already reported on the digging process,

any satisfactory description of the digging mechanism has not been reported yet. Nevertheless, several different scenarios have been suggested by other groups and will be discussed. It should be noted that annealing has been done in an oxidation atmosphere. This fact makes a major difference from the most similar investigation carried out under ultra-high vacuum (UHV) conditions [62]. In the oxidation atmosphere the reactive oxygen is involved in chemical reactions responsible for the silica formation.

Our experimental results can be summarized as follows: During the digging process the craters and surrounding rims are formed simultaneously. Silica is transferred from the region below the islands to the rims (see part 5.3.2). The mass transfer of silicon can be achieved through the bulk of gold islands or around the interface along the gold-silica substrate. The most probably the latter way of mass transfer was prevailing and so the concentration of silicon in the bulk was very small (deeply bellow the concentration corresponding to the eutectic point – 18.6 %). This is supported by the fact that the faceted shape of the craters was performed when islands were crystalline. We assume that the chemical composition of the bulk gold before and after the experiments is not changed.

Recently, Bowker et al. reported formation of craters in a silica substrate under the gold islands after annealing at 1100 °C and showed encapsulation of Au nanoparticles into this substrate [60]. They suggested that the digging process is caused by the upwards growth of a silica layer from the substrate silicon, when the growth is slower under the gold islands due to the lack of oxygen. Another possible scenario was discussed by Powell [58], Hu [59], Ajayan [67], Spolenak [61] and Klimmer [68] on different metallic - oxide systems. In addition to thermal annealing, the digging process may be also induced by ion beam irradiation which leads to temperature enhancement and metallic film dewetting as well [69]. The most researchers have suggested that the embedding of metallic particles is driven by the capillary forces and minimization of the surface energies. This scenario assumes a viscose substrate which can be formed at elevated temperatures provided by heating or ion bombardment. According to the Hu, the embedding driving force depends on the parameter a

$$a = \frac{\gamma_s + \gamma_p - \gamma_{p,s}}{\gamma_s} = 1 + \cos\vartheta, \qquad \text{Eq. 5.3}$$

where γ_s is the surface energy of the viscous substrate, γ_p is the surface energy of the particle (island), $\gamma_{p,s}$ is the corresponding interface energy and ϑ is the contact angle between the particle and the substrate. Different stages of embedding are shown in Fig. 5.25 with a corresponding value of the parameter a.
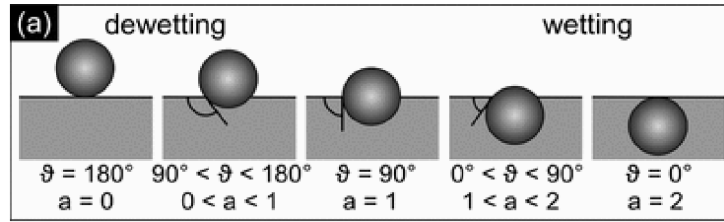
Fig. 5.25: Schematics of the final equilibrium positions of solid spheres sunk into a viscous substrate depending on the wetting conditions as expressed by the parameter *a*, taken from [68].

In the presented work it has been shown that the craters are formed on any type of the silica substrate (see part 5.3.2) and their depth is strongly dependent on their size (see part 5.3.2). It can be deduced, that our experimental observations do not correlate with the digging mechanism proposed by Bowker, where the digging process is conditioned by the presence of bare silicon underneath. Hence, in our case this scenario can be ruled as the digging process was observed also for the quartz. The second scenario, proposed by Powell [58], requires the existence of a viscous substrate and at first look it does not explain the deep embedding shown by the SEM cross section images (Fig. 5.24). Nevertheless, the intention of this work is to demonstrate that viscosity of the gold/silica interface can decrease and also that capillary forces can cause deeper digging.

It is well known that gold-silicon systems form gold silicide with the eutectic point at 363 °C and concentration 18.6 %, see the phase diagram in Fig. 5.26. The required silicon can be obtained from the silica decomposition catalyzed by the gold island without the access of oxidative atmosphere. Hence, annealing at 1000 °C may cause the formation of a thin interface layer between the gold and the bare silica composed of an Au-Si solution. The presence of the Au-Si layer would result in changes in the surface energy of silica and in decrease of its viscosity. On the triple phase line the Au-Si solution is exposed to oxidative atmosphere and thus silicon is released and forms the silica rim. It should be pointed out that the silica decomposition catalyzed by gold was reported by the group of Roldan [62] under ultra-high vacuum conditions (non-oxidative atmosphere) which does not lead to the formation of the silica rim. However, the proposed mechanism does not explain how oxygen, released into oxide after the formation of surface silicide, is accumulated in the substrate. Therefore, more experiments are necessary to fully prove this mechanism.
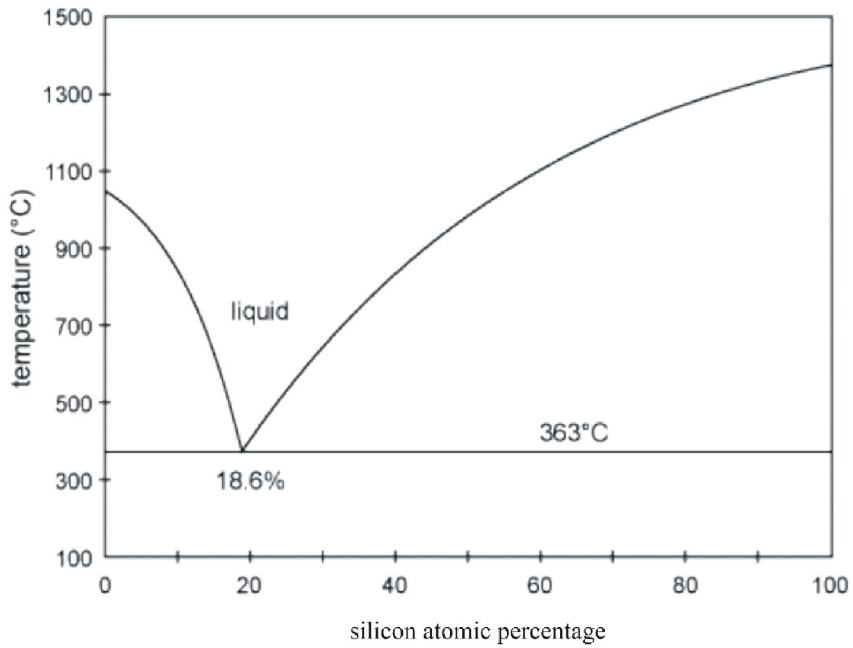
Fig. 5.26: Gold-silicon phase diagram. If a thin viscous interface layer is formed, capillary forces become significant and influence the embedding. In the viscous interface the upward flux of silica is driven by the wetting, the contact angle is in the range $0° < \vartheta < 90°$. The flux is stopped on the triple phase line where silicon oxidizes and forms the rim. This mechanism causes a continual silica transfer from the area below the crater to the rim, until the thermodynamic equilibrium is reached.
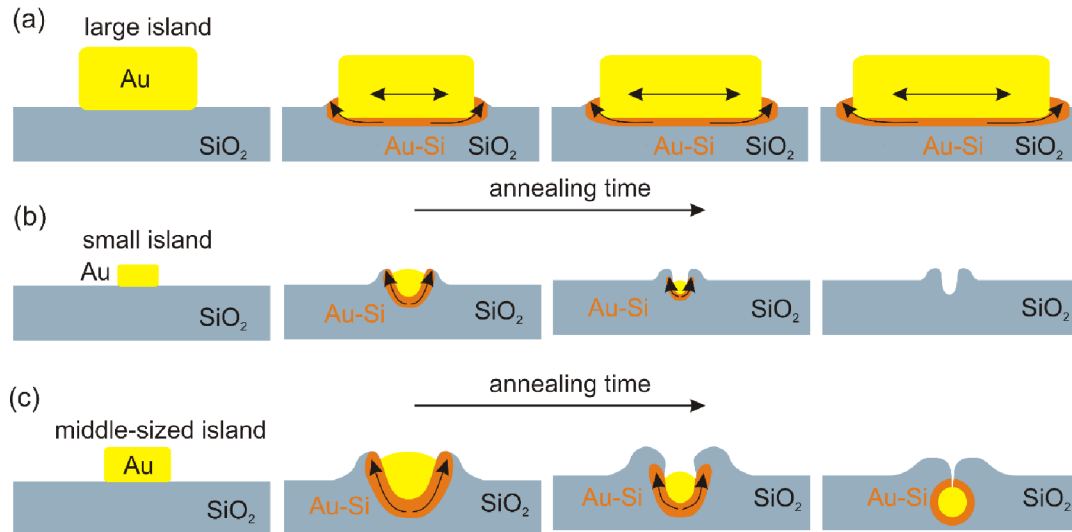
Fig. 5.27: Schematic of the time evolution of the islands with large (a), small (b) and medium (c) size during annealing followed by the formation of large single crystals (a), empty craters (b) and deeply embedded gold particles (c).

In Fig. 5.27 different scenarios according to the size of the initial islands are schematically shown. The dewetting process is relatively quick and separated islands are formed in the tens of second. On the other hand, the formation of craters is a slow process ongoing for hours (days). During the long annealing, the Ostwald ripening process causes significant changes in island sizes. Additionally, it has been shown that the small craters are dug faster. The interplay between the digging and the Ostwald ripening causes the formation of large gold islands (Fig. 5.27a), small empty craters (Fig. 5.27b) and deeply embedded gold particles (Fig. 5.27c).

Experimental observation of deeply embedded gold particles should be discussed and explained as a result of capillary forces. The typical radius of deeply embedded particles is in the range of 10 – 25 nm. It has been shown that size of these particles is not changing with the digging depth (see part 5.3.4). A continual digging can occur during the whole annealing. Termination of the digging process can appear when the thermodynamic equilibrium is established or when the full encapsulation of gold islands is achieved. In both cases the essential conditions for the digging process are not valid any more. It should be point out that the cross section SEM images did not show the full encapsulation and, hence, the digging process was not terminated. Embedding driven by the capillary forces proposed by Powell offer the explanation for the craters not deeper than islands diameter. To explain deeper embedding, the proposed theory should be extended by a possible crystallization of silica. It has been reported by Santos at al. [70] that amorphous silica initially covered by a gold layer undergoes crystallization during the annealing at 900 °C. The crystallization causes an increase of the silica density about 1 %. Thus the volume of the crystalline silica is reduced compare to the amorphous one. This scenario offers the explanation for the observed narrow chimney above the deeply embedded islands. Hence, the full encapsulation cannot be reached and then the capillary forces continuously drive the silica mass transfer from the below bottom of the crater to the upper rim.

5.5 Conclusion

We have demonstrated that high temperature annealing (1000 °C) of the gold islands on the silica substrate causes the embedding of the islands into the substrate. The depth of the majority of craters formed in the silica surface is in the range of 1 – 15 nm but also deeply embedded gold islands have been found to be in the depths of 40 – 80 nm. The perimeter of the craters is circumscribed by the silica rim. It has been demonstrated that faceted shape of the craters corresponds to the shape of the islands. The rim is therefore formed on the triple phase boundary by silica transfer from the crater bottom to the rim. According to the size of islands three different features – large islands with tight rim, middle size craters with remaining gold inside and small empty craters – were described.

The size of the individual islands evolves during annealing due to the Ostwald ripening process. Time evolution of the particle size distribution (PSD) was monitored in time frame of 5 min – 24 hours. The statistical analysis has shown that the initial islands are transformed into the large growing islands, craters with gold remaining inside or empty craters. The evolution is driven by an interplay between the Ostwald ripening process and the embedding

process. The appearance of the secondary peak in PSD (radius 18 nm) observed after 3 hours of annealing is caused by surface heterogeneity induced by embedding.

The data analysis of AFM images have shown that the size of the islands strongly influence the digging rate. The linear correlation between the reciprocal size and the depth of the craters shows that the small islands are digging faster. Also the volume of the rim and corresponding volume of the craters are very similar. The achieved results corresponds well to the proposed theory that the mass transfer is performed at the triple phase line.

Based on the experimental observations a possible mechanism has been discussed. High temperature annealing can result in formation of a viscous Au-Si solution at the interface between silica and gold islands. Therefore, the surface tension of the silica – gold interface is changed and the capillary forces cause the wetting of the island. At the triple phase line the delivered silicon is transformed to silica. The full encapsulation of the islands has been never observed. The proposed explanation is related to a volume reduction between the originally amorphous and the crystalline silica.

The presented results can find wide range of applications, e.g. in plasmonics and biosensing where the embedding of metal particles could be used for resonant frequency tuning. A relatively simple experimental procedure also opens possibilities for fabrication of nanostructures consisting of ordered arrays of embedded gold islands.

6. Summary

The main objectives of the work was to utilize the atomic force microscopy (AFM) for the study of ultrathin films and nanostructures. Both, the development of AFM instruments and fabrication of nanostructures with specific properties are of a long-term interest in the Institute of Physical Engineering (IPE) at the Brno University of Technology.

The atomic force microscope operating under ultrahigh vacuum conditions was previously developed at IPE and within this work have passed several upgrades regarding mainly the optical detection system, control electronics and optimization of the rotary slip-stick actuators. Optimization of motion of the piezo actuators having been quite unreliable before, required a detailed study and analysis. The significant improvement of the performance of the piezo actuator was achieved without the changes of their mechanical design. It was done by the modification of the driving pulses being used for controlling the displacement of the piezoceramic plates. It has been demonstrated that the critical parameter of the one slip-stick cycle (step) is the instantaneous velocity at the end of the sticking phase of the motion. The extended experimental measurements of the actuator response to the single and multiple pulses shown, that instantaneous velocity at the end of the slip phase should be maximal. It can be achieved by the shape of the pulse determined by the exponent of the exponential function and by the repetition frequency of the individual pulses. The experimental results have been supported by the numerical and analytical modelling of the actuator behavior during single and multiple steps. The motion of the slip-stick actuators was optimized and their smooth operation achieved.

Fabrication and characterization of metall nanostructures was carried out due to their wide range of applications in microelectronics, plasmonics (biosensing), semiconductor industry, magnetic memory media, and growth of nanowires. The analytical techniques used for their characterization were AFM and scanning electron microscopy (SEM), particularly. It has been demonstrated that the annealing of gold thin films leads to morphological transformations and formation of separated gold islands. The size and position of the fabricated islands can be controlled by the substrate patterning. The mechanism is driven by changes in local morphology parameters of the fabricated pattern elements, where the local surface curvatures influence the opening of the voids in the originally continuous gold film. During the annealing the voids are enlarged and separate the elements of the gold films along the high steps of the pattern. Further annealing of the gold films up to 600 °C results in the formation of well separated gold islands following the grid pattern. The patterning of substrates was carried out by electron beam lithography using grid patterns with square widths of 100, 200, 300, 400 and 500 nm. It has been shown that proposed methods are suitable for fabrication of well-ordered arrays of gold islands.

In the last part of the work the formation of craters during the annealing of gold films at 1000 °C is described. It has been shown that gold islands formed after the initial dewetting modify the silica substrate. We have proposed the digging mechanism caused by the mass transfer of the silica from the area bellow the gold islands to their perimeter. It has been determined that the digging speed is inversely related to the size of the gold islands where

the smaller islands are digging faster. The presented phenomena and fabrication procedure can be utilized in plasmonics and biosensing applications, particularly.

7. References

1. Binnig, G., C.F. Quate, and C. Gerber, *Atomic Force Microscope.* Physical Review Letters, 1986. **56**(9): p. 930-933.
2. Binnig, G. and H. Rohrer, *Scanning tunneling microscopy.* Surface Science Letters, 1983. **126**(1–3): p. A104.
3. Kruse, P., *Scanning Probe Microscopy: The Lab on a Tip: Ernst Meyer, Hans Josef Hug, Roland Bennewitz, Springer-Verlag, Berlin, Heidelberg, 2004, ISBN 3-540-43180-2.* Journal of Electron Spectroscopy and Related Phenomena, 2004. **135**(1): p. 83.
4. Basanta, M.A., et al., *Optimized atomic-like orbitals for first-principles tight-binding molecular dynamics.* Computational Materials Science, 2007. **39**(4): p. 759-766.
5. Lopour, F., *Development and application of an UHV SPM microscope.* 2006, Vysoké učení technické v Brně.
6. Wang, H., et al., *Multi-scale analysis of AFM tip and surface interactions.* Chemical Engineering Science, 2007. **62**(13): p. 3589-3594.
7. Ebeling, D. and S.D. Solares, *Bimodal atomic force microscopy driving the higher eigenmode in frequency-modulation mode: Implementation, advantages, disadvantages and comparison to the open-loop case.* Beilstein Journal of Nanotechnology, 2013. **4**: p. 198-207.
8. Lee, M. and W. Jhe, *General Theory of Amplitude-Modulation Atomic Force Microscopy.* Physical Review Letters, 2006. **97**(3): p. 036104.
9. Zhang, Z.M., et al., *Piezoelectric friction-inertia actuator-a critical review and future perspective.* Int J Adv Manuf Technol, 2012. **62**(5-8): p. 669-685.
10. Peng, J.Y. and X.B. Chen, *Modeling of Piezoelectric-Driven Stick-Slip Actuators.* Ieee-Asme T Mech, 2011. **16**(2): p. 394-399.
11. Nguyen, H.X., C. Edeler, and S. Fatikow, *Contact mechanics modeling of piezo-actuated stick-slip microdrives.* Phys Mesomech, 2012. **15**(5-6): p. 280-286.
12. Drevniok, B., et al., *Methods and instrumentation for piezoelectric motors.* Rev Sci Instrum, 2012. **83**(3): p. 033706.
13. Jean-Marc Breguet, R.C., *Stick and Slip Actuators: design, control, performances and applications.* International Symposium on Micromechatronics and Human Science 1998: p. 89 - 95.
14. Anantheshwara, K., N.S. Murali, and M.S. Bobji, *Effect of friction on the performance of inertial slider.* Sadhana-Acad Proc Eng Sci, 2008. **33**(3): p. 221-226.
15. Merry, R., R. van de Molengraft, and M. Steinbuch, *Modeling of a walking piezo actuator.* Sens Actuator A-Phys, 2010. **162**(1): p. 51-60.
16. Merry, R.J.E., et al., *Modeling and Waveform Optimization of a Nano-motion Piezo Stage.* Ieee-Asme T Mech, 2011. **16**(4): p. 615-626.
17. Sun, D., et al., *Cylindrical ultrasonic linear microactuator based on quasi-traveling wave propagation on a thin film metallic glass pipe supported by a piezoelectric ceramic tube.* Sens Actuator A-Phys, 2009. **156**(2): p. 359-365.
18. Snitka, V., *Ultrasonic actuators for nanometre positioning.* Ultrasonics, 2000. **38**(1–8): p. 20-25.
19. Capozza, R., et al., *Stabilizing Stick-Slip Friction.* Phys Rev Lett, 2011. **107**(2).
20. Nováček, Z., et al., *Systém pro charakterizaci a optimalizaci pizomotorů.* Jemná mechanika a optika, 2013. **58**(6): p. 190-193.
21. van Honschoten, J.W., N.R. Tas, and M. Elwenspoek, *The profile of a capillary liquid bridge between solid surfaces.* American Journal of Physics, 2010. **78**(3): p. 277-286.

22. *NI-DAQmx Software.* 2012; Available from: http://www.ni.com/dataacquisition/nidaqmx.htm.
23. Orfanidis, S.J., *Introduction to Signal Processing*, ed. E. Cliffs. 1996, New York: Prentice Hall.
24. Hwang, D.H. and K.H. Zum Gahr, *Transition from static to kinetic friction of unlubricated or oil lubricated steel/steel, steel/ceramic and ceramic/ceramic pairs.* Wear, 2003. **255**(1–6): p. 365-375.
25. Thompson, C.V., *Solid-State Dewetting of Thin Films*, in *Annual Review of Materials Research, Vol 42*, D.R. Clarke, Editor. 2012, Annual Reviews: Palo Alto. p. 399-434.
26. Giermann, A.L. and C.V. Thompson, *Solid-state dewetting for ordered arrays of crystallographically oriented metal particles.* Applied Physics Letters, 2005. **86**(12).
27. Jiang, W., et al., *Phase field approach for simulating solid-state dewetting problems.* Acta Materialia, 2012. **60**(15): p. 5578-5592.
28. Wang, D., et al., *Ordered arrays of nanoporous gold nanoparticles.* Beilstein Journal of Nanotechnology, 2012. **3**: p. 651-657.
29. Dong, W. and P. Schaaf, *Thermal dewetting of thin Au films deposited onto line-patterned substrates.* Journal of Materials Science, 2012. **47**(4): p. 1605-8.
30. Ye, J. and C.V. Thompson, *Regular pattern formation through the retraction and pinch-off of edges during solid-state dewetting of patterned single crystal films.* Physical Review B, 2010. **82**(19).
31. Ibach, H., *Physics of Surfaces and Interfaces*. Vol. Springer-Verlag Berlin Heidelberg. 2006.
32. Vrij, A. and J.T.G. Overbeek, *Rupture of thin liquid films due to spontaneous fluctuations in thickness.* Journal of the American Chemical Society, 1968. **90**(12): p. 3074-3078.
33. Presland, A.E.B., G.L. Price, and D.L. Trimm, *Kinetics of hillock and island formation during annealing of thin silver films.* Progress in Surface Science, 1972. **3, Part 1**(0): p. 63-96.
34. Mullins, W.W., *Capillarity-induced surface morphologies.* Interface Science, 2001. **9**(1-2): p. 9-20.
35. Mullins, W.W. and P.G. Shewmon, *THE KINETICS OF GRAIN BOUNDARY GROOVING IN COPPER.* Acta Metallurgica, 1959. **7**(3): p. 163-170.
36. Mullins, W.W., *GRAIN BOUNDARY GROOVING BY VOLUME DIFFUSION.* Transactions of the American Institute of Mining and Metallurgical Engineers, 1960. **218**(2): p. 354-361.
37. Ye, J. and C.V. Thompson, *Templated Solid-State Dewetting to Controllably Produce Complex Patterns.* Advanced Materials, 2011. **23**(13): p. 1567-1571.
38. Henley, S.J., J.D. Carey, and S.R.P. Silva, *Pulsed-laser-induced nanoscale island formation in thin metal-on-oxide films.* Physical Review B, 2005. **72**(19).
39. Kojima, Y. and T. Kato, *Nanoparticle formation in Au thin films by electron-beam-induced dewetting.* Nanotechnology, 2008. **19**(25).
40. Tesler, A.B., et al., *Tunable Localized Plasmon Transducers Prepared by Thermal Dewetting of Percolated Evaporated Gold Films.* Journal of Physical Chemistry C, 2011. **115**(50): p. 24642-24652.
41. Karakouz, T., et al., *Mechanism of morphology transformation during annealing of nanostructured gold films on glass.* Physical Chemistry Chemical Physics, 2013. **15**(13): p. 4656-4665.
42. Lifshitz, I.M. and V.V. Slyozov, *THE KINETICS OF PRECIPITATION FROM SUPERSATURATED SOLID SOLUTIONS.* Journal of Physics and Chemistry of Solids, 1961. **19**(1-2): p. 35-50.
43. Zhdanov, V.P., E.M. Larsson, and C. Langhammer, *Novel aspects of Ostwald ripening of supported metal nanoparticles.* Chemical Physics Letters, 2012. **533**(0): p. 65-69.
44. Giermann, A.L. and C.V. Thompson, *Requirements for graphoepitaxial alignment through solid-state dewetting of Au films.* Journal of Applied Physics, 2011. **109**(8).
45. Dong, W. and P. Schaaf, *Two-dimensional nanoparticle arrays formed by dewetting of thin gold films deposited on pre-patterned substrates.* Journal of Materials Science: Materials in Electronics, 2011. **22**(8): p. 1067-70.

46.   Dong, W. and P. Schaaf, *Nanoporous gold nanoparticles.* Journal of Materials Chemistry, 2012. **22**(12): p. 5344-8.

47.   Norrman, S., et al., *QUANTITATIVE EVOLUTION STUDIES OF PARTICLE SEPARATION, SIZE AND SHAPE FOR VAPOUR-DEPOSITED ULTRATHIN GOLD-FILMS ON GLASS SUBSTRATES.* Thin Solid Films, 1981. **77**(4): p. 359-366.

48.   Golan, Y., L. Margulis, and I. Rubinstein, *VACUUM-DEPOSITED GOLD-FILMS .1. FACTORS AFFECTING THE FILM MORPHOLOGY.* Surface Science, 1992. **264**(3): p. 312-326.

49.   Neuman, J., et al., *Příprava pravidelně uspořádaných ostrůvků zlata.* Jemná mechanika a optika, 2014. **59**(6-7): p. 199-201.

50.   Karakouz, T., et al., *Highly Stable Localized Plasmon Transducers Obtained by Thermal Embedding of Gold Island Films on Glass.* Advanced Materials, 2008. **20**(20): p. 3893-3899.

51.   Kedem, O., et al., *Sensitivity and Optimization of Localized Surface Plasmon Resonance Transducers.* Acs Nano, 2011. **5**(2): p. 748-760.

52.   Tesler, A.B., et al., *Solid-State Thermal Dewetting of Just-Percolated Gold Films Evaporated on Glass: Development of the Morphology and Optical Properties.* Journal of Physical Chemistry C, 2013. **117**(21): p. 11337-11346.

53.   Necas, D. and P. Klapetek, *Gwyddion: an open-source software for SPM data analysis.* Central European Journal of Physics, 2012. **10**(1): p. 181-188.

54.   Hutchings, G., *Catalysis by Gold: Recent Advances in Oxidation Reactions*, in *Nanotechnology in Catalysis*, B. Zhou, et al., Editors. 2007, Springer New York. p. 39-54.

55.   Della Pina, C., E. Falletta, and M. Rossi, *Gold Nanoparticles-catalyzed Oxidations in Organic Chemistry*, in *Nanoparticles and Catalysis*. 2008, Wiley-VCH Verlag GmbH & Co. KGaA. p. 427-455.

56.   Shalav, A., T. Kim, and R.G. Elliman, *SiOx Nanowires Grown via the Active Oxidation of Silicon.* Ieee Journal of Selected Topics in Quantum Electronics, 2011. **17**(4): p. 785-793.

57.   Ruach-Nir, I., et al., *Silica-stabilized gold island films for transmission localized surface plasmon sensing.* Journal of the American Chemical Society, 2007. **129**(1): p. 84-92.

58.   Powell, B.R. and S.E. Whittington, *ENCAPSULATION - A NEW MECHANISM OF CATALYST DEACTIVATION.* Journal of Catalysis, 1983. **81**(2): p. 382-393.

59.   Hu, X.Y., D.G. Cahill, and R.S. Averback, *Burrowing of Pt nanoparticles into SiO2 during ion-beam irradiation.* Journal of Applied Physics, 2002. **92**(7): p. 3995-4000.

60.   Bowker, M., et al., *Encapsulation of Au Nanoparticles on a Silicon Wafer During Thermal Oxidation.* The Journal of Physical Chemistry C, 2013. **117**(41): p. 21577-21582.

61.   Mueller, C.M., F.C.F. Mornaghini, and R. Spolenak, *Ordered arrays of faceted gold nanoparticles obtained by dewetting and nanosphere lithography.* Nanotechnology, 2008. **19**(48).

62.   Ono, L.K., F. Behafarid, and B.R. Cuenya, *Nano-Gold Diggers: Au-Assisted SiO2-Decomposition and Desorption in Supported Nanocatalysts.* Acs Nano, 2013. **7**(11): p. 10327-10334.

63.   Fu, Q. and T. Wagner, *Interaction of nanostructured metal overlayers with oxide surfaces.* Surface Science Reports, 2007. **62**(11): p. 431-498.

64.   Ross, F.M., J. Tersoff, and R.M. Tromp, *Coarsening of Self-Assembled Ge Quantum Dots on Si(001).* Physical Review Letters, 1998. **80**(5): p. 984-987.

65.   Vaskevich, A., T. Sehayek, and I. Rubinstein, *Mass Thickness Analysis of Gold Thin Films Using Room Temperature Gas-Phase Chlorination.* Analytical Chemistry, 2009. **81**(8): p. 2877-2883.

66.   Dick, K., et al., *Size-dependent melting of silica-encapsulated gold nanoparticles.* Journal of the American Chemical Society, 2002. **124**(10): p. 2312-2317.

67.   Ajayan, P.M. and S. Iijima, *Wetting and de-wetting transitions of small metal particles on substrates under electron irradiation.* Journal of Colloid and Interface Science, 1991. **147**(1): p. 281-285.

68.   Klimmer, A., et al., *Size-dependent effect of ion bombardment on Au nanoparticles on top of various substrates: Thermodynamically dominated capillary forces versus sputtering.* Physical Review B, 2009. **79**(15).

69.   Zhao, K., R.S. Averback, and D.G. Cahill, *Patterning of metal nanowires by directed ion-induced dewetting.* Applied Physics Letters, 2006. **89**(5).

70.   De Los Santos, V.L., et al., *Crystallization and surface morphology of Au/SiO2 thin films following furnace and flame annealing.* Surface Science, 2009. **603**(19): p. 2978-2985.